The Pennsylvania State University
The Graduate School
Department of Electrical Engineering

DISPERSION AND DISTRIBUTION OF OPTICAL INDEX OF REFRACTION IN FERROELECTRIC RELAXOR CRYSTAL

A Thesis in
Electrical Engineering
by
Chunlai Li

Submitted in Partial Fulfillment
of the Requirements
for the degree of
Doctor of Philosophy

May 2006

The thesis of Chunlai Li has been reviewed and approved* by the following

Date of Signature

Ruyan Guo
Professor of Electrical Engineering and Materials Research
Thesis Co-Advisor
Co-Chair of Committee

Amar S. Bhalla
Professor of Materials and Electrical Engineering
Thesis Co-advisor
Co-Chair of Committee

Leslie Eric Cross
Evan Pugh Professor Emeritus of Electrical Engineering

William B. White
Professor Emeritus of Geochemistry

Shizhuo Yin
Associate Professor of Electrical Engineering

W. Kenneth Jenkins
Professor of Electrical Engineering
Head of the Department of Electrical Engineering

*Signatures are on file in the graduate school

Abstract

This thesis deals with the optical properties of relaxor ferroelectrics with nano/micro polar regions, including their optical frequency dispersion near phase transition, thermo-optical properties, and transmission spectrum analysis. The essential objectives of this thesis work are to deepen the understanding on diffuse phase transition of relaxor ferroelectrics and to obtain practical data for potential optical application from technically important ferroelectrics crystals PBN and PZN-PT.

Temperature dependent birefringence and optical refractive indices of PBN ($Pb_{1-x}Ba_xNb_2O_6$) crystal (1-x=0.57) were measured in several optical wavelengths (λ= 694nm, 633nm, 535nm, and 450nm) to understand the optical frequency dependency of ferroelectric phase transitions in relaxor ferroelectric crystals of tungsten bronze structure. Local polarization is verified to be dynamically activated by thermal process and probed effectively by suitable wavelength of light. An optical isotropic point, as a function of temperature and light frequency, is reported at which the crystal's standing birefringence is fully compensated by polarization. A modified single oscillator model is used to calculate the index of refraction in the ferroelectric phase. The deviation temperature from the single oscillator model is reported to be significantly marking the crossover from macroscopic to microscopic polarization. A new parameter, optical Curie temperature region, defined by the temperature difference between the well known Burns temperature and the deviation temperature (from the single oscillator model for index of refraction) is explored for its significance in depolarization behavior of the micro- to nano-polar regions of the ferroelectric relaxor.

Temperature dependent optical indices of refraction of PZN-0.12PT (1-x)$PbZn_{1/3}Nb_{2/3}O_3$-x$PbTiO_3$, x=0.12, were also studied with emphasis on poling effect. The refractive index n_3 decreases as a result of [001] poling. Temperature dependent effective energy of dispersion oscillator E_0 and dispersion energy E_d were calculated using single oscillator model and found that E_0 and E_d increased by 32% and 60% after [001] poling, respectively. Birefringence of poled PZN-0.12PT also was measured with several frequencies and varying temperature. The polarization derived from refractive index and birefringence were consistent with each other. The remnant polarization was increased by approximately 30% as a result of [001] poling. Transmission spectrum of PZN-0.12PT was measured from near UV to IR for both poled sample and unpoled sample. Transmission was improved significantly after poling. By analyzing the transmission spectrum in the visible range, optical band gap and lattice phonon were determined. The existence of hydrogen in PZN-0.12PT single crystal grown by flux method was postulated based on evidence obtained by FTIR.

For accurate and fast birefringence measurement, which is of fundamental importance to device design, quality control, and various sensing functions, a two-dimensional birefringence profiling and analysis system was designed and implemented successfully. Jones matrices of two and three 90° domains are derived and conclude that odd number of stacked 90° domains can be treated as a single 90° domain while even number of stacked 90° domains can be treated as two 90° domains. By rotating analyzer method a test experiment using voltage controllable liquid crystal as sample is demonstrated.

Table of Contents

List of Tables

List of Figures

Acknowledgements

I would express my sincerely gratitude to my advisors Dr. Ruyan Guo and Dr.Amar Bhalla for their guidance, support, and help during my study. Before I joined this group about four years ago, I knew little about ferroelectrics and never thought I could extend my academic career in this field. I would like to thank Dr. Guo and Dr. Bhalla for their invaluable enlightenment and patience on my academic exploration. Also I would like to thank the thesis committee members, Drs. Cross, White and Yin for their time and insightful comments on this work.

This work cannot be finished without the help from my colleagues and the staff at the MRL. They are: Dr Shujun Zhang Dr. Yoshi Somiya, Dr. Ed Alberta, Dr. Alok, Dr. Chuanyong Huang, Dr. Youwei Fu, Mr. Hongbo Liu, Mr. Jeff Long, Mrs. Nicole Wanderling, and Mrs. Man Gu.

Finally, my family in China deserves my profound gratitude for their support and encouragement. Most of all, I would like to express my gratitude to my lovely wife Hongli Pu.

Chapter 1 Introduction

1.1 Introduction of ferroelectrics

1.1.1 Ferroelectrics

Ferroelectricity is a phenomenon that was discovered in 1921. The name is somewhat misleading as it is not related with iron despite the ferro- prefix. The connection is as follows. Ferromagnetic materials have a spontaneous magnetization below a critical temperature due to the alignment of magnetic dipoles and the prefix was given because the first discovered compound contained iron. It is because of the analogy between the magnetic and electric dipole behavior that ferroelectrics are named.

Ferroelectricity has also been called Seignette electricity, as Seignette or Rochelle Salt (RS) was the first material found to show ferroelectric properties such as a spontaneous polarization on cooling below the Curie point, ferroelectric domains and a ferroelectric hysteresis loop.

Due to their typically high dielectrics constants and piezoelectric constants, a lot of efforts in the research on ferroelectric materials came in the 1950's, leading to the widespread use of barium titanate ($BaTiO_3$) based ceramics in capacitor applications and piezoelectric transducer devices. Since then, many other ferroelectric ceramics including lead titanate ($PbTiO_3$), lead zirconate titanate (PZT), lead lanthanum zirconate titanate (PLZT), and relaxor ferroelectrics like lead magnesium niobate (PMN) have been developed and utilized for a variety of applications. With the development of material (ceramic) processing and thin film technology, many new applications have emerged. The biggest use of ferroelectric ceramics have been in the areas such as dielectric

ceramics for capacitor applications, ferroelectric thin films for non volatile memories, piezoelectric materials for medical ultrasound imaging and actuators, and electro-optic materials for data storage and displays.

In the past few decades, many books and reviews have been written explaining the concepts of ferroelectricity in materials [Lines and Glass 1977; Jaffe et al. 1971; Xu 1991]. In this chapter, an effort is made to introduce the basic principles governing ferroelectricity and some general properties related to this thesis.

1.1.2 General Properties of Ferroelectrics

1.1.2.1 Crystal Symmetry

The lattice structure described by the Bravais unit cell of the crystal governs the crystal symmetry. Though there are thousands of crystals in nature, they all can be grouped together into 230 microscopic symmetry types or space groups based on the symmetry elements [Nye 1990; Newnham 1975]. A combination of these symmetry elements gives us the macroscopic symmetry also called as point groups. It can be shown by the inspection of the 230 space groups that there are just 32 point groups. As shown in Table 1.1, the seven crystal systems can be divided into these point groups according to the point group symmetry they possess.

The thirty-two point groups can be further classified into (a) crystals having a center of symmetry and (b) crystals which do not possess a center of symmetry. Crystals with a center of symmetry include the 11 point groups labeled centrosymmetric in Table 1.1. These point groups do not show polarity. The remaining 21 point groups do not have a center of symmetry (i.e. non-centrosymmetric). A crystal having no center of symmetry

Table 1.1 Point groups for the seven crystal systems

Crystal Structure	Point Groups	Centro-Symmetric	Non-centrosymmetric	
			Piezoelectric	Pyroelectric
Triclinic	1, $\bar{1}$	$\bar{1}$	1	1
Monoclinic	2, m, 2/m	2/m	2, m	2, m
Orthorhombic	222, mm2, mmm	mmm	222, mm2	mm2,
Tetragonal	4, $\bar{4}$, 4/m, 422, 4mm, $\bar{4}$2m, (4/m)mm	4/m, (4/m)mm	4, $\bar{4}$, 422, 4mm, $\bar{4}$2m	4, 4mm
Trigonal	3, $\bar{3}$, 32, 3m, $\bar{3}$m	$\bar{3}$, $\bar{3}$m	3, 32, 3m	3, 3m
Hexagonal	6, $\bar{6}$, 6/m, 622, 6mm, $\bar{6}$m2, (6/m)mm	6/m, (6/m)mm	6, $\bar{6}$, 622, 6mm, $\bar{6}$m2	6, 6mm
Cubic	23, m3, 432, $\bar{4}$3m, m3m	m3, m3m	23, $\bar{4}$3m	------

possesses one or more crystallographically unique directional axes. All non-centrosymmetric point groups, except the 432 point group, show piezoelectric effect along unique directional axes. Piezoelectricity is the ability of certain crystalline materials to develop an electrical charge proportional to a mechanical stress. It was discovered by the Curie brothers in 1880. Piezoelectric materials also show a converse effect, where a geometric strain (deformation) is produced on the application of a voltage. The direct and converse piezoelectric effects can be expressed in tensor notation as,

$$P_i = d_{ijk}\sigma_{jk} \tag{1.1.1}$$

$$e_{ij} = d_{kij}E_k \tag{1.1.2}$$

where P_i is the polarization generated along the i- axis in response to the applied stress σ_{jk}, and d_{ijk} is the piezoelectric coefficient. For the converse effect, e_{ij} is the strain generated in a particular orientation of the crystal on the application of electric field E_k along the k-axis. [Lines and Glass 1977]

Out of the twenty point groups, which show the piezoelectric effect, ten point groups (including 1, 2, m, mm2, 4, 4mm, 3, 3m, 6, and 6mm) have only one unique directional axis. Such crystals are called polar crystals as they show spontaneous polarization. Most of the non-vanishing properties of crystals can be derived from the symmetry elements of unit cell or structure alone.

1.1.2.2 Phase transition

The characters of ferroelectrics exist only in a temperature range. Ferroelectricity will disappear when temperature is higher than a phase transition temperature T_c, Curie point. And the ferroelectrics transforms from ferroelectric phase to paraelectric phase,

with zero spontaneous polarization. The static dielectric constant obeys the Curie-Weiss law:

$$\varepsilon = \varepsilon_0 + \frac{C}{T - T_0} \tag{1.1.3}$$

where ε_0 is the dielectric constant of vacuum, C is the Curie constant and T_o is the Curie temperature. For the second order transition $T_0 = T_c$ while for first order phase transition $T_0 < T_c$.

Ferroelectrics may exhibit one or more polar phase below Curie point. Barium titanate ($BaTiO_3$) has three polar phases as a function of temperature. Barium titanate transforms from cubic (paraelectric) to tetragonal (ferroelectric) at 120°C, to orthorhombic (ferroelectric) at ~5°C, and to rhombohedral (ferroelectric) at -90°C. The polarization axes are along the [001], [110], and [111] directions for the tetragonal, orthorhombic, and rhombohedral phase, respectively as shown in Figure 1.1.

1.1.2.3 Domain and hysteresis

When a ferroelectric crystal is cooled below the Curie temperature, in the absence of external electric field and mechanical stress, it breaks up into domains of different orientation under the constraints of boundary conditions. Within a domain, all the electric dipoles are aligned in the same direction resulting uniform polarization. The formation of the domains lowers the total energy of ferroelectrics. The polarization direction in a domain can be switched to the direction of the electric field when the ferroelectrics is in an applied electric field. The total polarization exhibits the characteristic hysteresis loop when changing the magnitude and direction of the applied

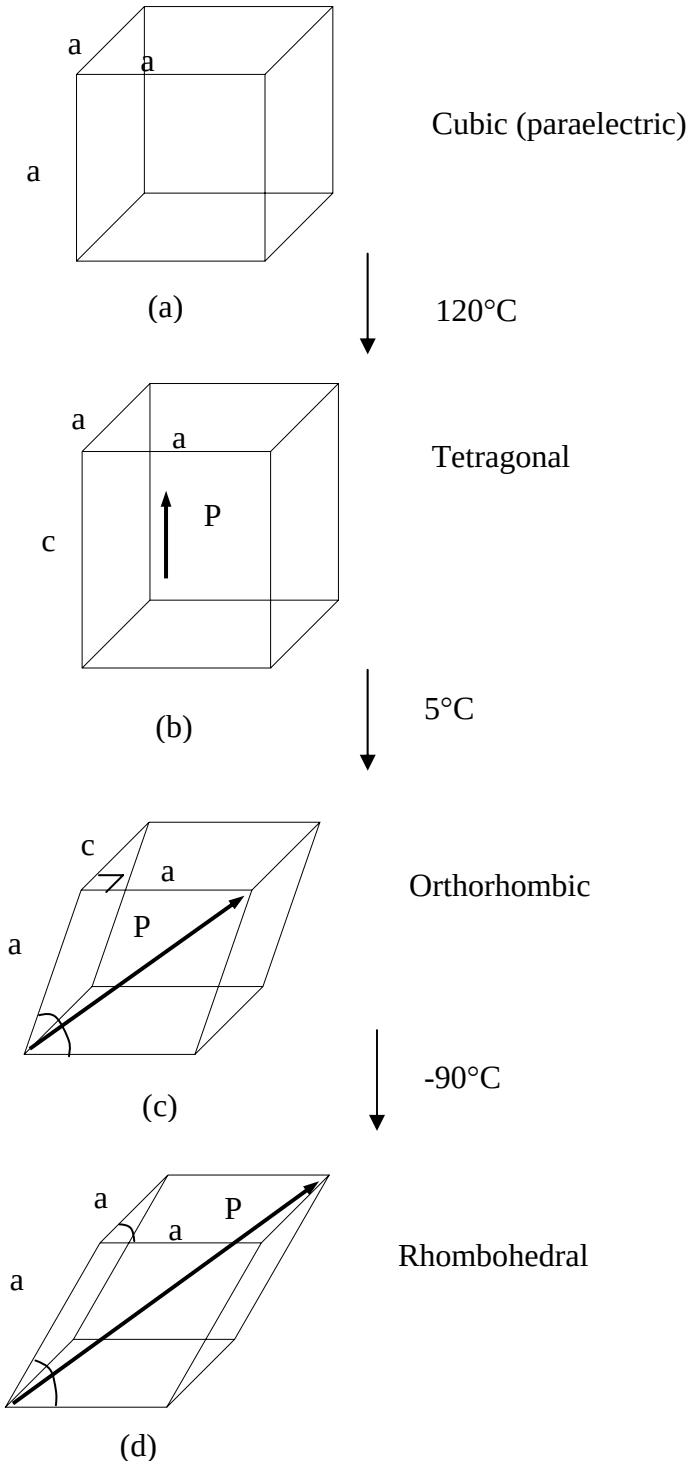

Figure 1.1 Unit cells of the four phases of $BaTiO_3$ as a function of temperature. (a) cubic T>120°C (b) tetragonal 5°C <T<120°C, (c) orthorhombic -90°C <T<5°C, (d) rhombohedral T<-90°C

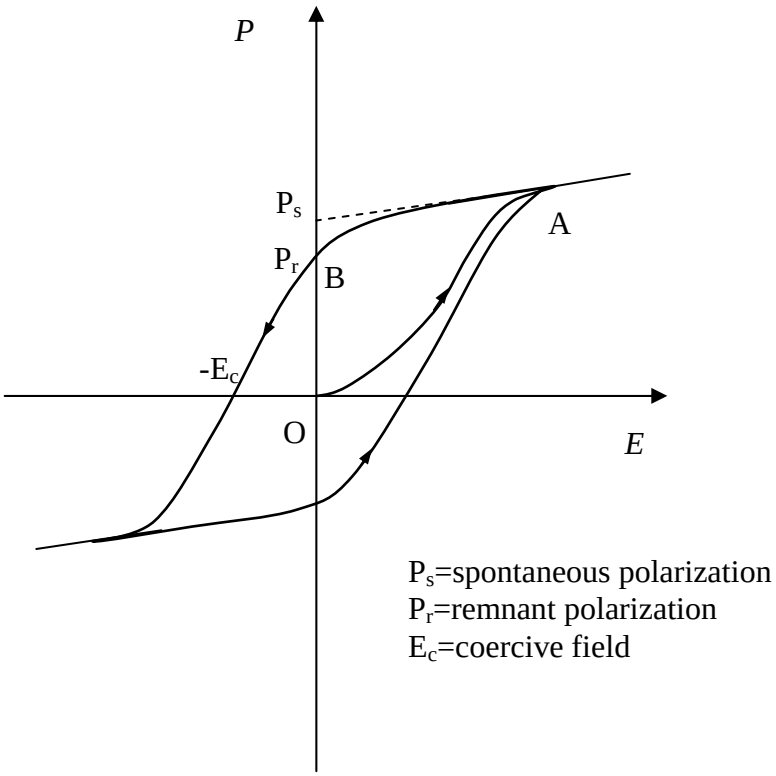

Figure 1.2 A typical ferroelectrics hysteresis loop

electric field as shown in Figure 1.2, assuming only two orientations of spontaneous polarization in a ferroelectrics and the total polarization is zero in the absence of applied electric field. Now applying an electric field along one orientation, the domains with the polarization direction parallel to the electric field enlarge while the domains with the polarization direction opposite to the electric field diminish. The total polarization increases with the electric field corresponding to the curve OA in Figure 1.2. There is only one domain in the ferroelectric when the electric field is strong enough. All polarizations are parallel to the electric field and the total polarization is saturated. The total polarization decreases to a remnant polarization P_r along the curve AB while the electric field decreasing to zero. In order to remove the remnant polarization, a reversal electric field > E_c (coercive field) is applied.

1.2 Relaxor ferroelectrics

Relaxor ferroelectrics are ferroelectrics with diffuse phase transitions, which are characterized [Cross 1987] by (i) a significant frequency dependence of their peak permittivity at T_m, (ii) persistence of the local polarization far above the phase transition temperature T_C , and (iii) absence of macroscopic spontaneous polarization and structural symmetry breaking after zero-field cooling. Table 1.2 listed the differences between the normal and relaxor ferroelectrics. Some more explains will be given in later sections.

Relaxor ferroelectric behavior occurs dominantly in lead based perovskite structures of $A(B'B'')O_3$ compositions, where B' is a low-valence cation (such as Mg^{2+}, Zn^{2+}, Ni^{2+}, Co^{2+}, Fe^{3+}, Sc^{3+}, In^{3+}, and Yb^{3+}) and B'' is a ferroelectrically active cation that has a higher valence and no outer d-electron (such as Ti^{4+}, Zr^{4+}, Nb^{5+}, Ta^{5+}, and W^{6+}).[Glass 1969] Similar features are also observed in tungsten bronze

Table 1.2 Property differences between normal and relaxor ferroelectrics

Property	**Normal Ferroelectrics**	**Relaxor Ferroelectrics**
Dielectric temperature dependence	Sharp 1^{st} or 2^{nd} order transition at Curie point T_c	Broad diffusive phase transition at Curie maxima
Dielectric frequency dependence	Weak Frequency dependence	Strong frequency dependence
Dielectric Behavior in paraelectric range ($T > T_c$)	Follows Curie - Weiss law	Follows Curie - Weiss square law
Remnant polarization (P_R)	Strong P_R	Weak P_R
Diffraction of X-Rays	Line splitting due to deformation from paraelectric to ferroelectric phase	No X-Ray line splitting
Scattering of light	Strong anisotropy	Very weak anisotropy to light

structurematerials such as $A_xBa_{1-x}Nb_2O_6$ (A=Sr, Pb) [Lines and Glass 1977]. First discovered by Smolenskii *et al.* [Smolenskii and Isupov 1954], these materials exhibit broad and anomalously large dielectric maximas which make them ideal candidate for multilayer capacitors [Shrout and Halliyal 1987], electrostrictive actuators [Uchino 1986], pyroelectric bolometeters [Whatmore et al. 1987], electro-optics [McHenry et al. 1989], and for nonvolatile random access memories [Paz de Araujo et al. 1995]. The existence of a morphotropic phase boundary in various solid solutions of relaxor compounds with $PbTiO_3$ (PT) similar to that in the well know $Pb(Zr_{1-x}Ti_x)O_3$ (PZT) system, also makes these materials excellent candidates for piezoelectric transducers [Choi et al. 1989].

1.2.1 Structure of relaxor ferroelectric

Relaxor ferroelectrics behavior in crystalline ferroelectrics has been studied in many ferroelectric solid solution systems, which have either the complex perovskite or tungsten bronze crystal structure [Cross 1987, 1994].

1.2.1.1 Perovskite structure

Perovskite is a family name of a group of materials and the name comes from the mineral $CaTiO_3$ which exhibits a structure of type ABO_3. Many normal ferroelectric ceramics such as Barium Titanate ($BaTiO_3$), Lead Titanate ($PbTiO_3$), Lead Zirconate Titanate (PZT), Lead Lanthanum Zirconate Titanate (PLZT), Lead Magnesium Niobate (PMN), Potassium Niobate ($KNbO_3$), have a perovskite type structure. Most perovskite-type ferroelectrics are compounds with either $A^{2+}B^{4+}O_3^{2-}$ or $A^{1+}B^{5+}O_3^{2-}$ type formula.

The structure is illustrated in Figure 1.3.The A ions are the larger cations that sit at the corners of the cube and is coordinated by 12 oxygen ions. The smaller B ions

occupy the center of the cube and surrounded by an oxygen octahedron. The oxygen anions are situated at the center of the faces. Most ferroelectrics with oxide perovskite structure are cubic at high temperature, but at low temperatures they may transform into other structures. This structure is highly tolerant to cation substitution to A and B site lattice, and lead to the complex perovskite structure $A(B^{'}B^{''})O_3$. The structures of $A(B^{'}_{1/2}B^{''}_{1/2})O_3$ and $A(B^{'}_{1/3}B^{''}_{2/3})O_3$ are illustrated in Figure 1.4 and 1.5, respectively. This thesis will be concerned on solid solution of lead zinc niobate, $Pb(Zn_{1/3}Nb_{2/3})O_3$ with PT.

The single crystal $Pb(Zn_{1/3}Nb_{2/3})O_3$ (PZN) is a typical relaxor ferroelectric material with globally disordered complex perovskite structure in which Zn^{2+} and Nb^{5+} cations exhibit only short order coherency (2-50nm) on the B site. The averaged symmetry over the macroscopic scale is considered to be rohombohedral below the diffuse phase transition temperature of about 140°C[Kuwata et al. 1981].

1.2.1.2 Tungsten bronze structure

Ferroelectric tungsten bronze structure (TB) is transparent in the visible range and has tetragonal symmetry. The structure of the TB prototype is shown in Figure 1.6 as projected in the (001) plane. The tetragonal unit cell consists of 10 BO_6 octahedral linked by their corners. In such a manner three different types of tunnels, i.e. square (A_1), pentagon (A_2), and triangle (C), are formed parallel to the c-axis. There are two 12-fold coordinated sites (A_1), four 15-fold coordinated sites (A_2), and four 9-fold coordinates sites (C) per unit cell. The latter ones are the smallest. A large number of compound crystallize with TB structure, but the variety, the size and charge of the metal cations can

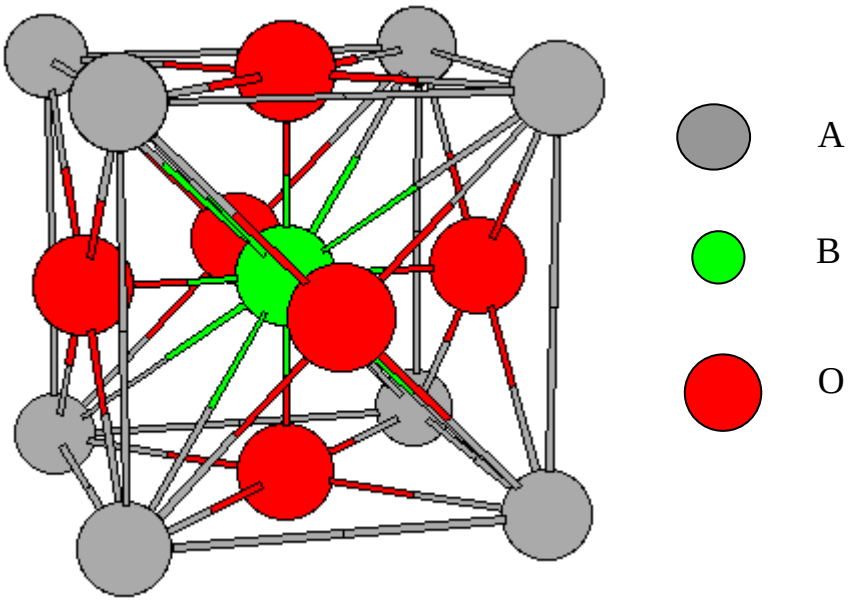

Figure 1.3 Illustration of the structure of pervoskite ABO_3

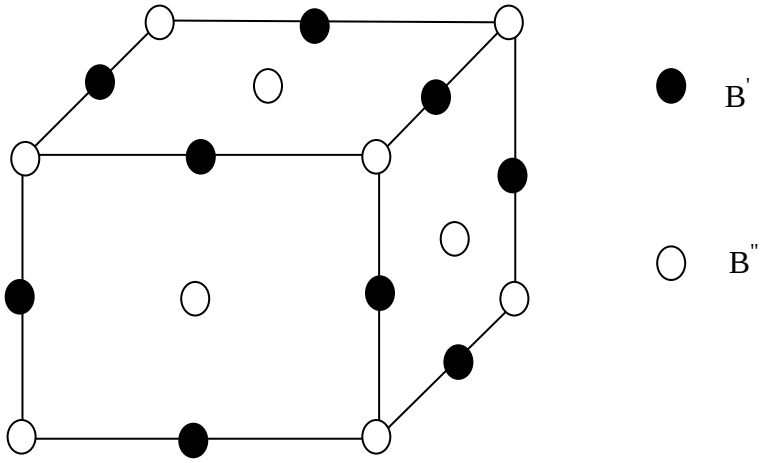

Figure 1.4 Ordered arrangement of B-site ions in complex pervskite: 1:1 order type

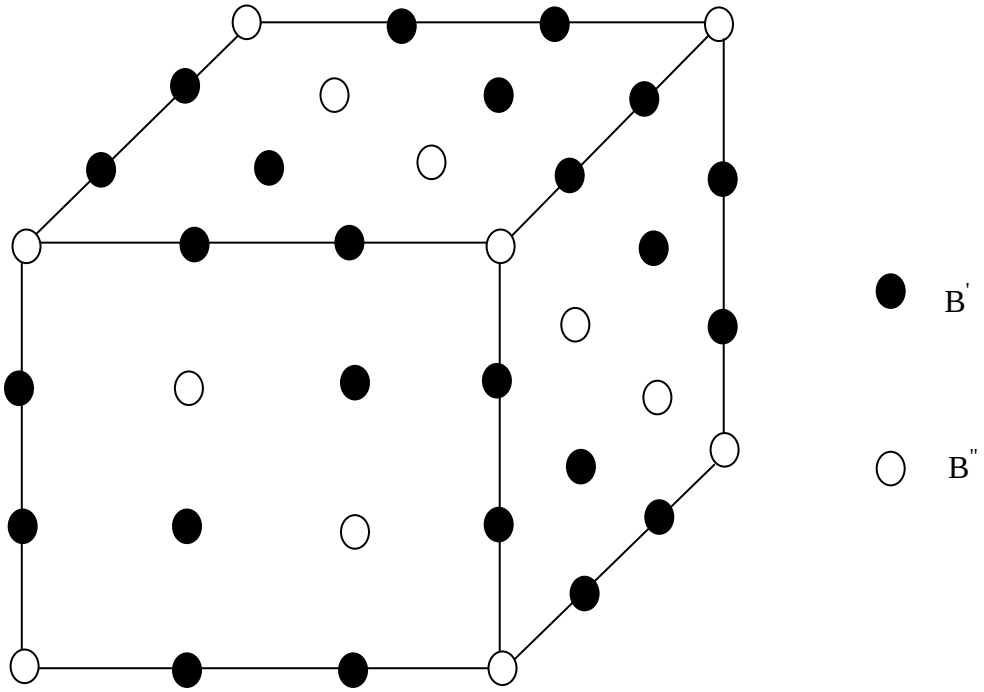

Figure 1.5 Ordered arrangement of B-site ions in complex pervskite: 1:2 order type

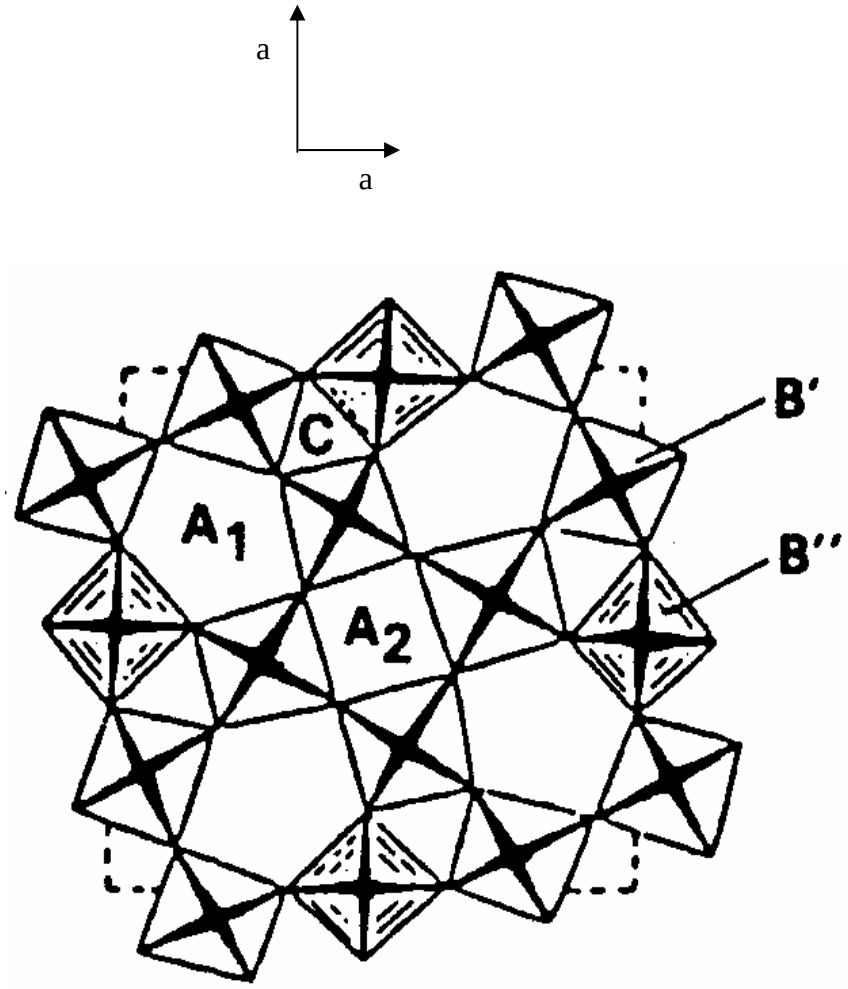

Chemical formulae
$(A_1)_x(A_2)_{1-x}C_4B_{10}O_{30}$
$(A_1)_{4+x}(A_2)_{2-2x}B_{10}O_{30}$
$(A_1)_{6-x}(A_2)_{4+x}B_{10}O_{30}$

A_1= 15- fold coordinated site
A_2= 12- fold coordinated site
C= 9- fold coordinated site
B= 6- fold coordinated site (two sites)

Figure 1.6 Tungsten bronze Type structure projected on (001) plane

cause subtle changes on the ferroelectrics phases and varying characteristics of ferroelectric properties. For example, $PbTa_2O_6$ is orthorhombic both above and below T_c, whereears $PbNb_2O_6$ is tetragonal above and orthorhombic below T_c, and $Sr_{1-x}Ba_xNb_2O_6$ (SBN) remains tetragonal both above and below T_c [Lines and Glass 1977]. The general composition may be considered to be close to one of the following formulae: (a) $(A_1)_x(A_2)_{1-x}C_4B_{10}O_{30}$ if both A_1 and A_2 are alkaline earth ions, (b) $(A_1)_{4+x}(A_2)_{2-2x}B_{10}O_{30}$if A_1 is an alkaline earth and A_2 is an alkali, and (c) $(A_1)_{6-x}(A_2)_{4+x}B_{10}O_{30}$ if both A_1 and A_2 are alkali ions. This thesis also will be concerned on tungsten bronze PBN composition.

1.2.2 Dielectric and related electrical properties

The static dielectric constant of normal ferroelectrics exhibits a sharp, narrow peak at *Tc*. For a single crystal the peak is very sharp and the width at half max is ~10–20 K. For a mixed oxide ferroelectrics the peak is somewhat rounded due to compositional fluctuations, and the width at half max is typically ~20–40 K. The ferroelectric response is frequency independent in the audio frequency range. By contrast a relaxor exhibits a very broad $\varepsilon(T)$ peak and strong frequency dispersion in the peak temperature T_m and in the magnitude of ε below T_m. The conventional wisdom has been that the broad $\varepsilon(T)$ peak, also referred to as a "diffuse phase transition", is associated with compositional fluctuations leading to many nano/micro polar regions with different compositions and $T_c s$. The breadth of the peak is simply a manifestation of the dipolar glass-like response of these materials.

The temperature dependence of $\varepsilon(T)$ of a ferroelectric obeys a Curie–Weiss law, above T_c by the linear $1/\varepsilon$ versus T response. While $\varepsilon(T)$ of a relaxor ferroelectrics exhibits strong deviation from this law for temperatures of many tens to a few hundred

degrees above T_m. It is only at very high temperatures that a linear $1/\varepsilon$ versus T response is obtained. Although the dielectric behavior of a typical relaxor is following the Curie - Weiss square law. A more general dielectric behavior of relaxor ferroelectrics has the form [Kirilov and Isupov, 1973]:

$$\frac{1}{\varepsilon} \propto (T - T_m)^{\alpha} \quad , \tag{1.2.1}$$

where $1 < \alpha \leq 2$, diffuseness coefficient $\alpha = 2$ is a special case for the "complete" relaxor ferroelectrics and $\alpha = 1$ for the normal ferroelectrics.

The P–E hysteresis loop is the signature of ferroelectrics in the low temperature ferroelectric phase. The large remnant polarization, P_r is a manifestation of the cooperative nature of the ferroelectric phenomenon. A relaxor, on the other hand, exhibits a so-called slim loop. For sufficiently high electric fields the nano polar regions of the relaxor can be oriented with the field leading to large polarization; however, on removing the field most of these domains re-acquire their random orientations resulting in a small P_r. The small P_r is evidence for the presence of some degree of cooperative freezing of dipolar (or nano polar regions) orientations.

The saturation and remnant polarizations of a ferroelectrics decrease with increasing temperature and vanish at the ferroelectrics transition temperature T_c. The vanishing of P at T_c is continuous for a second-order phase transition and discontinuous for a first-order transition. No polar regions exist above T_c. By contrast, the field-induced polarization of a relaxor decreases smoothly through the dynamic transition temperature T_m and retains finite values to rather high temperatures due to the fact that nano polar regions persist to well above T_m.

The ferroelectric transition can be thermodynamically first or second order and involves a macroscopic symmetry change at T_c. Transparent ferroelectrics exhibit strong optical anisotropy across T_c. However, there is no structural phase transition across *Tm* in a relaxor. The peak in $\varepsilon(T)$ is simply a manifestation of the slowing down of the dipolar motion below T_m. For transparent relaxors, there is no optical anisotropy across T_m.

1.2.3 Optical properties

The influence of phase transitions on the temperature dependence of refractive indices of transparent materials (whether they are structural, magnetic, soft-mode, normal ferroelectric or related to this work, relaxor ferroelectrics) has attracted growing interest [Schafer and Kleemann 1985]. Refractometry in the precursor region of ferroelectric phase transitions in the order to obtain information on the order parameter fluctuations above the Curie temperature has grown in importance as a means of probing the onset of the local short range order of polarization clusters [Burns and Dacol 1990a,b].

The characteristic refractive index behavior of three types of ferroelectric phase transition is illustrated in Figure 1.7 for a normal first order ferroelectric phase transition, a second order transition, and a relaxor ferroelectric. For a normal ferroelectric phase transition, the refractive index is linear at high temperature and then at *Tc* abruptly departs from linear behavior with a sharp discontinuity for a first order transition, or with a change in slope at a second order transition. In contrast, relaxor ferroelectrics display quite different behavior. At a temperature well above T_m the n(T) curve for relaxor departs from the straight line high temperature regimes and gradually becomes nonlinear. This temperature is referred to as a dipolar or Burns temperature.

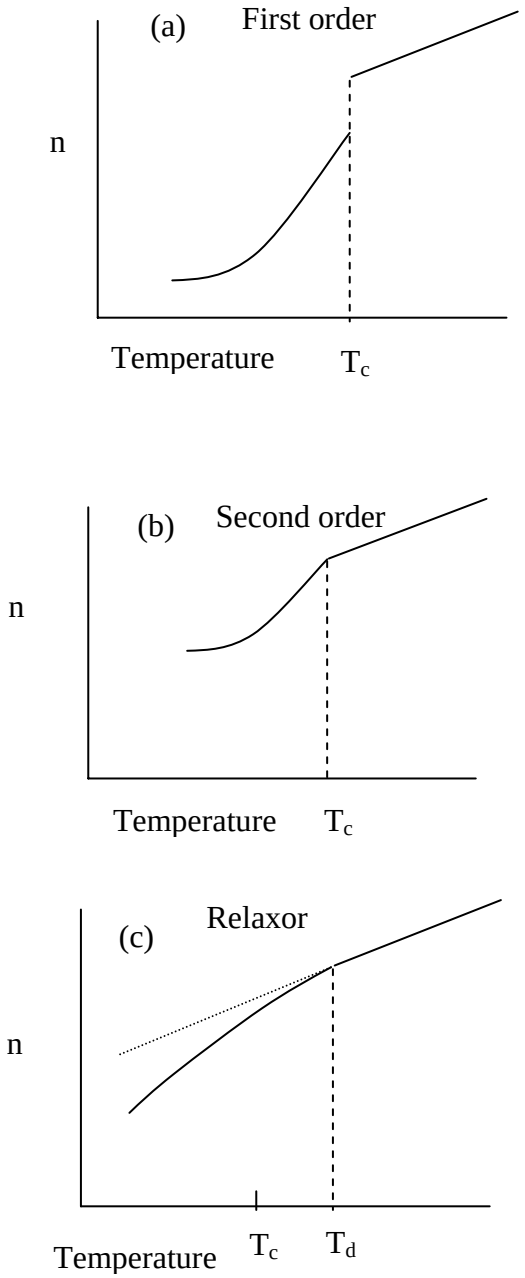

Figure 1.7 Representation of the characteristic refractive index vs. temperature behavior for ferroelectric systems with a) first order phase transition b) second order phase transition c) a relaxor phase transition

1.3 Domain in ferroelectrics

1.3.1 Ferroelectric Domain

Besides the fundamental importance to understand the relaxor ferroelectrics, domain investigation is also motivated by some practical applications, such as the general trend of miniaturization of electronic devices, photonic devices and nonvolatile random access memories.

When a ferroelectric crystal is cooled below the Curie temperature, in the absence of external electric field and mechanical stress, it breaks up into domains of different orientation under the constraints of symmetry requirement and boundary conditions. The main contributions to the free energy that can be reduced or increased by the formation of domain are: (i) the electrostatic energy or the depolarization energy, (ii) the energy of certain strain fields around imperfections, (iii) the domain wall energy, and (iv) the elastic energy. Therefore, if the crystal is brought to the ferroelectric state from the paraelectric phase by decreasing temperature, the minimization of the total system free energy may result in multi-domain structure. In addition, the distribution of internal stress due to crystal defects is considered to give rise to multi-domain structures. Qualitatively, to reduce the depolarization energy, antiparallel (180°) domains are favored. To decrease the strain energy, 90° domain (or other permissible non-90° domain walls) would be favored. If the spontaneous strain is small, forming 90° domains will not significantly reduce energy, thus one finds the crystal stays single domain or form 180° domains. If the crystal contains enough free mobile charge carriers that can sufficiently screen the depolarization field, 180° domain may not form and crystal may stay single domain.

Figure 1.8 shows the domain structure of a thin plate barium titanate in the tetragonal phase. (a) and (b) are 90° domain structure while (c) and (d) are 180° domain structures which are compatible with the original lattice structure and does not lead to internal stress. There is no mechanical interaction between adjacent 180° domains.

1.3.2 Domain investigation

To understand the behavior of relaxor ferroelectrics, a lot of experimental methods are applied. By measuring Raman spectra, or by measuring the temperature dependent dielectric constant, strain, and optic index of refraction, *n(T)*, of these ferroelectrics, the electrical, thermal, mechanical, and optical properties of relaxor ferroelectrics are widely studied [Cross 1987; 1994]. It has been experimentally verified that the domain reorientation process contributes more than 70% of the total observed electrical and mechanical response in ferroelectric systems. So the domain studying plays a fundamental important role to understand relaxor ferroelectrics. There are various experimental techniques used to reveal the domain structure. Although these techniques vary from one material to another, for the given crystal geometry, with certain speed and resolution, and whether the external action, such as electric filed and temperature dependence is required.

Presently, a number of techniques have been developed for revealing domain structures. They are optical birefringence (Mill and Savage 1959); optical rotation (Dougherty, Sawaguchi, and cross 1972), Chemical etching (Fatuzzo and Merz 1967), powder techniques (Pearson and Feldman 1958), dew method (Fousek, safrankova, and Kaczer 1966), liquid crystal method (Furuhata and Toriyama 1973), X-ray topography (Niizeki and Hasegawa 1964), electronic microscope (SEM, TEM) [Beudon et al. 1985;

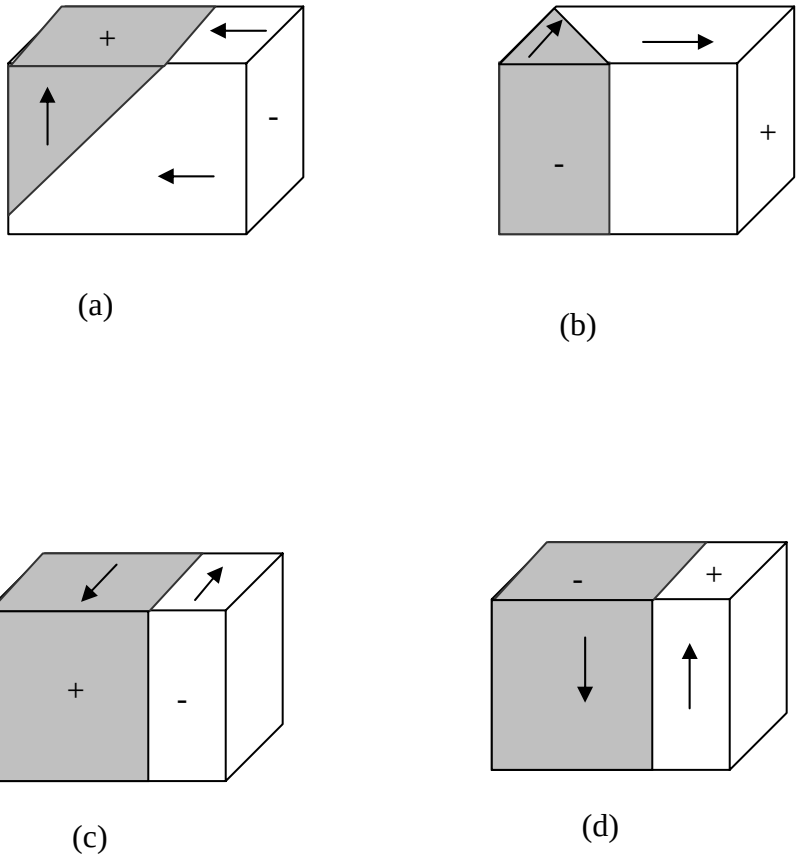

Figure1.8 Basic domain structures of $BaTiO_3$ in tetragonal phase. (a) and (b) are 90° domain structures; (c) and (d) are 180° domain structures

Hilczer and Szezesniak 1989], AFM [Haefke 1994], and so on. Optical refractive index measurement approach maybe the very convenient in-situ observation technique among these techniques.

Lithium niobate ($LiNbO_3$), lead zirconate titanate ($Pb(Zn_{1/3}Ti_{2/3})O_3$, PZT), lead zirconate Niobate ($Pb(Zn_{1/3}Nb_{2/3})O_3$,PZN), and the mixture of lead titanate (PT) and PZT are the most intensively investigated solutions.

Precise control of ferroelectric domains is a very important issue for many applications, most notably, the periodical poling of materials $LiNbO_3$, which are the basis for many powerful nonlinear optical devices, such as optical amplifiers and parametric oscillators. This makes the $LiNbO_3$ intensively investigated material [Gopalan 1998].

PZT thin film has great potential to be an ultrahigh density (100G bit/cm^2 class) medium for scanning probe microscopy-based data storages [Hidaka et al. 1996]. It is also of great benefit for the domain switching study of PZT since the domain structure will be quite simple if the orientation of the PZT thin film can be controlled along the c-axis orientation. Atomic force microscopy (AFM) and scanning force microscopy (SFM) [Gruverman et al. 1998], a generalization of AFM is usually used to study and control the local domain behaviors for their ultrahigh resolution compared with conventional techniques. Switching and backswitching, the polarization reversal in the absence of electric field, are two key issues in ferroelectric memories [Fu 2003]. Hidaka et al. [Hidaka et al. 1996] has successfully written and imaged polarized domains with a size of 40-50 nm using an AFM technique. The mechanism of backswitching, which is critical to understand the origin of polarization retention loss in ferroelectric memory, is still not clear.

PZN is known as a relaxor ferroelectric with a broad, large dielectric constant and high electromechanical coupling constant, which makes it and its mixture system (1-x) PZN-xPT, potential for applications in actuators and transducer [Kuwata 1979]. Since the domain reorientation mechanism contributes to the dielectric and piezoelectric properties, it is important to understand the domain reorientation so that the actuators and transducer properties can be tailored [Mulvihill 1995; Iwata et al. 2002]. Optical method is used since it is convenient to apply electric field and to vary temperature to study the dynamic ferroelectric domains and meanwhile making the in-situ observation also.

1.3.3 Size effect

The study of size effect on ferroelectrics has been an interesting subject both in experiment and theory. Experimental studies have reported two critical grain sizes, which have a major influence on ferroelectricity.

The first one, which occurs in the submicro size range, is characterized by a transition from multidomain to single domain grains. This transition was found to be at a critical grain size of about 200nm in $PbTiO_3$ thin films [Lu 1996], 100nm in $BaTiO_3$ powder particles [Hasiang and Yen 1996], and 300nm in $PbZr_{0.95}Ti_{0.05}O_3$ crystallites [Tuttle 1999]. The critical size was predicted theoretically by minimizing the total energy of the structure [Zhong 2001].

The second critical grain size refers to the disappearance of ferroelectric behaviors. Experimental studies have reported a critical size in the nanometer range, such as 49nm for $BaTiO_3$ thin films [Schlag and Eicke 1994], 30nm for $BaTiO_3$ powder particles [Hasiang and Yen 1996], and 7-14nm for $PbTiO_3$ thin films [Chattopanhuay 1995]. Studies of single-crystalline $PbZr_{0.25}Ti_{0.75}O_3$ thin films reported a local

ferroelectric reponse from a film thickness as small as 4 nm, a thickness of 10 unit cells [Tybell 1999] using piezoelectric and electric-field microscope. Theoretical models have been developed to calculate and predict this critical size. The models are maybe identified in three categories. One is thermodynamic model, which is under the frame of Landau-Devonshire's theory [Scott 1988]. This model based on mean-field assumption, predicts a material dependent critical size by minimizing the free energy of the finite crystallite and taking into account the contribution of volume and surface terms. Secondly, the model [Ghosez and K. M. Rabe 2000] is based on first-principle calculations, predicts ferroelectric behaviors in ultrathin $PbTiO_3$ films with a thickness as low as three unit cell. Another model [Zhong 1994] is originated from Ising model in a transverse field, taking into account surface effect and effects of depolarization fields among others. Recently Koray et al. [Akdogan 2002] proposed a phenomenological theory of size effects on the Cubic-Tetragonal phase transition in $BaTiO_3$ nanocrystals, which considered sized effects as an intrinsic phenomenon on the basis of size dependent spontaneous polarization and strains.

It's evident that grain size plays a role in the phase transition. Can this size effect be probed by optical method; say the light with different frequency may have different interactions with the same size grain? With this basis, the optical interaction with the nano/microregion in relaxor is also under the thesis's scope.

1.4 Review of the various models of relaxor ferroelectrics

There are various theories proposed to understanding the behaviors of relaxor ferroelectrics materials. Usually some of the properties can be explained by each theory.

None of them can describe all the properties. Moreover, these theories sometimes contradict with each other.

1.4.1 First principles calculation

There are still lots of unsolved questions for researchers who are exploring the origin of ferroelectricity, such as, why $SrTiO_3$ is not ferroelectrics while $BaTiO_3$ and $PbTiO_3$ are ferroelectrics although they have the same structure and chemical properties [King-Smith 1994]. Maybe the final answer can be found by means of the first principles calculation. This was extremely difficult about twenty years ago. The understanding of ferroelectrics with first principles has been significantly advanced in the last ten years with the development of electron density function and the application of powerful high-speed computer [Wu 2003].

First principles calculation starts from the fundamental interactions among electrons and nuclei, not from the experimental data used as constrain parameters. Solid is considered as a multi-particle system consisting of electrons and nuclei. The total energy of the system is calculated by solving the Schrödinger equation. The system state is then determined by the total energy and the electronic structure. Comparing with soft-mode theory, concerning the movement of ions but omitting the contribution of electrons by the adiabatic approximation, first principles emphasized the contribution of electrons, the medium between ions' interaction.

Most of the first principles methods applied to ferroelectric are based on density functional theory (DFT) and some are based on Hartree-Fock theory . The DFT states that the ground state properties of a system are given by the charge density using an effective exchange-correlation potential (V_{xc}) that accounts for electron interaction from

the view point of quantum mechanics. The main difficulty within DFT is how to treat the exchange-correlation potential since the exact form of it remains unknown. The local density approximation (LDA) takes the exchange-correlation potential from the uniform electron gas at the density for each point in the material. Two classes of methods usually used to solve to LDA equation are pseudopotential method and all-electron method. The LDA predicts many properties of ferroelectrics, such as phonon frequencies, ferroelectric transitions, polarization, and elasticity etc [Cohen 1999]. The generalized gradient approximation (GGA) including the effect of local density gradient in the density, tends to improve upon LDA in many aspect, such as atomic energies and structural energy differences.

Weyrich et al. [Weyrich 1990] calculated the electronic structure and total energy of $BaTiO_3$. Their calculation indicated that any lattice distortion lowering symmetry would change the non-overlap electronic state to overlap state. Calculated total energy supported that the different behavior of $BaTiO_3$ and $SrTiO_3$ is due to the volume effect.

Cohen[Cohen 1990] showed that there was an overlap between electron wave functions of Ti 3d and O 2p, and the overlap was enhanced by ferrodistortion, by calculating the densities of state in valence band of $BaTiO_3$ and $PbTiO_3$. This is agreed with Weyrich's [Weyrich 1990] result. Cohen also suggested that hybridization between Ti 3d and O 2p was necessary to exhibit ferroelecticity for ABO_3 perovskite ferroelectrics. It is the hybridization between Ti 3d and O 2p that reduces or balances the short-range repulsions, which tend to stabilize crystals with respect to off-center displacement.

Using an effective Hamiltonian and Monte carlo method, Garcia and Vanderbilt [Garcia 1998] studied piezoelectric response of $BaTiO_3$ as a function of applied field and

temperature. They obtained good agreement with the temperature dependence of piezoelectric constants, and found a field induced rhombohedral to tetragonal phase transition at very large fields. Rabe and Cockayne [Rabe 1998] used an effective Hamiltonian for $PbTiO_3$ and calculated piezoelectric constant d_{33} as a function of temperature using Monte Carlo, also finding good agreement with the experimental temperature dependence, which peak strong at the ferroelectric phase transition.

It will be a challenge to apply these methods to compute relaxor system, but models can be parameterized using first principles results and Monte Carlo simulation could be used to simulate rather small disorder system. To simulate much larger, mesoscopic system, it maybe necessary to parameterize models for interactions between nanoregions, leaving the atomic domains all together.

1.4.2 Compositional fluctuation model theory

One of the earliest accepted models for the understanding of relaxor ferroelectrics proposed by Smolenskii and Isupov [Smolenskii and Isupov 1954] and advanced by Isupov [Isupov 2003] continuously was based on compositional fluctuations. This model suggested that ferroelectric relaxors have a common characteristic of two or more cations occupying equivalent crystallographic sites in the lattice structure. These fluctuations could result in different local Curie temperature ($T_{C,loc}$), where the polar nanoregions in the order of ~10nm are formed, in microregions due to the dependence of the Curie temperature on the concentration of the components. These microregions are large enough to allow the occurrence of spontaneous polarization P_s in it in the absence of P_s in the surroundings. Polar nanoregions with different $T_{C,loc}$, sizes, dipole moments, spontaneous deformations and activation energies of depolarization, are distributed

randomly within the crystal in the vicinity of Curie range. The relaxor ferroelectrics is regarded as an ensemble of polar nanoregions chaotically arranged in the crystal as shown in Figure 1.9. In the Curie range the polar nanoregions are surrounded by the paraelectric phase. The number of polar nanoregions increases upon cooling. The small polar nanoregion sizes cause large $T_{C,loc}$ fluctuations. If the crystal temperature is approximately equal to $T_{C,loc}$, the local temperature alternately increases and decreases due to the polar nanoregion temperature fluctuation. Consequently the polar nanoregions will alternately disappear and reappear accompanying with losing and gaining P_s respectively. Thus the direction of P_s in a reappearing polar nanoregion could differ from the preceding one, i.e. the vector P_s could jump to another equilibrium direction while through a state with zero polarization, which explains the relaxor behavior in the Curie range.

The interaction in the crystal also is considered. The interaction includes electrostatic interaction and mechanical stress between polar nanoregions and their paraelectric surroundings. The paraelectric interlayers are strongly deformed and delay the merging of polar nanoregions with parallel P_s and the formation of ferroelectric macrodomains on cooling.

Assuming that the local temperature $T_{C,loc}$ has Gaussian distribution:

$$f(T_{C,loc}) = \exp[-\frac{(T_{C,loc} - T_m)^2}{2\delta^2}] \qquad (1.4.1)$$

where T_m is the dielectric maxima temperature, δ is the width of temperature distribution.

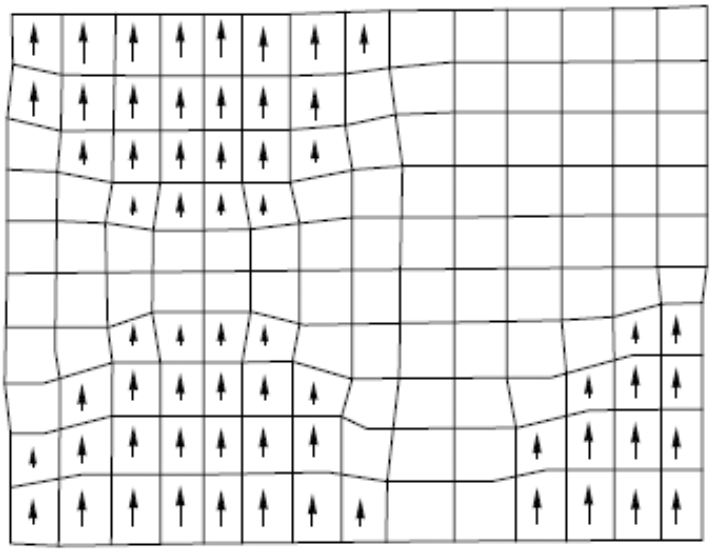

Figure 1.9 The polar regions in the paraelectric environment (from [Isupov 2003]

$$\frac{1}{\varepsilon(T)} = \frac{\int_0^\infty \frac{1}{\varepsilon(T, T_{C,loc})} f(T_{C,loc}) dT_{C,loc}}{\int_0^\infty f(T_{C,loc}) dT_{C,loc}} \tag{1.4.2}$$

Assuming that the phase transition of polar nanoregion is of first order and Curie-Weiss law is hold for $\varepsilon(T_{C,loc})$, i.e.

$$\frac{1}{\varepsilon_r(T_{C,loc})} = \begin{cases} -\frac{4}{C}(T - T_m) + \frac{16}{3c}(T - T_m)\{1 + [1 - \frac{3(T - T_m)}{4(T_{C,loc} - T_m)}]^{1/2}\}, T < T_{C,loc} \\ \frac{T - T_m}{C}, T > T_{C,loc} \end{cases} \tag{1.4.3}$$

Considering two extreme cases:

(i) $\delta >> T - T_m$, corresponding to high degree of diffuse phase transition:

$$\frac{1}{\varepsilon_r(T)} = \frac{1}{\varepsilon_{rm}} \exp[-\frac{(T - T_m)^2}{2\delta^2}]. \tag{1.4.4}$$

Expanding the exponent into a power series in terms of $T - T_m$ and dropping the higher order terms.

$$\frac{1}{\varepsilon_r(T)} - \frac{1}{\varepsilon_{rm}} = \frac{(T - T_m)^2}{2\varepsilon_{rm}\delta^2} \tag{1.4.5}$$

This is the Curie - Weiss square law, which holds for relaxor ferroelectrics.

(ii) $\delta << T - T_m$, corresponding to low degree of diffuse phase transition:

$$\frac{1}{\varepsilon_r(T)} \propto T - T_m \tag{1.4.6}$$

This is the Curie - Weiss law, which holds for normal ferroelectrics.

This model gives the most direct explanation of the broad diffuse phase transition by the existence of polar nanoregions, generally accepting by other models. The weaknesses [Randall and Bhalla, 1990a]of this model are as follows:

(i) It can not make a distinction between compounds and solid solutions with mixed cation sites and also their tendency to exhibit normal or relaxor behavior; or why so many nonrelaxor ferroelectrics have a diffuse phase transition.

(ii) Localization of polar nanoregions requires enough gradient of chemical composition, this is controversial with the Gaussian distribution assumption about the local temperature, resulting fine variations in chemical composition through the crystal.

1.4.3 Superparaelectricity model theory

A theory proposed by Cross [Cross 1987] in analogy with superparamagntic cluster materials is based upon the view that polarization clusters exist metastably or in terms of kinetic disordering. The alternative polarization states, $+P$ and $-P$, which are superparaelectric potentials of a polar cluster (comparing with Isupov's term 'polar region', here using 'polar clusters'), are separated by an activation barrier as illustrated in Figure 1.10. The height of the barrier H is proportional to the volume V of the polar region itself. Due to the composition heterogeneity the composition gradient would not be identical along these two opposite directions, thus the two potential wells have different depth. For low thermal energies the polarization will lock-in to a particular orientation and form a polar microdomain or cluster. Apparently the lower well A has the priority for polar cluster to stay. However, the polar orientation can be perturbed from the lower well A, which would lead to dispersion in dielectric response. A flipping of the polarization orientation from one state to another state could happen for sufficient thermal energy. The flipping frequency ν is given by:

$$\nu = \nu_D \exp(-\frac{H(V)}{k_B T}) \ . \qquad (1.4.7)$$

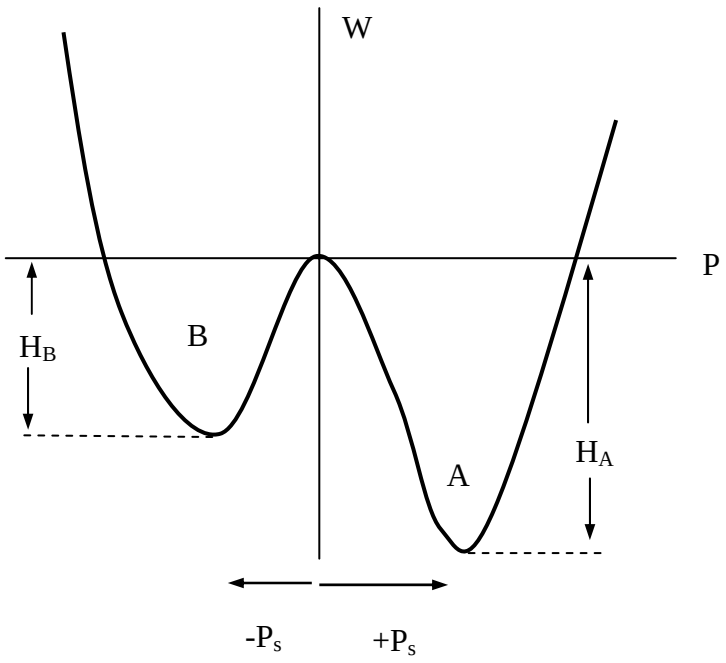

Figure 1.10 Schematic representation of superparaelectric potential describing the polarization states $+P_s$ and $-P_s$

where ν_D is Debye frequency (~10^{11}-10^{13}Hz), k_B is Boltzman constant. Since $H_A > H_B$, one can expect that the polar region will stay in well *A* longer, i.e. $+P_s$ has longer "show time". Isupov [Isupov 1999] obtained preexponential factor $\nu_D \sim 10^{40} Hz$, activation energy $H(V) \sim 7eV$, both of which are physically unrealistic for simple thermally activated polarization fluctuation. However, by extrapolating Cole-Cole plots Isupov obtained activation energy on the order of k_BT with a preexponential factor of 10^9 Hz. He ascribed the dielectric relaxation to temperature dependence of the number of polar regions.

With the analogy with magnetization behavior in superparamagnetic material, the polarization of an ensemble of uniform noninteracting polar regions having uniaxial symmetry can be described by:

$$p = \tanh(\frac{EP}{k_BT}) \qquad (1.4.8)$$

where *p* is the reduced or normalized polarization, E, the electric field, P, the dipole moment of the polar region. If *p* at different temperature is plotted against *E/T* (rather than *E*), all the curve should superimpose on one another. The implication of the superposition is that at higher temperature it takes much more electrical energy to align the moments against the thermal energy.

The superparaelectric model, without incorporating the coupling between polar regions, accurately describes many of the observed properties of ferroelectric relaxors such as the frequency dependence of the permittivity, dielectric aging, metastable switching from micro to macro domain states, and the nonlinear behavior of the thermoelastic and optical properties [Cross, 1987].

The nanoscale order domains act as natural site to localize the high temperature superparaelectric polar clusters within a paraelectric matrix on a scale of ~10nm. This is consistent with the size of polar nanregion in Isupov's model. So here polar cluster is exactly the polar nanoregion. So the broad diffuse phase transition also ascribed to the size distribution of the polar clusters.

One advantage of this model over compositional fluctuation model is that the scale of B-site order allows distinguishing whether a material will exhibit normal or realxor ferroelectric behavior.

1.4.4 Dipolar glass model

The dipolar glass phase is characterized by two temperatures, T_d, Burns temperature (or dipole temperature) [Burn, 1985], and T_f [Viehlandet al, 1990b], freezing temperature. The relaxors exhibits glassy behavior between these two characterization temperatures. However, these two characterization temperatures are from different evidence. It is interesting to put them together, although they are proposed independently.

Burns and Dacol [Burn, 1985; Burns et al., 1983a,b, 1985, 1986, 1990a, b, c] made comprehensive study on materials with both complex perovskite structure and tungsten bronze structure by accurate measurement of optical refractive index, thermal expansion, and Raman spectrum. They found that up to hundreds degrees above T_m, where the index deviates from a high temperature linear behavior, a local random polarization (or glassy dipolar) still exist in the relaxor system. In the temperature range from T_m to T_d, the average polarization $\bar{P}$ is zero, but the root mean square polarization $(\bar{P^2})^{1/2}$ is not zero.

Burns and Dacol's [Burns, 1985] the idea of composition fluctuations is transformed. From their experiment fact that T_d , the dipole temperature, is approximately the same as the T_c of the end member, $AB'O_3$ of the mixed system $A(B'B'')O_3$, they concluded that in mixed system $A(B'B'')O_3$ the local polarization begins to appear at the temperature $T_d >> T_m$ in the region containing only B' (but not B'') ions. The idea of composition fluctuations is transformed. From their experiment fact that T_d , the dipole temperature, is approximately the same as the T_c of the end member, $AB'O_3$ of the mixed system $A(B'B'')O_3$, they concluded that in mixed system $A(B'B'')O_3$ the local polarization begins to appear at the temperature $T_d >> T_m$ in the region containing only B' (but not B'') ions. One can infer that the polar region must be very small and only containing several unit cells (~1nm). However, this is contradictory to Smolenskii's model that the polar region can not be smaller than a critic size (~10nm).

The superparaelectric model was extended by Viehland et al. [Viehland et al., 1990a, 1990b, 1991] as dipolar glass models to account for polar cluster interaction in analogy to magnetic spin glass. By fitting the frequency and temperature dependent dielectric constants with Vogel-Fulcher relation

$$f = f_0 \exp(-\frac{E_a}{T_m - T_f}) \tag{1.4.9}$$

where T_f is the static freezing temperature, E_a the activation energy, f_0 the Debye frequency. The extrapolated values of freezing temperature usually are very close to temperature of the collapse in the remnant polarization [Viehland et al., 1990b]. The fundamental difference between glassy dipole freezing and thermal localization process in superparaelectrics is that freezing is a cooperative performance while the thermal localization is an independent behavior. This cooperative performance is believed to be

an indication of interactions between polar regions. The local field of a polar region has the tendency to polarize its neighboring polar regions over a correlation radius. Neutron scattering experiments [La-Orauttapong,et al, 1999] reveals that this correlation radius is temperature dependent.

These models successfully explained the polar dynamics and their extreme slowing down at the diffuse phase transition. However, they are not capable of describing the ferroelectric symmetry breakdown on a nanometric scale [Mathan,et al, 1991]. The Vogel-Fuclcher relation is not the only one that can describe the frequency and temperature dependence dielectric constants. A superexponential function proposed [Cheng,et al, 1996] also can fit well with experiment results in the range of its physical significance, though the physical origin is not clear. More over, the Vogel-Fuclcher relation can be directly derived as a consequence of other means, such as, the activated dynamic scaling concept of the random fields Ising model [Kleemann, 2002]; gradual broadening of the relaxation time spectrum as the temperature decreases [Tangantsev, 1994]; random fields distribution with GF model [Glinchuk,et al, 2001], but without the assumption of freezing in the system.

1.4.5 Random fields theory

A spherical cluster glass model or spherical random-bond-random-field (SRBRF) [Pirc and Blinc, 1999, 2000] model involving both random bonds and quenched random fields has been recently proposed. In this model, relaxor ferroelectric is regarded as an intermediate state between dipole glasses and normal ferroelectrics. In contrast to dipolar glasses, where elementary dipolar moments exist on the atomic scale, the relaxor state is characterized by the presence of nanoscale polar cluster of variable sizes. This picture

constitutes the basis of the superparaelectric model [Cross, 1987] and of the more recent reorientable polar cluster model of relaxor [Vugmeister and Rabitz, 1998]. The long-range frustrated intercluster interaction of a spin-glass type is also taken into account into this picture. The system can be described by the pseudospin Hamiltonian:

$$H = -\sum_{ij} J_{ij} P_i P_j - \sum_i h_i P_i \,. \qquad (1.4.10)$$

Here the first sum is the interaction between the dipole moments (pseudospin) P at lattice site i and j that are coupled by interaction constants J_{ij} with Gaussian distribution. The second sum denotes the interaction of the dipole moments P_i (pseudospin) with quenched random field h_i, where $\sum h_i = 0$, but $\sum h_i^2 \neq 0$. The electric dipoles random distributed in the system were treated as the main souses of random fields.

This model is capable of elucidating the static behavior of relaxors, such as the line shape of quadrapole nuclear magnetic resonance (NMR) in PMN [Blincet al,1999] and PST [Blincet al, 2000], and the sharp increase of the quasistatic third-order nonlinear dielectric constant [Bobnaret al, 2000]. This model has been extended to describe the dynamic of relaxor ferroelectrics by introducing Langevin-type equation of motion [Pircet al, 2001].

By reviewing these models, one can conclude that microscopic chemical fluctuation is the original cause of the diffuse phase transition; based on the superparaelectric model, the interaction between polar regions or polar cluster should be carefully considered. One key issue in understanding relaxor behavior is the mechanism of polar cluster formation.

1.5 Optical properties

In this section some basic concept, such as energy bandgap, optical refractive index, birefringence, and so on, will be introduced, as well as related work to this thesis.

1.5.1 Energy band theory

Principally the understanding of the optical properties of material is highly dependent on their electronic energy band structure, which can be computed by means of first principles calculations. There is a lot of progress achieved in this area recently with the development of electron density function and the application of powerful high-speed computer [Cohen, 1999]. Comparing with the huge family of ferroelectrics, the results, however, are still sparse and limited on a few samples only.

One interesting aspect of energy band of ferroelectrics is that the band can be shifted by the crystal polarization. Using the polarization-potential tensor concept introduced by Zook and Casselman [Zook and Casselman, 1966], the shift of the energy band is given by:

$$\Delta E_g = \sum_{ij} \sigma_{ij} P_i P_j \tag{1.5.1}$$

where σ_{ij} are polarization potential tensor with unit $eV \cdot m^4 C^{-2}$, which describes the Stark–like shift of the electronic energy band of a ferroelectric due either to an applied field or to a spontaneous polarization.

In oxygen-octahedra ferroelectrics, for light polarized parallel (||) to and perpendicular (⊥) to the *P* axis, the band shift is:

$$\Delta E_{g\parallel} = \sigma_{11} P^2$$

$$\Delta E_{g\perp} = \sigma_{12} P^2 \tag{1.5.2}$$

The energy band should also dependent on temperature since the spontaneous polarization is a function of temperature. Thus the energy band plays an important role in the refractive index, birefringence, thermo optical properties, and transmission spectra.

1.5.2 Optical refractive index

1.5.2.1 Introduction

The dielectric constant (or permittivity) is the basic parameter of a dielectric describing its properties from the point of view of the process of its polarization or the propagation of electromagnetic wave in it, or the process of its interaction with an electric field. In Maxwell's macroscopic theory, the problem of the interaction of electromagnetic wave with a material is reduced to the solution of Maxwell's equations for definite conditions at the boundary between the media in which the wave propagates. For the vast majority of transparent dielectric materials in the range of optical frequency of electromagnetic wave, the phase velocity of these waves is

$$v = c / \sqrt{\varepsilon} \,. \tag{1.5.3}$$

Optical refractive index is defined as the ratio of the velocity of electromagnetic waves in vacuum, light velocity *c*, to velocity of these waves in the medium

$$n = c / v \tag{1.5.4}$$

The value of the refractive *n* depends on the frequency of light and the state of material (its temperature, density, etc.). From equations (1.5.3) and (1.5.4) the index of refraction is related to the dielectric constant by the expression:

$$n^2 = \varepsilon \tag{1.5.5}$$

Optical refractive index is the most direct parameter to study optical properties. The electronic excitation spectrum of a substance is generally described in terms of a frequency dependent complex dielectric constant

$$\varepsilon(\omega) = \varepsilon_1(\omega) - i\varepsilon_2(\omega) \tag{1.5.6}$$

The real and imaginary parts relate with each other by the well-known Kramers-Kronig (K-K) relation since they are causal response function.

$$\varepsilon_1(\omega) - 1 = \frac{2}{\pi} P\int_0^{\infty} \frac{\omega' \varepsilon_2(\omega')}{\omega'^2 - \omega^2} d\omega' , \tag{1.5.7}$$

$$\varepsilon_2(\omega) = -\frac{2\omega}{\pi} P\int_0^{\infty} \frac{\varepsilon_1(\omega') - 1}{\omega'^2 - \omega^2} d\omega' , \tag{1.5.8}$$

where *P* denotes the principal part. In materials exhibiting a bandgap, the real part in the transparent region (non-absorption) is given by the optical absorption above the gap:

$$\varepsilon_1(\omega) - 1 = n^2(\omega) - 1 = \frac{2}{\pi} P\int_{\omega_t}^{\infty} \frac{\omega' \varepsilon_2(\omega')}{\omega'^2 - \omega^2} d\omega' , \ \omega > \omega_t \tag{1.5.9}$$

where ω_t is the threshold frequency, and n is optical refractive index. The frequency ω is assumed to lie above all lattice vibrational modes. Usually a few adjustable parameters need to be introduced into energy band calculation in order to compute equation (1.5.9), thus some practical difficulties are also introduced, especially for ionic materials. It is useful to adapt approximation method to calculate equation (1.5.9) with some physically meaningful parameters. These parameters depend on the particular approximation being made.

Phillips and Van Vechten [Phillips and Van Vechten, 1969] used the Penn model [Phillips, 1968] describing the static electronic dielectric constant to define an average energy gap E_g. Wemple and DiDomenico [Wemple and DiDomenico, 1969] used a

single- oscillator description of the frequency dependent dielectric constant to define a parameter E_d, so called dispersion energy. The latter approximation has been applied to vast dielectric materials including lots of ferroelectrics with oxygen-octahedra successfully

1.5.2.2 Sellmeier Formulation

Wemple and DiDomenico's single oscillator model originated from the well-known Sellmeier formulation, governs the simple dispersion in the region of low absorption:

$$n^2(\omega) - 1 = \sum_i \frac{f_i}{\omega_i^2 - \omega^2}, \tag{1.5.10}$$

where atoms are treated as dipole oscillators of strength f_i and intrinsic frequency ω_i. This equation separates the important innerband optical transitions into individual dipole oscillators. Equation (1.5.10) can be rewritten in terms of wavelength λ,

$$n^2(\lambda) - 1 = \sum_i \frac{S_i \lambda_i^2 \lambda^2}{\lambda^2 - \lambda_i^2}, \tag{1.5.11}$$

where S_i is a strength factor. One can obtain different dispersion formulas using various long wavelength approximations. The most typical is to assume that one oscillator dominates and combine the other oscillators together into a constant *A*

$$n^2(\lambda) - 1 = A + \frac{B\lambda^2}{\lambda^2 - C} \tag{1.5.12}$$

This equation fits the refractive index dispersion quite well for most of materials. However, the resulting curve-fitting parameters *A*, *B*, and *C* have no special physical significance.

In equation (1.5.11), the summation over oscillators λ_n can be approximated by isolating the lowest energy oscillator (first term) and combining the remaining terms in the form $\sum_{i\neq 1} \frac{S_i \lambda_i^2 \lambda^2}{\lambda^2 + \lambda_i^2}$. Combining these higher-order contribution with the first-resonant oscillator and retaining terms to order λ^2 one then yields the single oscillator approximation:

$$n^2(\lambda) - 1 = \frac{S_0 \lambda^2 \lambda_0^2}{\lambda^2 - \lambda_0^2}. \tag{1.5.13}$$

where λ_0 is an average oscillator position and S_0 is an average oscillator strength, both of which differ in general from any specific oscillator defined in equation (1.5.11). A more general form of equation (1.5.13) is

$$n^2(E) - 1 = \frac{E_0 E_d}{E_g^2 - E^2} \tag{1.5.14}$$

where E is energy of light, E_0 is average energy of effective dispersion oscillator, and E_d is dispersion energy.

Equation (1.5.12), which involves three parameters, is intrinsically capable of numerically fitting the dispersion of the refractive index to higher accuracy than equation (1.5.14). However, the equation (1.5.14) with the physical significant oscillator parameters E_d and E_0 is more preferable. In addition to the single oscillator form given by equation (1.5.14), many other curve-fitting forms involving two, three or more parameters have been used in the literature to describe the refractive index dispersion data. In general, no physical significance has been attached to the parameters, and the expressions serves as interpolation formulas.

Schlarb and Betzler [Schlarb and Betzler, 1993] proposed generalized Sellmeier equation which described the refractive indices of $LiNbO_3$ as a function of composition, wavelength, and temperature. The equation consisted of two approximated oscillator terms for infrared and plasmonic contributions and two terms representing Nb on a Nb site and Li site. Calculation verified that the equation gave an accurate description of the refractive indices in the composition range from 47 to 50 mol% Li_2O, in the wavelength range from 400 to 1200nm, and for temperature between 50 and at least 600K.

Wan [Wan et al 2003, 2004] added a quadratic term, which accounted for the IR correction, to equation (1.5.12) and fitted the refractive indices of PMN-xPT (x=0.24,0.30,0.31.0.33.0.38) with high accuracy in the low absorbtion wavelength range, namely, from 400nm to 5800nm.Ghosh [Ghosh, 1994] added another oscillator term, which accounted for the lattice absorption, to equation (1.5.12) and fitted to $KNbO_3$, BaB_2O_4 and LiB_3O_5. Zysset [Zysset 1992] added both a second oscillator term and a quadratic term to equation (1.5.12) and fitted to $KNbO_3$ in the wavelength range 400-3400nm. Abedin [Abedin and Ito, 1996] applied a seven-parameters equation including temperature term fitted $LiTaO_3$ in the region 400-4000nm between 25°C and 300°C

1.5.3 Birefringence

Birefringence exists in all solids which are not isotropic, such birefringence is known as standing birefringence. All ferroelectrics are birefringent medium since their anisotropic structure in ferroelectric state. It is considered [Kinase,et al, 1984] that anisotropy is caused by the spontaneous Kerr effect due to the strong local field induced by the spontaneous polarization, where the spontaneous lattice deformation is accompanied with the polarization. This is usually called induced birefringence. When

ferroelectrics under electric filed or changing temperature, external perturbation can cause extra birefringence due to the Kerr effect.

It is convenient to describe the optical anisotropic material by optical indicatrix which is an ellipsoid illustrating the change of the refractive index with variation direction. In a principal Cartesian axis system x_1, x_2, x_3 it has the equation

$$(\frac{x_1}{n_1})^2 + (\frac{x_2}{n_2})^2 + (\frac{x_3}{n_3})^2 = 1 \qquad (1.5.15)$$

The spontaneous changes of the refractive indices in a prototypic centrosymmtry system are given by:

$$\Delta(n^{-2})_i = \sum g_{ij} P_s^2 \qquad (1.5.16)$$

where g_{ij} are quadratic polarization optic coefficient with unit [m^4/C^2].

1.5.4 Transmission properties

Optical transmission spectrum gives straightforward information of optical bandgap of a material. It is one of the most important methods to determine a new material for optical applications.

The light intensity *I* after passing through a sample with thickness d is given by:

$$I = I_0 e^{-\alpha d} \qquad (1.5.17)$$

where α is absorption coefficient.

$$\alpha = \frac{1}{d}\log(\frac{I_0}{I}) = \frac{1}{d}\log(\frac{1}{Tr}) \qquad (1.5.18)$$

where Tr is transmission percentage.

Under the shining of light with frequency ω, electrons in valence band can be excited to conduction band given $\omega \geq E_g / \hbar$, where E_g is bandgap between valence band

and conduction band. There are two type of transition. One is called direct transition (as shown in Figure (1.11), in which electron keeps momentum unchanged, while another is called indirect transition, in which electron changes momentum by emitting or absorbing a phonon.

Theoretical calculation gives the absorption coefficient for different transition as following:

$$\alpha(\omega)\hbar\omega \propto (\hbar\omega - E_g)^n, \tag{1.5.19}$$

where $n = 1/2$, corresponds the allowed direction transition; $n = 3/2$, forbidden direction transition; $n = 2$, allowed indirection transition; $n = 3$, forbidden indirection transition. The type of transition can be determined by plotting $\sqrt{\alpha(\omega)\hbar\omega}$ vs. $\hbar\omega$. Especially for allowed indirection transition, $n = 2$, $\sqrt{\alpha(\omega)\hbar\omega}$ is linear with $\hbar\omega$. Figure 1.12 showed this type absorption at two temperatures. Each curve consist of two straight lines; the up one corresponding to emitting phonon while the down one corresponding to absorbing phonon.

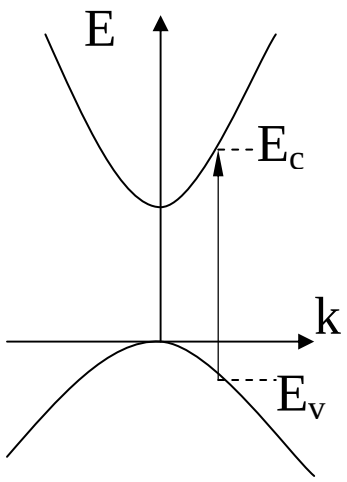

(a)

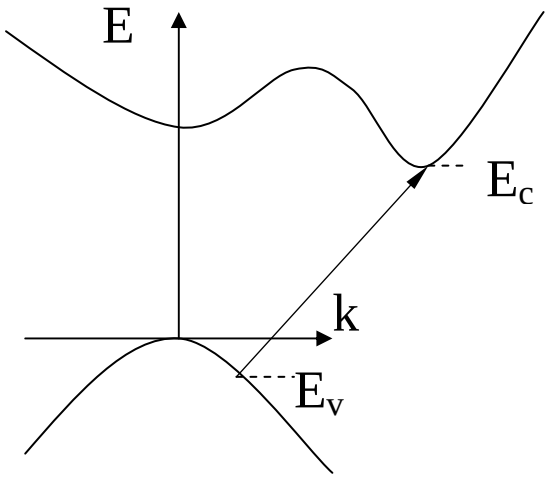

(b)

Figure 1.11 Twp type Transition (a) direct transition (b) indirect transition

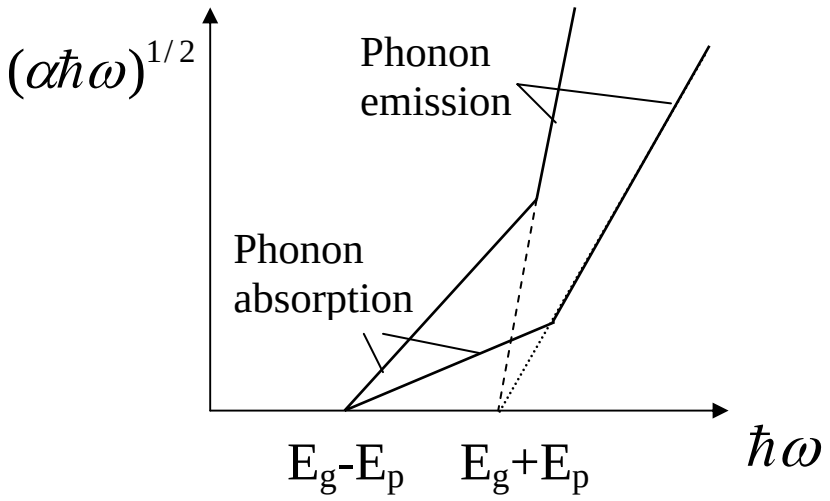

Figure 1.12 Theoretical curve of allowed indirect transition

Chapter 2

Statement of the Problem

The solid solution of ferroelectrics near morphotropic phase boundary (MPB) usually exhibits relaxor behavior, with a universal signature of diffuse phase transition (DPT). Relaxor ferroelectrics has been one of the recent intensified topics in ferroelectric community both for fundamental understanding and for technical applications [Cross 1987, 1994; Uchino 1994]. Most of the ferroelectric relaxors identified have either the complex perovskite or the tungsten bronze structure. Except for their anomalously large and temperature-insensitive dielectric constants, ideal for multilayer capacitors, they also demonstrate superior characteristics in piezoelectricity, electrostriction and electro-optic effects applicable to transducer, actuators and optoelectronic devices, practically with compositions in the vicinity of MPB.

This thesis puts emphases on the optical properties of the single crystal of PBN and PZN-PT near MPB. The reasons and the main scope are as follows:

First, PBN and PZN-PT are typical relaxors belonging to different families. The explanation of the mechanism for relaxors is still controversial as introduced in chapter 1 although a lot of progress has been made for their applications. The fact that the disordering of B-site complex cations played a key role in the phase transition characteristics for the perovskite structure [Setter 1980] while the A-site vacancy order-disorder states played a key role in the tungsten bronze structure [Guo 1989] indicates that the mechanism lies in the nanometer scale or larger. Optical wavelength in the visible range is an effective probe for nano/micro polar regions. The Burns temperature T_d marks the appearance of significant deviations of refractive index or birefringence

from a quasilinear temperature dependence [Burns 1983, 1986; Bhalla 1987]. Burns and Dacol connected this deviation with the onset of the formation of polar nanoregions (NPR). Dynamic characteristics associated with the sizes of the NPR maybe one of the significant results expected by measuring of the refractive index and birefringence of relaxors with different frequency light during phase transition. This study is much needed to deepen the understanding on relaxors through the investigation of the optical properties of PBN and PZN-PT.

Second, PBN and PZN-PT are both promising candidates for optonelectronic devices. Most of the solid state electro-optic oxides have large and fast electro-optic effects. Single crystals $LiNbO_3$ are the benchmark of electro-optic material used in telecommunication. However, the high temperature dependence and low electro-optic effect ($r_{13} = 10.6\,pm/V$, $r_{33} = 31.8\,pm/V$, $r_{22} = 7.6\,pm/V$ [Landolt-Bornstein 1996] prevented it from widespread application. Measurement already demonstrated that the electro-optic effect of PBN57 ($r_{13} = -32\,pm/V$, $r_{33} = -154\,pm/V$ [Guo 2000] and PZN-12PT ($r_{13} = 7\,pm/V$, $r_{33} = 134\,pm/V$ [Lu 2000]) are about 3~5 times of $LiNbO_3$. Some widely used electro-optic ferroelectrics are listed in Table 2.1. However, a complete understanding of the optical properties of these materials could not be achieved without their linear optical properties, including the transmission, refractive index, and birefringence as well as thermo-optic properties. From these optical properties it is also interesting to study how the optical bandgap changes with temperature and polarization.

Third, developing a system to accurately, fast, and quantitatively measure birefringence near phase transition is also our primary objective. The optical properties, especially indicatrix, of a crystal are related to its symmetry. The birefringence during

phase transition can be so small that the total phase retardation is less than π and cannot produce bright and dark fringes for some case, i.e., from tetragonal to cubic and tetragonal to tetragonal. Thus the conventional fringes pattern measurement method is not applicable [Zhu 1999,2002].

The thesis is organized according to sequence of the statements above. It includes 7 chapters.

Chapter 1 is the introduction of the background. General properties of ferroelectrics and relaxor ferroelectrics are introduced first; then some major models for relaxors are reviewed. Some basic concepts and knowledge that will be used in the latter chapters are introduced subsequently.

Chapter 3 gives the full account on the experiment results of frequency dispersion of PBN and PZN-PT near phase transition. Both refractive index and birefringence are reported. Single oscillator model is used to fit the frequency and temperature dependent refractive index with only 4 parameters. Optical Curie region is proposed and defined. Polarization is calculated with frequency and temperature dependent quadratic electro-optic coefficient.

Chapter 4 addresses the result and discussion about the thermo-optic properties.

Chapter 5 describes the transmission spectrum analysis with emphasis on PZN-PT for both poled sample and unpoled sample. Optical absorption coefficient and optical band gap are determined. Urbach rule is used to explain the difference of the absorption coefficient along the a axis and c axis.

Chapter 6 introduces the theoretical model and experimental configuration on 2D index mapping.

Chapter 7 includes the final discussion, major conclusion, and the suggestion for the future work.

Table 2.1 Some widely used electro-optic ferroelectrics

	$LiNbO_3$	$S_{1-x}B_xN$	KDP	PLZT
Coefficient	n_o=2.286 n_e=2.2 r_{13}=10.6pm/V r_{33}=31.8pm/V	n_o=2.312 n_e=2.273 r_c=205pm/V x=0.5 [Xu, 1991]	n_o=1.513 n_e=1.471 r_{41}=26pm/V r_{63} =32pm/V [Narasimhamurty, 1991]	R=9.1×10^{-16} m^2/V^2 [Uchino, 2000]
Comments	Widely used for e-o modulation application	Strongly dependent on the composition and temperature	Water soluble	Ceramic

Chapter 3

Optical frequency dependency properties near phase transition

3. 1 Theoretical background

In this chapter, frequency dependent optical properties, refractive index and birefringence of both tungsten bronze system and complex perovskite are reported.

From the classical point of view the interaction between solid material and optical waves, in form of the light dispersion, is described by Sellmeier relation:

$$n^2(\omega) - 1 = \sum_i \frac{f_i}{\omega_i^2 - \omega^2} \tag{3.1}$$

where atoms are treated as dipole oscillators of strength f_i and intrinsic electronic oscillator frequency ω_i. The index is only determined by the electronic term. Obviously n should be dependent on temperature T besides ω since ω_i is dependent on T. Including the polarization effect, the optical index of refraction should be written as:

$$n = n_{\omega_i}(\omega, T) + n_p(P) \tag{3.2}$$

where the $n_{\omega_i}(\omega, T)$ is the intrinsic part. If the polarization is spontaneous, which is dependent on temperature, $\frac{dn_p}{dT}$ will give the information of $n_p(P)$. This optical index dependent of polarization effect has been observed before and it turned out that this effect could be more significant than the intrinsic part [Bhalla 1987, 1992], in the ferroelectric temperature region.

For a perovskite structure crystal with prototype symmetry m3m, $n_1 = n_2 = n_3$ is expected since the 1,2,and 3 axis are all equivalent in symmetry, while for a tetragonal

tungsten bronze crystal with prototype symmetry 4/mmm, $n_1 = n_2 \neq n_3$, i.e. there is a standing birefringence Δn_{13}^s which is dependent upon temperature and optical frequency. Now if there is a spontaneous polarization P_r along the 3 (c) axis in a cell, this spontaneous polarization will give an additional long-range dipole-dipole interaction in this direction except the short-term repulsive forces. So the total birefringence Δn_{31}:

$$\Delta n_{31} = \Delta n_{31}^s(\omega, T) + \Delta n_{31}^p(P) \tag{3.3}$$

where $\Delta n_{13}^p(P)$ is the birefringence due to the polarization.

Generally the refractive index has appearance of a symmetritrical second-rank tensor quantity and is represented by the optical indicatrix which is described by equation 1.5.15:

$$\frac{x^2}{n_1^2} + \frac{y^2}{n_2^2} + \frac{z^2}{n_3^2} = 1 \tag{3.4}$$

With the application of an external electric field , the change in index is given by an expansion expression:

$$\frac{1}{n_{ij}^2(E)} - \frac{1}{n_{ij}^2(0)} = \sum_{ijk=1,2,3} r_{ijk} E_k + \sum_{ijkl=1,2,3} R_{ijkl} E_k E_l \tag{3.5}$$

Here $n(E)$ and $n(0)$ (n^0) are the refractive indices at E and zero field respectively, and r_{ijk} is the primary electro-optic coefficient (Pockels effect) and R_{ijkl} is the quadratic electro-optic coefficient (Kerr effect).

If using the polarization as the independent variable instead of electric field, the index change due to the polarization is given by:

$$\Delta(n^{-2})_{ij} = \sum_{ijk=1,2,3} f_{ijk} P_k + \sum_{ijkl=1,2,3} g_{ijkl} P_k P_l \tag{3.6}$$

where f_{ijk} and g_{ijkl} are linear polarization-optic coefficient and second polarization-optic coefficient respectively.

In order to obtain relationship between electro-optic and polarization-optic coefficient, let the linear term and quadratic term in equation (3.5) and (3.6) equal to each other, respectively, and using the relation between polarization and electric field,

$$P_p = \varepsilon_0 \chi_{pq} E_q = (\varepsilon_{pq} - \varepsilon_0) E_q \tag{3.7}$$

one can obtain:

$$r_{mnp} = f_{mnq}(\varepsilon_{pq} - \varepsilon_0) \tag{3.8}$$

$$R_{mnpq} = g_{mnrs}(\varepsilon_{pr} - \varepsilon_0)(\varepsilon_{qs} - \varepsilon_0) \ . \tag{3.9}$$

For a centro-symmetric prototype symmetry crystal, the linear coefficients f_{ijk} are zero; equation (3.6) can be written in contracted notation:

$$\Delta(n^{-2})_i = \sum g_{ij} P_s^2 \tag{3.7}$$

For an uniaxial tetragonal prototype ferroelectric crystal with polarization along c-axis, the induced changed in indices of refraction perpendicular and parallel to the c-axis are given by:

$$\Delta n_1 \approx -\frac{1}{2}(n_1^0)^3 g_{13} P_3^2 \tag{3.8}$$

$$\Delta n_3 \approx -\frac{1}{2}(n_3^0)^3 g_{33} P_3^2 \tag{3.9}$$

where n_3^0 n_1^0 are the index of refraction if there were no polarization of any sort present along the c axis (n_3) and perpendicular to it (n_1) respectively. If $n_3^0 \approx n_1^0 \approx n_0$, the change of optical birefringence due to the polarization will be given by:

$$\Delta n_{31}^{p}(P) = \Delta n_3 - \Delta n_1 = -\frac{1}{2} n_0^3 (g_{33} - g_{13}) P_3^2 \tag{3.10}$$

Using the model of electric field or spontaneous polarization affecting band gap of ferroelectrics [Lines and Glass 1977], which gives quadratic electro-optical coefficient g_{ij} as the formula:

$$g_{ij} = \frac{2\omega_0 B \sigma_{ij}}{h n_0^4 (\omega_0^2 - \omega^2)^2} \tag{3.11}$$

where $\omega_0 = \frac{E_g}{\hbar}$ (E_g is band gap) the lowest-energy oscillator frequency, B a constant related with oscillator strength, σ_{ij} polarization potential.

3.2 Experiment approach

3.2.1 Sample preparation

Single crystal of $Pb_{1-x}Ba_xNb_2O_6$, 1-x=0.57(PBN57) used for this investigation was grown by Czochralski method. The crystal faces were polished carefully by first using 3 micron diamond paste and then the fine grade 1~1/4 micron diamond paste until an optical finish (while using kerosene as lubricating medium). Air-dry silver electrodes for poling the sample and for dielectric constant measurement were also prepared.

The PZN-0.12PT crystals used in this study were grown using the flux method [Lim and Rajan 2004]. The single crystal was oriental along the <001> direction by using x-ray Laue back reflection. The same polishing procedure as PBN was also applied to PZN-PT crystals to an optical grade. The sample was poled at a temperature of 110°C with an electric field of 10kV/cm for 5 minutes. Then the sample was slowly cooled down to room temperature under the electric field.

3.2.2 Optical refractive index measurement

All optical refractive indices were measured by minimum deviation method with prism sample. As illustrated in Figure 3.1, the deviation angle Δ of the light beam can be expressed in terms of the incident angle i of the prism and apex angle A as:

$$\Delta(i) = i + \arcsin(n\sin(i - \arcsin(\sin i / n))) - A \tag{3.12}$$

When the beam within the prism is parallel to the base and passes symmetrically, the deviation angle has minimum $\Delta_{\min}$, and refractive index can be determined as:

$$n = \frac{\sin(\frac{A + \Delta_{\min}}{2})}{\sin(\frac{A}{2})} \tag{3.13}$$

The precision of the deviation angle is determined by the minimum vernier scale of the optical spectrometer of 20″. So the precision of the measured refractive index can be approximately as:

$$\delta n = \frac{\sin(\frac{A + \Delta_{\min} + 20''}{2}) - \sin(\frac{A + \Delta_{\min}}{2})}{\sin(\frac{A}{2})} \approx \frac{\cos(\frac{A + \Delta_{\min}}{2})}{\sin(\frac{A}{2})}\sin(10'') \sim 10^{-4} \tag{3.14}$$

In this study, the optical refractive index measurements were performed from room temperature up to around 500°C. An Oriel ultraviolet light provided white light. The white light was selected by a monochromator (Kratos Analytical) and output the desired monochromatic light at wavelength of 450, 535,633, and 694nm. Then the light was polarized by a polarizer to ensure that the real extraordinary index n_e (n_3) was measured. All the prism apex angle and minimum deviation angles were measured by Gaertner spectrometer (Figure 3.2) (Scientific Corporation) with a smallest vernier reading of 20″. The sample temperature was controlled by a lab-designed hot stage.

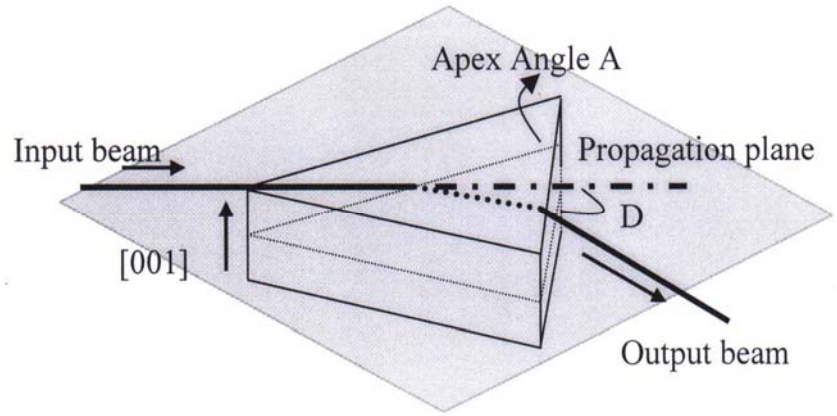

Figure 3.1 Principle of minimum deviation measurement.

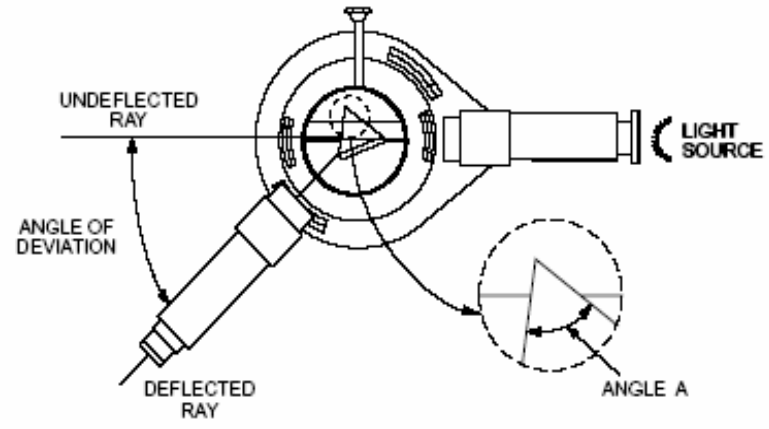

Figure 3.2 Measurement of minimum deviation angle

3.2.3 Birefringence measurement

The birefringence, Δn_{31}, was measured as function of temperature and wavelength using a wedge method based on wave interference. Δn_{31} was measured using a polarizing microscope with a hot stage and the different light sources, see experiment setup in Figure 3.3. The linearly polarized light propagating in a direction perpendicular to the optical axis was incident on the a-plate. The transmitted light after passing through an analyzer produced dark and bright fringes (Figure3.4). The birefringence was determined by

$$\Delta n_{31} = \frac{\lambda}{d \sin\theta} \tag{3.15a}$$

where θ is the wedge angle, and d is the separation between the interference fringes resulting from the varying thickness of the wedge.

From Figure 3.4, when $d > L$, L the length of sample, there will no fringes appearing on the surface of wedge sample. So, in order to using this method to measure birefringence, the birefringence must be satisfied with $d = \frac{\lambda}{\Delta n_{31} \sin\theta} < L$, i.e.

$$\Delta n_{31} > \frac{\lambda}{L \sin\theta}. \tag{3.15b}$$

More generally the value L should be the minimum of the length of sample and the width of view scope. For example the birefringence must be greater than 3.6×10^{-3} for a wedge sample with apex angle 5° and 2mm view scope at 6328nm.

The hot stage (Linksys Corpration) was controlled by computer software. The birefringence fringes images were captured by a Polariod camera (Hamamatsu) and stored in computer. Light sources were Helium-Neon laser, which provided light with

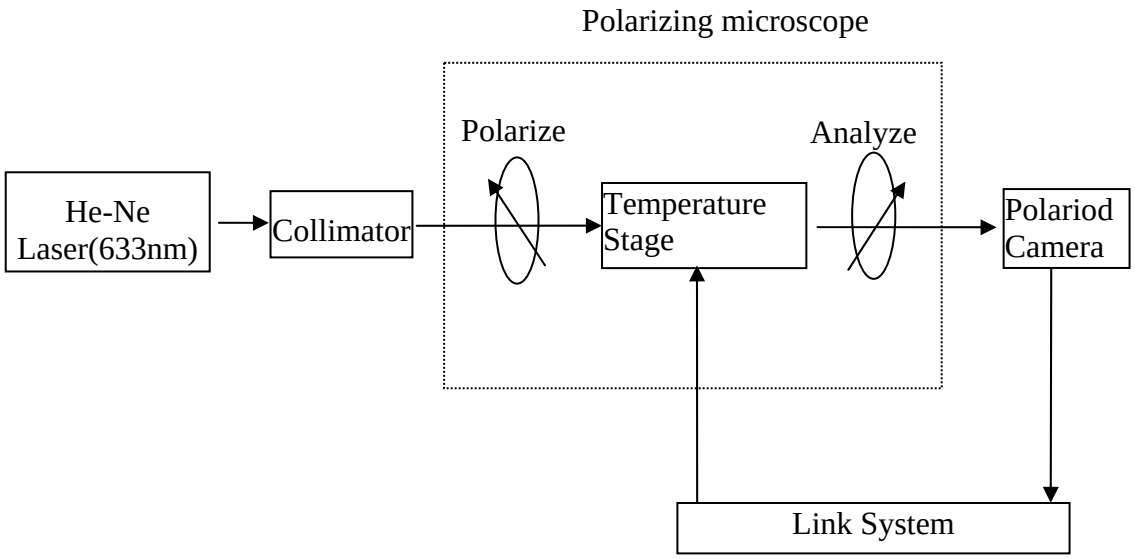

Figure 3.3 Experiment setup of Birefringence measurement

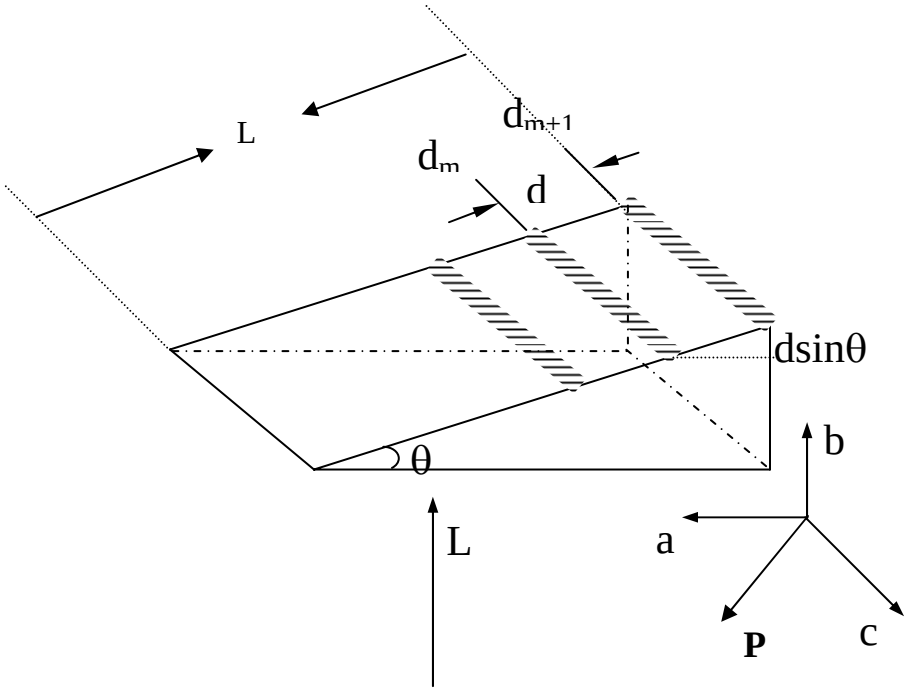

Figure 3.4 Wedge method for birefringence measurement

wavelength of 632.8nm, white light with different interference filters, providing light with wavelength of 535nm and 694nm.

3.3 Optical properties of PBN

3.3.1 PBN system and background

Ferroelectric TB is transparent in the visible range and has prototype tetragonal symmetry 4mm/m. The structure of the TB prototype is shown in Figure 1.6 as projected in the (001) plane. The tetragonal unit cell consists of 10 BO_6 octahedral linked by their corners in such a manner as to form three different types of tunnels running right through the structure parallel to the c-axis. A large number of compound crystallize with TB structure, but the variety, the size and charge of the metal cations can cause subtle changes on the ferroelectrics phases and varying characteristics of ferroelectric properties. For example, $PbTa_2O_6$ is orthorhombic both above and below T_c, whereas $PbNb_2O_6$ is tetragonal above and orthorhombic below T_c, and $Sr_{1-x}Ba_xNb_2O_6$ (SBN) remains tetragonal both above and below T_c.[Lines and Glass 1977]

$Pb_{1-x}Ba_xNb_2O_6$ (PBN[(1-x)%]) crystals have a prototype 4/*mmm* tetragonal symmetry above their Curie temperature, *Tc* . Below *Tc* , PBN has a nearly vertical morphotropic phase boundary (MPB) near $1-x=0.63$ which separates the subsolidus region into two ferroelectric phase fields with two distinct crystallographic structures, as shown in Figure 3.5. A spontaneous, reversible polarization P_r, is along the c axis (<001>) for the Ba-rich $(1-x \le 0.63)$ material, which is tetragonal 4mm structure, with only 180° domains; or perpendicular to the c axis for the Pb-rich $(1-x \ge 0.63)$ material, which has an orthorhombic *m*2*m* structure, with 180° and 90° domains [Guo et al 1990]. Like other TB materials, PBN has a high optical refractive index and the transmission covers

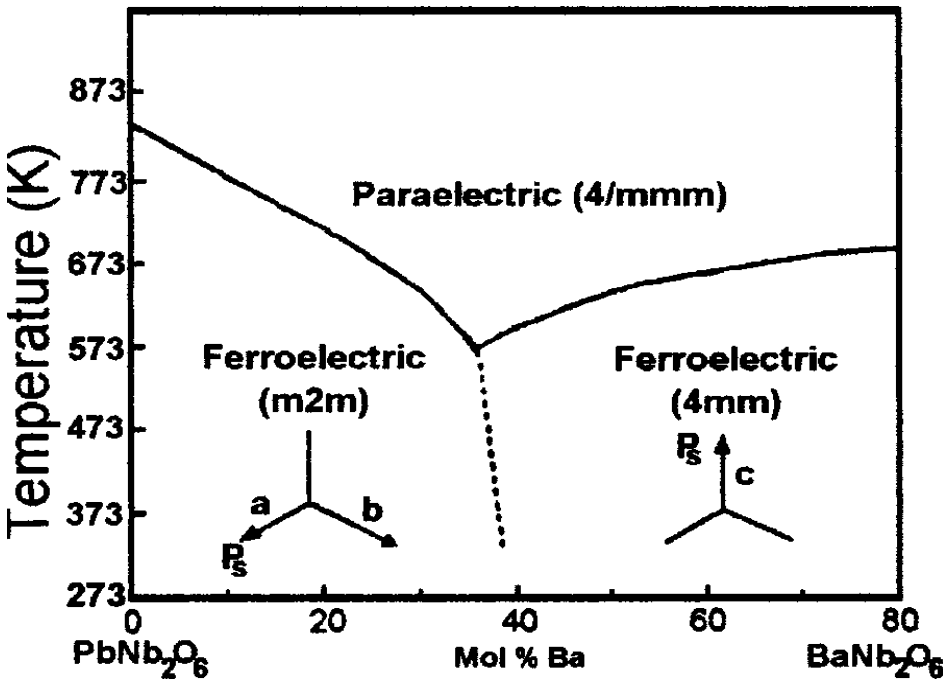

Figure 3.5 Pseudobinary PBN morphotropic phase boundary diagram [Guo et al. 1990]

roughly from 350nm to 6μm as reported for the SBN. PBN is water-insoluble, chemically stable and mechanically strong like other ferroelectric oxide octahedral structure crystal. For the compositions near the MPB, the material possesses temperature insensitive dielectric constant and polarization, which are advantageous for the electrooptic applications over a wide temperature range. Around the MPB, this material, either as single-crystal or in polycrystalline ceramic, shows high-dielectric permittivity, pyroelectric, piezoelectric, and electro-optic coefficients. All these properties make it very attractive for applications in electro-optic, surface acoustic wave, pyroelectric, and memory devices. PBN has been comprehensively studied for the ferroelectric and electrooptic properties, and the polarization mechanism [Guo et al 1989, 1990a, 1990b;Burns et al 1990; Randall et al 1991;Xiao et al 1996; Yang et al 2003; Santos 2003].

The composition quoted in the thesis as PBN[(1-x)%] where (1-x)% is the mole percent of $PbNb_2O_6$ in the $Pb_{1-x}Ba_xNb_2O_6$, refers to the post-growth analysis composition as determined by electron microprobe analysis.

One of the characteristics of relaxor ferroelectrics is the very strong frequency dependence of the electric properties. But most investigations on diffuse phase transition are limited in the radio frequencies range or lower frequencies. Here the frequency dependence of the diffuse phase transition of PBN in the optical range is studied.

3.3.2 Experiment results

3.3.2.1 Optical refractive index of PBN

The apex angle of the prism sample was determined as 5°7′. The refractive indices n_3 of PBN were measured with several visible wavelengths from room temperature to around 500°C by minimum deviation method as shown in Figure 3.6. The optical index can be described by a single oscillator model [DiDomenico and Wemple 1969a,b]:

$$n^2 - 1 = \frac{S_0 \lambda^2 \lambda_0^2}{\lambda^2 - \lambda_0^2} = \frac{E_0 E_d}{E_0^2 - E^2} \tag{3.16}$$

where E_0 is energy of effective dispersion oscillator, E_d is dispersion energy. All the constants can be determined by plotting $\frac{1}{n^2 - 1}$ against $\frac{1}{\lambda^2}$ to a straight line least square fits. Some plotting is shown in Figure 3.7 for several temperatures. The derived E_0 and E_d against temperature are plotted in Figure 3.8 and Figure 3.9, respectively. The effective dispersion oscillator energy follows Varshni's [Varshni 1967] empirical relation as:

$$E_0(T) = E_0(0) - \frac{AT^2}{B + T} \tag{3.17}$$

where $E_0(0)$, A and B are parameters to be determined. The dispersion energy can also be fitted by the similar expression:

$$E_d(T) = E_d(0) - \frac{CT^2}{D + T} \tag{3.18}$$

where $E_d(0)$, C and D are fitting parameters.

From equations 3.16, 3.17, and 3.18, an empirical expression of refractive index dependence of temperature and wavelength is obtained as:

$$n = \sqrt{1 + \frac{(E_0(0) - \frac{AT^2}{B+T})(E_d(0) - \frac{CT^2}{D+T})}{(E_0(0) - \frac{AT^2}{B+T})^2 - E^2}} \tag{3.19}$$

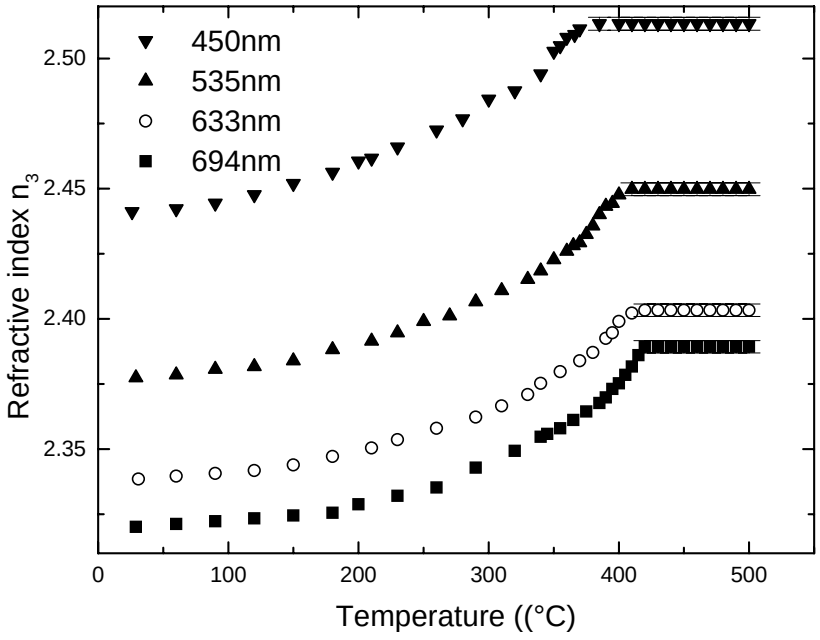

Figure 3.6 Optical refractive index n_3 of PBN57 single crystal as a function of temperature at λ=450, 535, 633, and 694nm

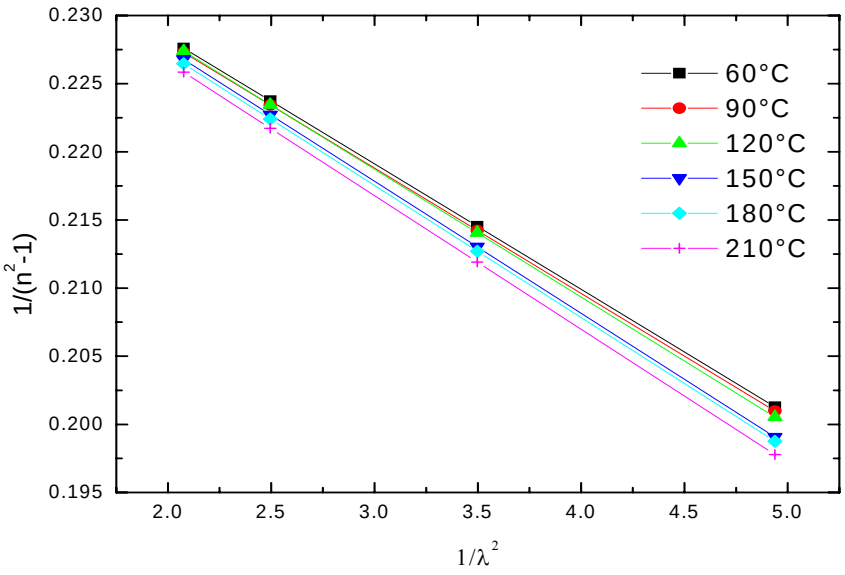

Figure 3.7 Single oscillator fitting for different temperature

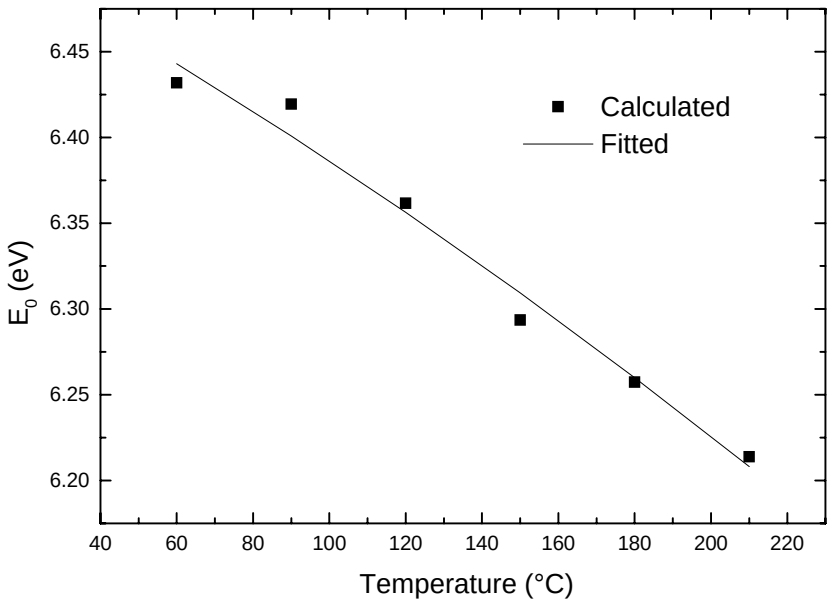

Figure 3.8 Calculated energy of effective oscillator E_0 vs temperature

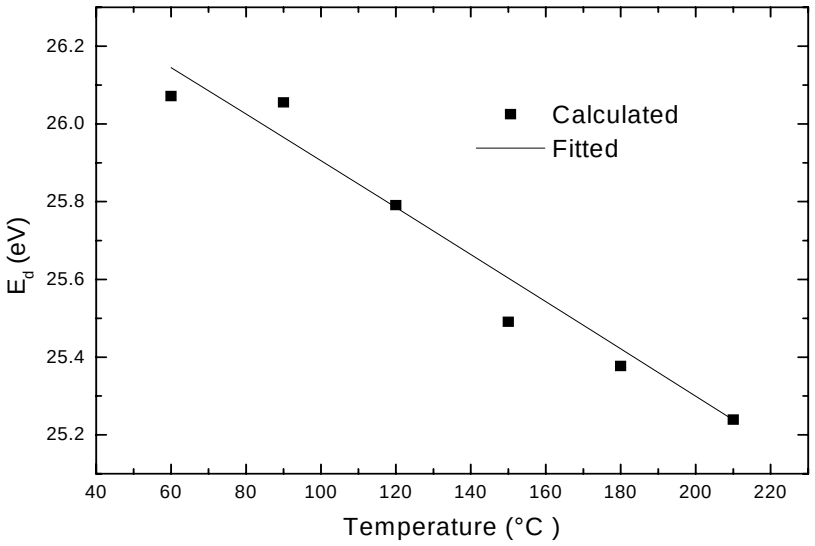

Figure 3.9 Calculated dispersion energy E_d vs temperature

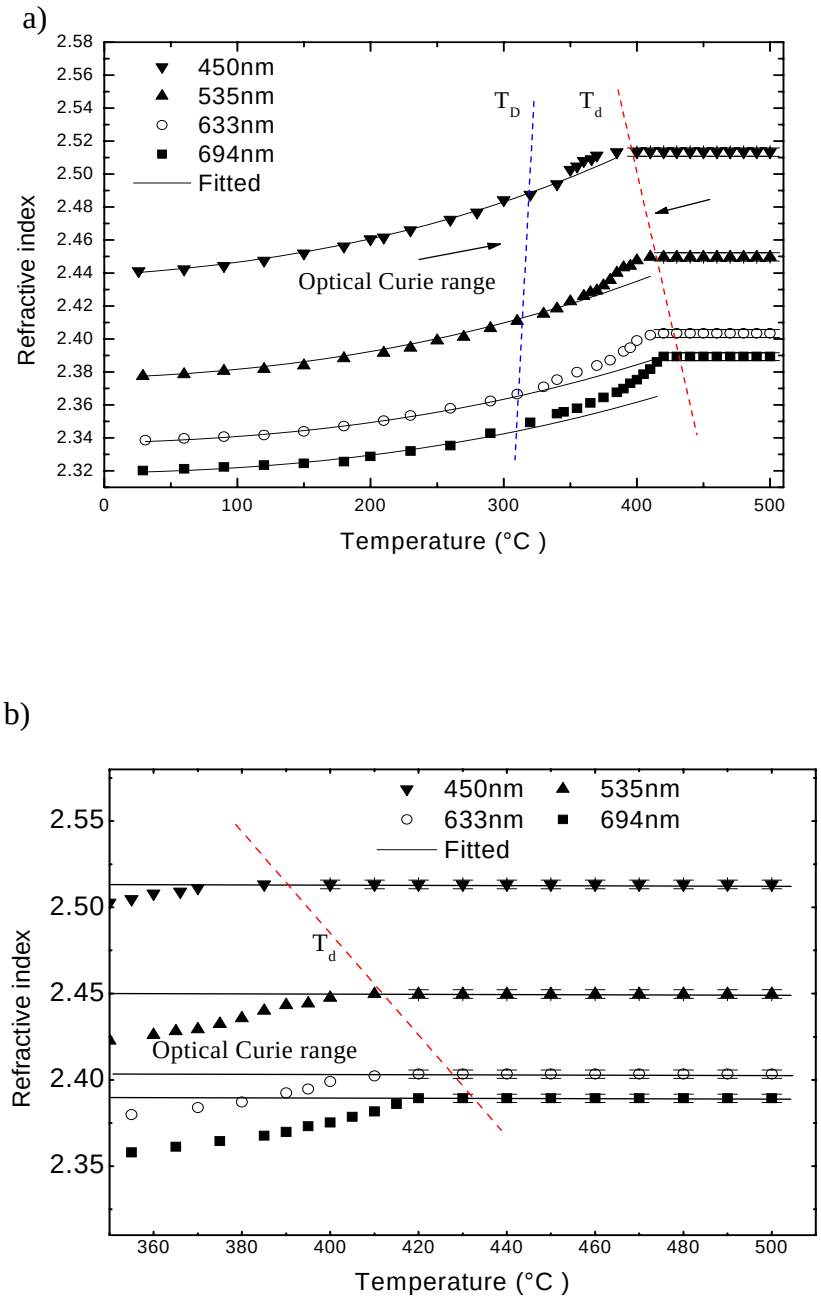

Figure 3.10 a) Experimental and calculated refractive index of n_3. The inclined lines signify the trend of T_D and T_d , obtained by extrapolation guided by the eye. b) details of T_d at high temperature

Table 3.1 Parameters from refractive index of PBN57

	694nm	633nm	535nm	450nm
Deviation temperature T_D (°C)	~320	~330	~340	~350
Burns temperature T_d (°C)	~435	~420	~410	~390
Breadth of Optical Curie region (°C)	~115	~90	~70	~40

This six-parameter refractive index empirical formula is temperature and frequency dependent, which is based on the single oscillator model with very clear physical emphasis. Once the index in the low temperature range, usually convenient to measure accurately, is known, the index in the whole temperature range which can be described by single oscillator model can be calculated.

There have been a lot of empirical formulas of refractive index [Schlarb and Betzer 1993; Abedin and Ito 1996], but almost they have no physical meaning.

Using the parameters in expressions 3.18 and 3.19, the refractive index against temperature is plotted in Figure 3.10. From room temperature to 340°C for 450nm and to 320°C for 694nm, the fitting values showed excellent agreement with experimental data. However, the index fitted deviates from the experiment data at different temperatures, denoted as T_D, well below T_m for each wavelength in ferroelectric state.

This deviation temperature from the single oscillator model, T_D, marks perhaps the breaking up of the macroscopic polar regions approaching a relaxor phase transition. T_D shifts to higher temperature for probing light of higher frequency (a similar trend is found for isotropic temperature T_i, see next section). During the phase transition process for relaxor ferroelectric, the polarization not only presents on the ionic scale as the usual elementary dipole moments of atoms, but also exists in the micro/nanoscale due to the polar regions. [Randall and Bhalla 1990a; Randall et al.1990b]. Taking into account the dipole-dipole cluster interaction between polar regions in equation 3.2, the index should

be larger than that contained in the electronic terms alone. This explains the deviation that the fitted index values are smaller than the measurement values above the deviation temperature T_D.

There is an error for refractive index at the high temperature (>400°C) range. When measuring the sample in this high temperature range, the refractive ray is not as stable as in the low temperature. However, there is no obvious change of the angle of the refractive ray in the whole high temperature range. The error is around 0.002. So the refractive index may not keep the same but has a slight slope of in the range of ± 0.000025. This error may come from the temperature fluctuation resulted from the heating couple or the structure of sample itself.

It is well known that at high temperature in paraelectric state the refractive index n_3 scales linearly with temperature and can be fitted by a linear relation with temperature. Below a certain phase transition or characteristic temperature refractive index will not follow this linear behavior. This departure-temperature is often regarded as dipole temperature or Burns temperature, T_d. [Burns and et. al. 1986,1987,1990a, b]. The Burns temperatures for different frequency are listed in table 3.1. Burns temperature marks the appearance of the local nonreversible polarization.

As mentioned above, there is an error around 0.0002 for refractive index in the high temperature range and may result a very large error of the Burns temperature. Here the start point of the unstable refractive index is regarded as Burns temperature, however, this is possibly not the truly Burns temperature. In later section 3.3.2.4 the dielectric maxima is found around 365°C for heating run. The difference between the Burns temperature derived from optical refractive index n_3 and dielectric maxima is just ~25°C

for 450nm and ~70°C for 694nm, which are much smaller than those reported in previous papers, which are usually about up to 200°C for typical relaxor ferroelectrics [Burns et. al. 1986, 1987, 1990a, b, Bhalla et. al. 1987, 1992]. One the other hand, the profile of refractive index of PBN57 is more like a 2nd order phase transition, similar as PBN50 [Burns et. al. 1990c], which is far from the MPB and is normal ferroelectrics, but rather a typical realxor transition, although PBN57 is very close to the MPB. It implies the diffuse index α is more close to 1 but rather 2. This is also supported by the later dielectric constant measurement in section 3.3.2.4 where the dielectric constant is weak dependent on frequency The difference between Burns temperature and temperature of dielectric maxima is zero for normal ferroelectric with diffuseness coefficient of 1 and several hundred degrees for "complete" relaxor ferroelectrics with diffuseness coefficient of 2. It's reasonable to assume that the difference between Burns temperature and temperature of dielectric maxima is proportional to diffuseness coefficient α. The validity of this assumption is based on the two facts. First, the diffuseness coefficient is increasing with the degree of disorder of polar regions [Setter and Cross, 1980]. Second, the Burns temperature is approximately the same as the T_c of the end member, $AB'O_3$ of the mixed system $A(B'B'')O_3$ [Burns, 1985]. With the above assumption the small difference between Burns temperature and temperature of dielectric maxima of PBN57 is accepted.

Optical Curie region is proposed to define as the temperature between the deviation temperature T_D and the Burns temperature T_d. The optical Cuie region is about 40°C for 450nm and 115°C for 694nm. All these parameters are listed in table 3.1 and plotted in Figure 3.14. It is evident that the optical Curie region broadens at lower frequency, which agrees in trend with Curie region for dielectric constant [Cross, 1987]

and that of the result of birefringence. Moreover, the width of the optical Curie region scales almost linearly with frequency.

In ferroelectric state, the wavelength of high frequency light (blue light) is closer the size of nanocluster than the wavelength of low frequency light (red light). Thus it's more effective for blue light to active the nanocluster.

3.3.2.2 Birefringence of PBN

Birefringence results of PBN obtained at wavelength of 694nm, 633nm, and 535nm are shown in Figure 3.11. All three birefringence undergo positive, zero (isotropic), and negative from high temperature to low temperature while refractive index of the PBN crystal changed from optically positive to optically negative. The higher the frequency of the light, the larger the birefringence. This is expected considering the general dispersion theory based on the model of the classical harmonic oscillator interacting with external field while the intrinsic frequency in equation (3.1) is taken as the lowest-energy oscillator frequency ω_0. For a typical ferroelectrics band gap E_g ~4-5eV, ω_0 (>10^{15} Hz) is always much greater than source light frequency ω (visible light frequency 10^{14} Hz). In the normal dispersion region when the light frequency is approaching to its intrinsic frequency of the oscillator, the electronic polarizability is high along the c-axis thus the large refractive index along the c-axis; while the refractive index along the a-axis remains approximately constant, thus positive birefringence is resulted.

A more detailed birefringence-temperature relation is shown in Figure 3.12. The optical isotropic temperature T_i increases with frequency of light. T_i in ferroelectric tungsten bronze strontium barium niobates was reported before [Bhalla, 1987, 1992, Ivanov, 2002]; however, its physical significance in relaxor materials has not been

discussed previously. Below T_i the primary contribution to Δn_{31} comes from spontaneous polarization whose characteristic resonance frequency is 2~3 orders lower than that of electronic polarization. Negative Δn_{31} is thus observed in analogous to the anisotropy of dielectric permittivity $\varepsilon_1 > \varepsilon_3$. Similarly T_m, the temperature corresponding to maximum dielectric constant at low frequency, and T_D, deviating temperature from single oscillator model (to be addressed in a later section), have the same tendency increasing with frequency.

It is well known that at high temperature in paraelectric state the birefringence is the standing birefringence that scales linearly with temperature and can be fitted by a linear relation with temperature. Below a certain phase transition or characteristic temperature birefringence will not follow this linear behavior. This departure-temperature is regarded as dipole temperature or Burn's temperature, T_d. [Burns, 1985]. This departure is nearly 100°C above the isotropic temperature T_i for the sample studied. The derived T_d and measured T_i are listed in table 3.2. T_d is also frequency dependent but in contrast to that of T_i it decreases with frequency. (T_d-T_i) is listed in Table 3.2 that decreases at higher frequency. The slopes of the fitted straight lines in Figure 3.12 also increase with frequency. It implies that light with higher frequency has higher resolution to smaller polar-regions as well. All these values are tabulated in Table 3.2.

From equation 3.3, the combination of the standing birefringence Δn_{31}^0 and the polarization-dependent part vanishes that leads to the optical isotropic condition. Standing birefringence is dominated by anisotropic ionic polarizability whose temperature dependence comes from lattice deformation. The standing birefringence is linear with temperature with a positive slope while the polarization-dependent part is of

negative dependence in ferroelectric state and gradually decreases approaching dipole temperature T_d. Before reaching to the dipole temperature T_d, the standing birefringence and polarization-dependent part compensate each other at isotropic temperature T_i. In relaxor ferroelectrics the macrodomain transforms to microdomain with increasing temperature [Yao et.al. 1984], and so do the polar regions. Considering coupling between light waves and polar regions, apparently a certain frequency will be more sensitive to some polar regions with a corresponding sizes but almost invisible to other polar regions with much different sizes. When temperature is increased, the size of polar region becomes smaller and is sensitive to light of shorter wavelength. Thus light of low frequency is more effective to probe the polar region at low temperature comparing with light of high frequency. So the frequency of the light that can sense effectively polar-regions is increasing with temperature. The statistical result of this effective interaction is that Δn_{31} approaches to zero at a lower temperature for lower frequency since the number of polar-regions of corresponding sizes decreasing at lower temperature, i.e., the isotropic temperature, T_i, increases with frequency.

From equation (3.10), the root mean square $\sqrt{\bar{P}_3^2}$ can be obtained from $\delta(\Delta n_{31})$ which is the difference between the measurement Δn_{31} and the standing birefringence Δn_{31}^s extrapolated from high temperature linear region. Here $n_1 \approx n_3 \approx n_0 = 2.32$ [Isupov, 1989], and $g_{33} - g_{13} = 0.0755\,(\mathrm{m}^4/\mathrm{C}^2)$ [Guo et al. 1990] at $\lambda = 633nm$. In order to get the quadratic electro-optical coefficient for other two frequencies, the equation (3.11) is used. Since ω_0 (>10^{15} Hz) is always much greater then ω (visible light frequency 10^{14} Hz) and not dominate on g value, the choosing of ω_0 will not change g too much. Using these parameters, the g values are calculated and listed in table 3.2.

The obtained values of P_d are plotted in Figure 3.13. . The P_d shows very weak dispersion behavior at low temperature and the typical P_d is around 0.31~0.34 C/m^2, which is comparable with other measurement 0.38~0.46 C/m^2 (PBN60) [Guo et.al. 1996]. P_d showed a decreasing tendency in low temperature range rather than approaching to a saturated polarization value as usually expected [Burns 1986]. Usually the band gap is broaden with decreasing temperature [DiDomenico and Wemple 1969], thus the larger ω_0 and smaller g is expected with decreasing temperature. While in equation (3.13) a fixed value of g for all temperature for one frequency is used, thus P_d is decreasing when lowering the temperature in the low temperature range. A correction is given in the next section after considering the temperature and dispersion dependence of g values. This is done after the n_3 directly was measured. Another possibility is that PBN is experienced a low temperature phase transition since the decreasing tendency for the three all occurs around 30~40°C below zero. The existence of the low temperature phase transition is also checked by measuring the low temperature dielectric constant and loss tangent.

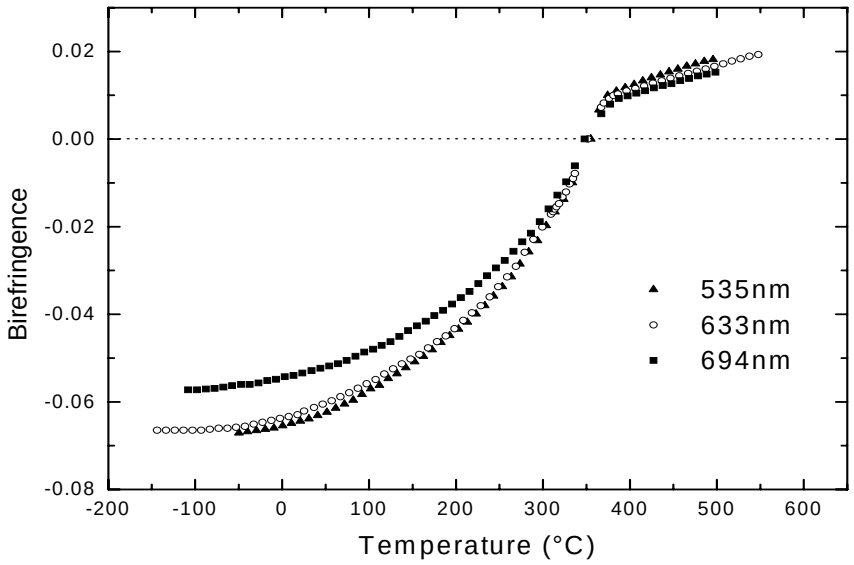

Figure 3.11 Birefringence of PBN57 as a function of temperature at λ=535, 633, and 694nm

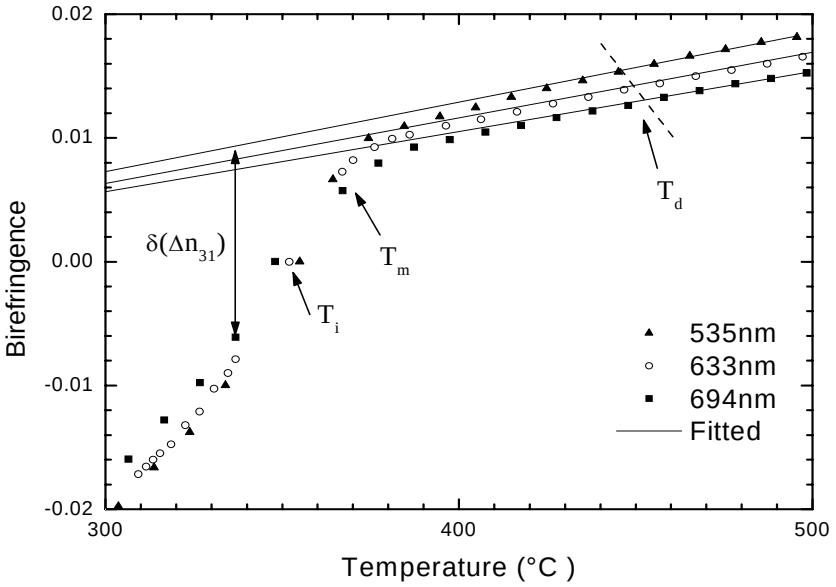

Figure 3.12 Birefringence of PBN57 vs temperature with linear extrapolating of high temperature intrinsic behavior, obtained by extrapolation guided by the eye.

Table 3.2 Parameters from birefringence of PBN57

	694nm	633nm	535nm
Isotropic temperature T_i (°C)	~347	~352	~356
Burns temperature T_d (°C)	~455	~450	~445
Slope ($\times 10^{-5}$/°C)	4.85	5.29	5.6
T_d -T_i (°C)	~108	~98	~89
$g_{33} - g_{13}(m^4/C^2)$	0.0745	0.0755	0.0778

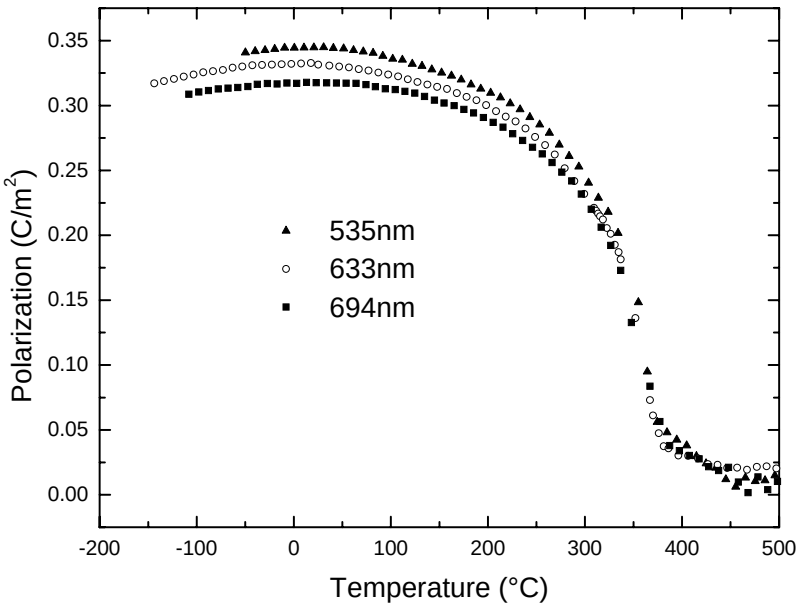

Figure 3.13 Calculated polarization of PBN57 as a function of temperature at λ=535, 633, and 694nm

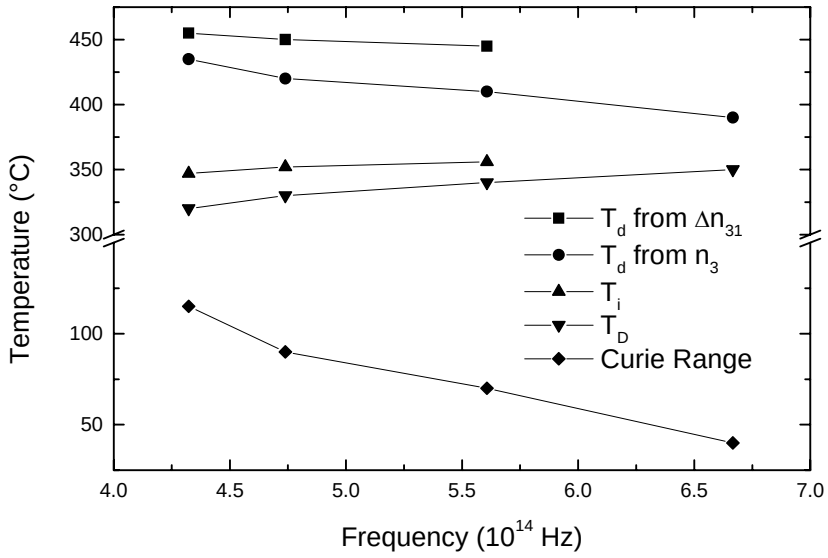

Figure 3.14 Summary of T_i, T_d, T_D, and Curie range of PBN57 as a function of frequency

3.3.2.3 Correction of Polarization:

Presently there are no available reference for the frequency and temperature dependent values of quadratic electro-optical coefficients of PBN. From equation (3.11) and (3.19), the quadratic electro-optical coefficient g_{33} has been calculated from around -150 °C to 350 °C and plotted in Figure 3.15, which shows a considerable dependence upon temperature but small dependence on frequency. The data of dispersion of electro-optic effect for ferroelectric is sparse to the author. Arabidze and Chikvaidze [Arabidze and Chikvaidze, 1979] measured the temperature dependence quadratic electro-optic coefficient of barium titanate at three wavelengths 460nm, 500nm, and 600nm. Their results showed that the quadratic electro-optic coefficient was very dependent on the temperature and frequency.

The phase transition has not been considered in this calculation since g_{33} maybe experience an abruptly change during the phase transition. So the calculated values of g_{33} near and above T_m is not reliable. However, this would not effect results the calculation of polarization. In equation (3.10) $\delta(\Delta n_{31})$ is near zero above T_m, ensuring the values of P_d near zero no matter the values of g_{33}.

The polarization estimated using corrected electro-optical coefficients is plotted in Figure 3.16. The decreasing tendency of polarization obtained without correction for 535 nm and 694nm is no longer present. In the low temperature range for the 633nm, a

slightly decreasing tendency still exists but occurs at a lower temperature around -100 °C, shifting about 60°C to lower temperature. The above correction is qualitative, a quantitative correction maybe available after more rigorous model for optical refractive index and g value.

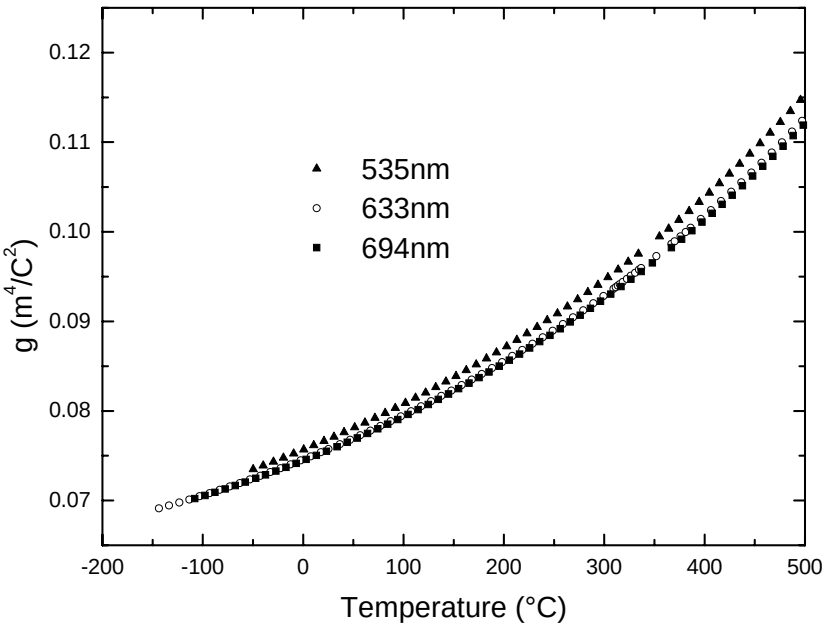

Figure 3.15 g_{33} of PBN dispersion with temperature

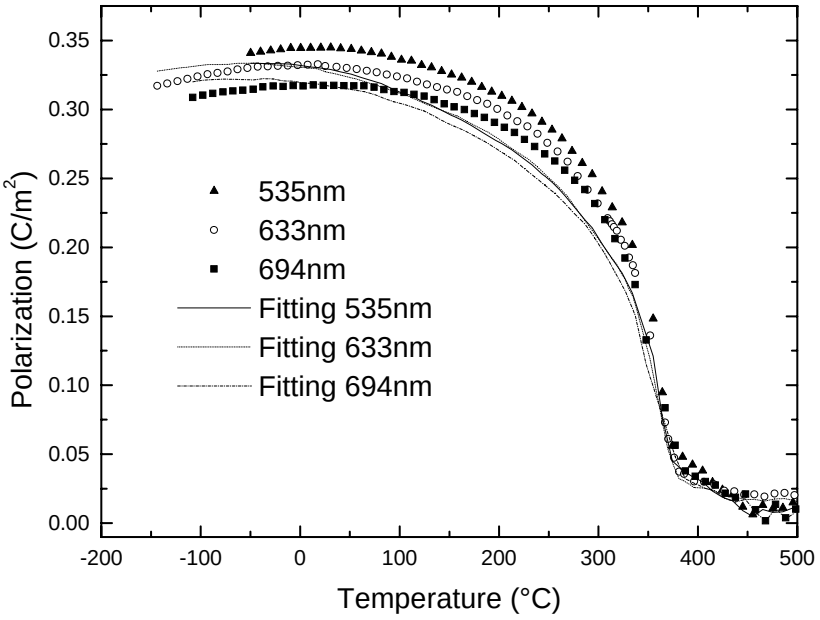

Figure 3.16 Corrected polarizations of PBN

3.3.2.4 Dielectric constant measurement

In order to evaluate fully the results of optical measurement the dielectric capacitance and loss tangent of the PBN57 crystal was measured using HP4284 LCR meter from 1KHz to 1M Hz in the temperature range of -260-20°C at rate of 1°C /min and in the temperature range of 30-460°C at rate of 4°C /min. In figure 3.17 both in the heating and cooling runs, it's evident that the dielectric constant is not strongly frequency dependent. For PBN57 having high temperature phase transition (T_c>360°C), there is a small thermal hysteresis (at ~365°C in the heating and at ~355°C in the cooling run) However, the isotropic temperature derived from birefringence is lower than the T_m. This is a signature of the relaxor behavior in PBN solid solution. The low temperature dielectric constant with temperature is shown in Figure 3.18. There is no evident phase transition occurring. This supports the previous polarization correction with the consideration of the temperature and frequency dependent g_{33}.

Martirena [Martirena and Burfoot, 1974] and Uchino [Uchino and Nomura, 1982] suggested the variable power law, which is rewritten as:

$$\frac{1}{\varepsilon} = \frac{1}{\varepsilon_m} + \frac{(T - T_m)^{\alpha}}{C} \tag{3.20}$$

where ε and ε_m are the permittivity and its maximum, respectively, T_m is the temperature of ε_m and C and α are fitting parameters. It describes the paraelectric side

dielectric permittivity of ferroelectrics with diffuse phase transition. Power factor α close to 1 suggests normal ferroelectrics, while close to 2 suggests "complete" relaxor ferroelectrics. The fitting parameters are listed in table 3.3. The power factor of 1.43 suggests PBN57 is not a complete relaxor ferroelectrics.

The freezing temperature T_f can be derived from the Vogel and Fulcher relation [Viehland et. al. 1990b]:

$$f = f_0 \exp[-\frac{E_a}{k(T_m - T_f)}] \tag{3.21}$$

where T_f is the static freezing temperature, E_a the activation energy, f_0 the Debye frequency, k is Boltzmann's constant. The data listed in table 3.3 is not enough to yield a reasonable freezing temperature since there are only 4 sets data, however, 3 parameters need to be determined.

Table 3.3 Dielectric fitting results for PBN57

Frequency(KHz)	T_m(°C)	α
1	361.973	1.43
10	361.989	
100	362.018	
1000	362.58	

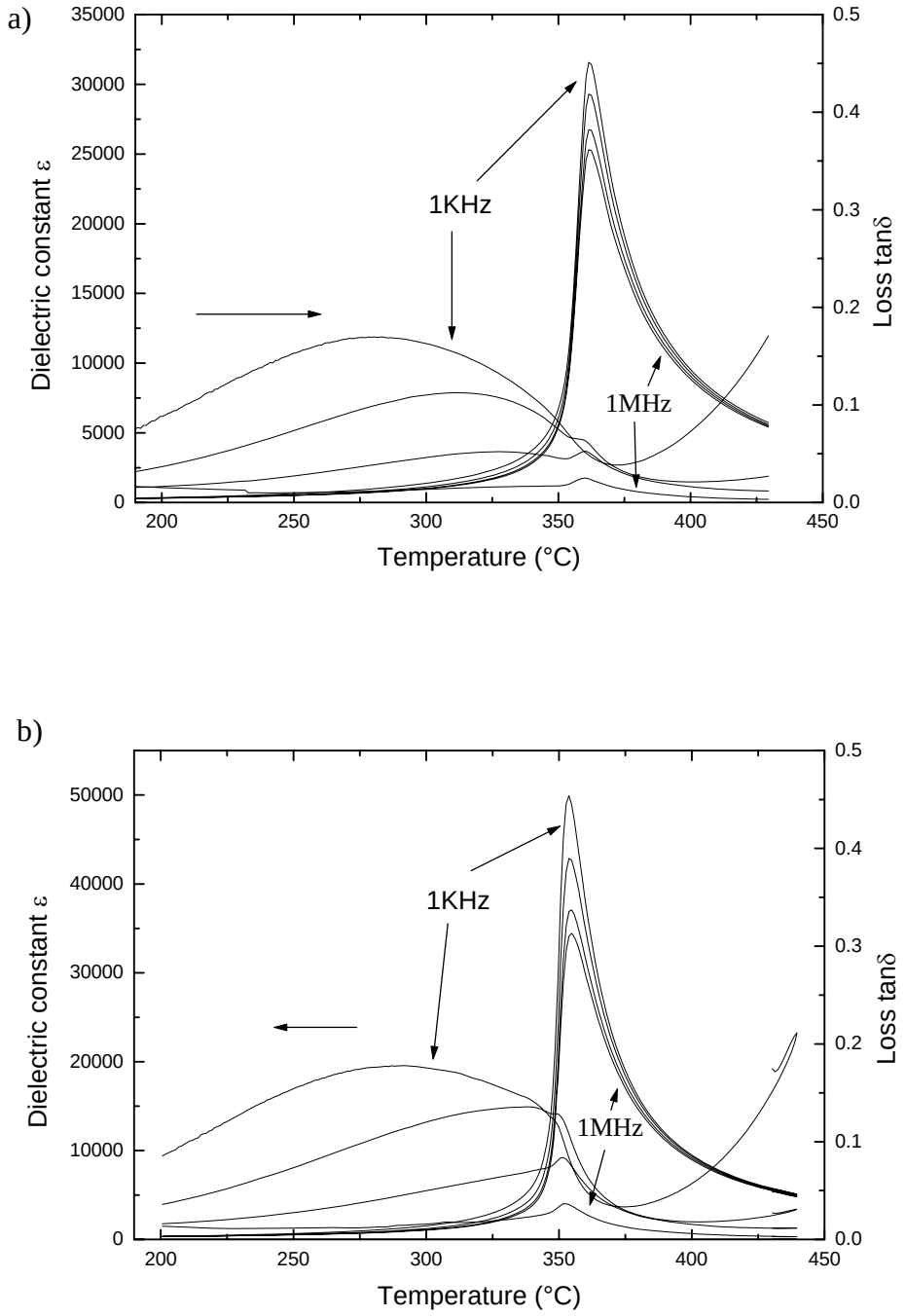

Figure 3.17 Dielectric constant and loss tangent of PBN57. a) heating run, b)cooling run.

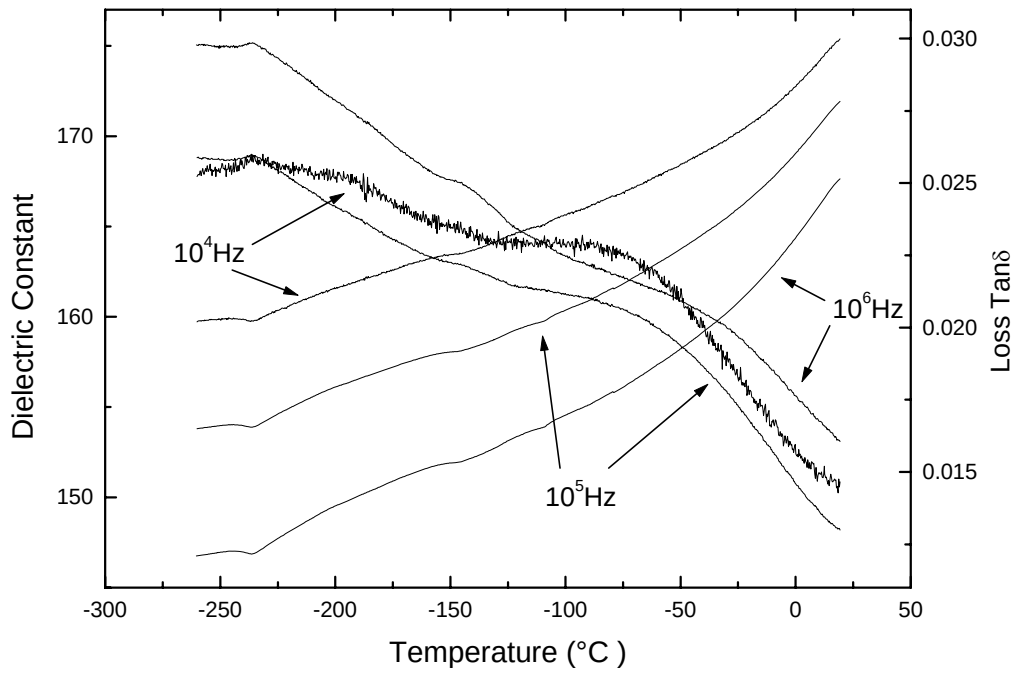

Figure 3.18 Dielectric constant and loss tangent of PBN57 at low temperature

3.4 Optical properties of PZN-PT

3.4.1 PZN-PT system and background

Lead zinc niobate $Pb(Zn_{1/3}Nb_{2/3})O_3$ (PZN) is a typical relaxor ferroelectric material which has globally disordered complex perovskite structure in which the Zn^{2+} and Nb^{5+} cations exhibit only short order on the B-site [Kuwata et al 1982]. The Curie region for PZN is around 140°C. PZN has a *m3m* prototype cubic point symmetry, and has *3m* rhombohedral point symmetry below phase transition. $PbTiO_3$ (PT) is a normal ferroelectric below phase transition temperature 490°C with 4mm tetragonal symmetry.

In 1980 PZN-PT single crystal was succeeded in growth [Kuwata et al 1982] and found that for compositions near MPB (figure 3.19) poling along <001> axis exhibited anomalously large piezoelectric coefficient and electromechanical coupling factor d_{33}=2500 pC/N, k_{33}=0.92, strain levels up to 0.6% with low hysteresis. These properties are highly attractive in the application of high performance piezo devices including ultrasound medical image probes, sonars for underwater communications, high power density and high sensitivity sensors and actuators [Yamashita 1994]. Although most recent research on PZN-PT has focused on its unusually large piezoelectric response, it has been reported that this material also exhibit extremely large electro-optic coefficient near the morphotropic phase boundary, with r_{33}=450pm/V (632.8nm) for <001> poled PZN-0.08PT, 97pm/V for <111> poled PZN-0.08PT, 78pm/V for <111> poled PZN-0.045PT, and 134pm/V for <001> poled PZN-0.12PT [Lu, et. al., 2000, 2001, Barad, et. al., 2000] This large electo-optic response makes the material an excellent candidate for highly efficient optical modulator.

As shown in phase diagram (Figure 3.19), the MPB of (1-x)$Pb(Zn_{1/3}Nb_{2/3})O_3$-x$PbTiO_3$ was initially believed to be an almost vertical boundary that separates the rhombohedral 3*m* from the tetragonal 4*mm* phase and located close to the value of x~10% for PZN-xPT. In addition to the known rhombohedral and tetragonal phases, a recent advance has been accomplished with the discovery of a new monoclinic phase in PZT [Noheda et al 1999]. New orthorhombic and monoclinic phases have also been found in PZN-PT [Noheda et al 2001]. These new phases play a key role in explaining the high piezoelectric and electrostrictive responses near the MPB. In PZN-PT, the new phase has an point symmetry *mm*2 and extends in a narrow concentration range around the MPB ($8\%<x<11\%$) with almost vertical phase boundaries on either side. This new phase can be described as a "matching" phase between the rhombohedral and tetragonal phases. This means that the polarization vector, instead of being aligned with a particular crystal axis, may be pointing in an arbitrary direction within a plane, allowing for a very easy reorientation of the polarization vector. Recently, a model [Fu and Cohen 2000] has been proposed that connects the structural features of the lead relaxor systems with their unusual polarization properties.

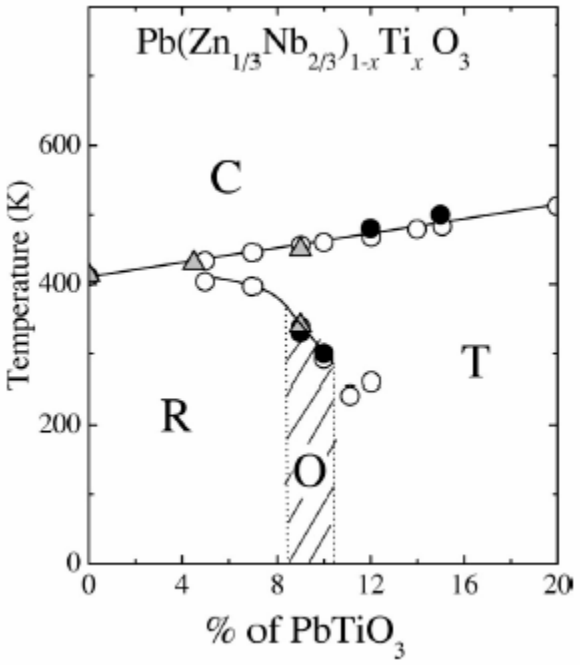

Figure 3.19 Phase diagram of PZN-PT around its MPB [La-Orauttapong 2002] C:cubic, T: tetragonal, O: orthorhombic, and R: rhombohedral

3.4.2 Experiment results of optical refractive index

The apex angle of prism sample was determined as 7°22′. The optical refractive indices n_3 of PZN-0.12PT single crystal were measured by minimum deviation method both before and after poling with wavelengths 450nm, 535nm, 633nm, and 694nm from room temperature to around 350°C as shown in Figure 3.20 and Figure 3.21. Both of the index data sets exhibit normal dispersion behavior. After poling the refractive indices n_3 decrease drastically by 0.17 for 694nm and 0.1 for 450nm. This is consistent with the dielectric constant measurement that after poling the dielectric constant decreases significantly from 4000 to 700[Zhang, unpublished data]. Lu [Lu 2000] measured refractive index of the PZN-0.12PT with n_3=2.46±0.01 and n_1=2.57±0.01 by Brewster's angle at 633nm. The refractive index at 633nm at room temperature in this thesis measured by minimum deviation is about 0.065 larger than Lu's values. The reason that causes so much difference of measurements of the refractive index is unknown though with the different measurement method. Saori [Saori, 2003] measured PZN-0.09PT with n_3=2.62 and n_1=2.63 at 515nm at room temperature while the measurement method was not described. It is well known that for the complex solid solution with PT, the refractive index is increasing with the content of PT. Saori's result is consistent with this measurement.

The procedure applied for PBN57 to determine the optical Curie region is not used for PZN-0.12PT since the diffuseness coefficient α of PZN-0.12PT is around 1.2 [Zhang, unpublished data] and exhibit very weak relaxor behavior.

The temperature dependent effective oscillator energy E_0 and dispersion energy E_d obtained by equation 3.16 are plotted in Figure 3.22 and 3.23, respectively. After poling, both the effective oscillator energy E_0 and dispersion energy E_d increased. More quantitatively the ratios of effective oscillator energy E_0 and dispersion energy E_d after poling to before poling are plotted in Figure 3.24. It is interesting to note that the ratio of E_0 and E_d have the same trend in the whole temperature. The ratio of E_0 is around 1.32 while the ratio of E_d is around 1.6.

The effective dispersion oscillator energy, E_0, is an energy which corresponds roughly to about one and half times the measure optical bandgap from transmission and represents the average energy of all the optical transmissions located at the averaged wavelength position, λ_0 with $E_0 = hc/\lambda_0$, where *h* is Planks constant.

The dispersion energy E_d, is a measure of the average strength of interband optical transitions. The benefit of this empirical parameter is based upon the following observations [Wemple, 1971, 1972, 1973]:

(1) E_d is very nearly independent of E_0 and consequently provides an independent oscillator strength quantity which is not related to any specific spectroscopic model or related energy bandgap parameter. The dispersion energy is not intimately related to the internuclear distance as the case in other description of the electronic dielectrics constant.

(2) The dispersion energy has been shown to obey a simple empirical relationship [Wemple, 1972] in variety of ionic and covalent solids:

$$E_d = \beta N_c Z_a N_e (eV), \tag{3.22}$$

where N_c is the coordination number of the cation nearest neighbor to the anion (e.g. N_c=6 in NaCl and N_c=4 in Si), Z_a is the formal chemical valency of the anion (e.g. Z_a=1 in NaCl and Z_a=2 in MgO), and N_e is the total number of valence electrons per anion (e.g. N_e=8 in NaCl). The coefficient β almost without exception takes on either of two values: $\beta = 0.37 \pm 0.04eV$ in covalent materials and $\beta = 0.26 \pm 0.03eV$ in ionic materials [Wemple, 1971].

In the next section the polarization of the crystal after poling was increased by 30%. Thus it is reasonable to conclude that the effective dispersion oscillator energy is proportional to the polarization while the dispersion energy is proportional to the quadratic polarization, i.e.:

$$E_0 \propto P_s \tag{3.23a}$$

$$E_d \propto P_s^2 . \tag{3.23b}$$

There is still remaining the controversial although the above relation can easily understand the increasing of E_0 and E_d after poling quantitatively. First, the increasing of E_0 and E_d occurs over the whole temperature range including in the paraelectric state with non polarization. Second, the effective dispersion oscillator energy E_0 is linear to optical bandgap [Wemple, 1971,1973], which is proportional to quadratic polarization known from equation 1.5.1.

The slopes of the high temperature linear behavior for each frequency are listed in table 3.4. The slope is increasing with frequency for both before poling and after poling. However, there is no clear trend of the slope change after poling.

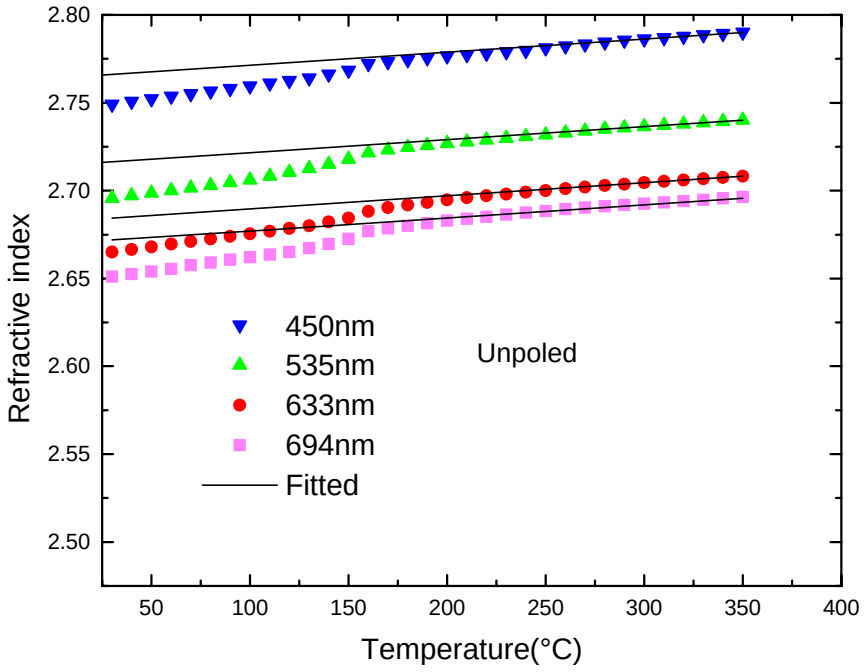

Figure 3.20 Optical refractive index n_3 of PZN-0.12PT single crystal before poling as a function of temperature at λ=450, 535, 633, and 694nm

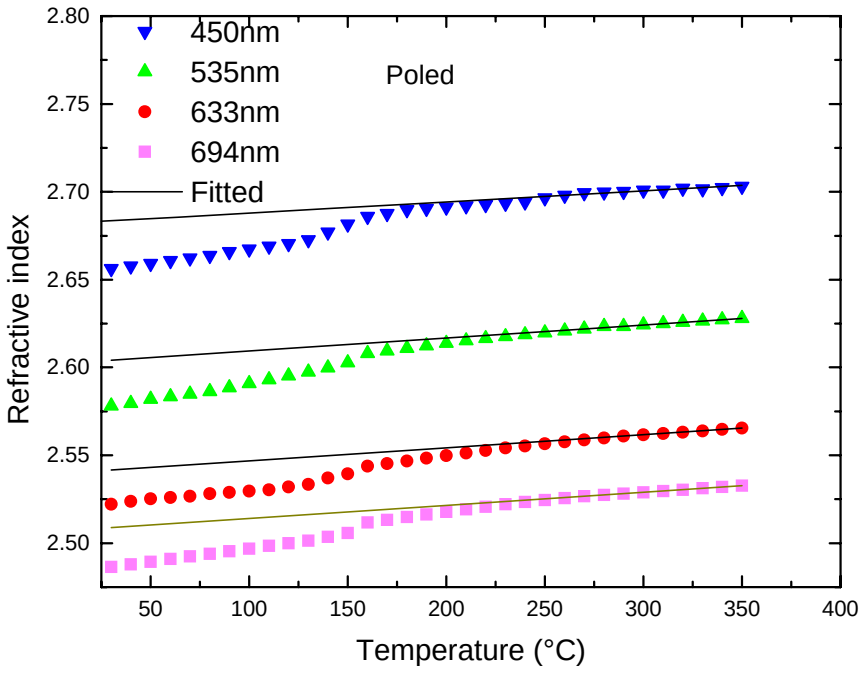

Figure 3.21 Optical refractive index n_3 of PZN-0.12PT single crystal after poling as a function of temperature at λ=450, 535, 633, and 694nm

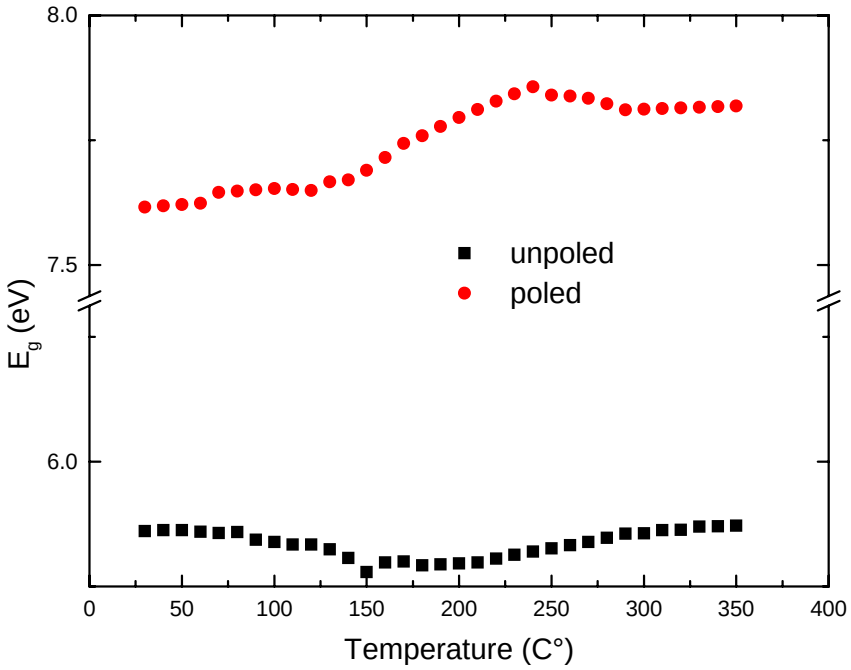

Figure 3.22 Temperature dependent effective dispersion oscillator energy E_0

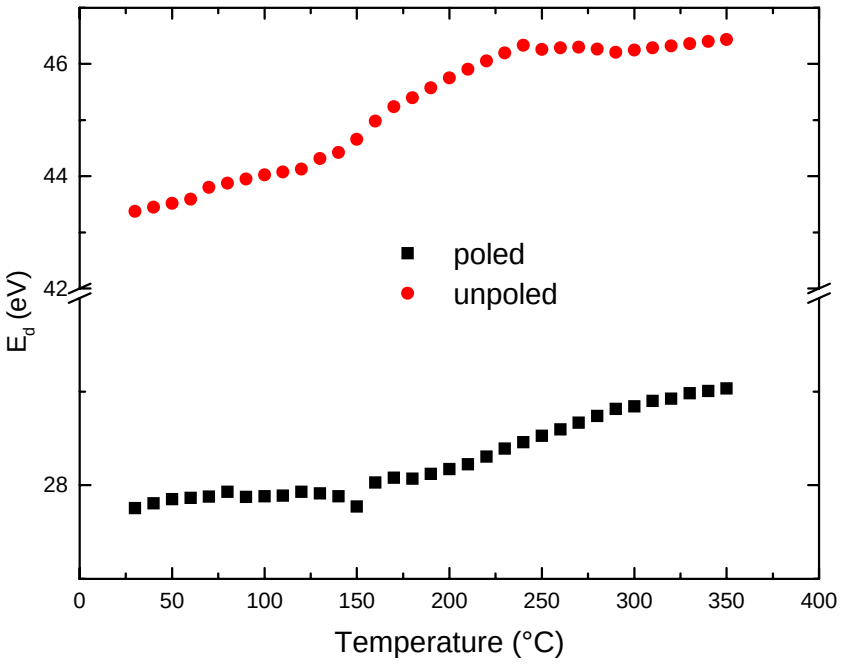

Figure 3.23 Temperature dependent dispersion energy E_d

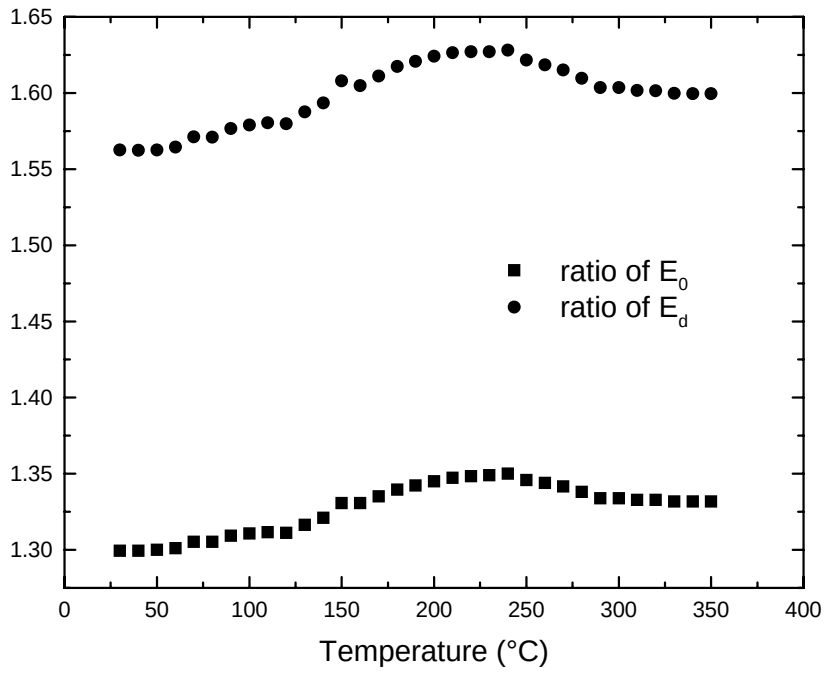

Figure 3.24 The ratio of effective dispersion oscillator energy E_0 and dispersion energy E_d ($E_{poled}/E_{unpoled}$)

Table 3.4 Slope of high temperature linear refractive index of PZT-0.12PT

Wavelength	694nm	633nm	533nm	450nm
Unpoled (10^{-5}/°C)	7.42	7.43	7.431	7.432
Poled (10^{-5}/°C)	7.2	7.428	7.44	7.446

3.4.3 Birefringence of PZN-0.12PT

Birefringence PZN-0.12PT was measured at wavelength of 694nm, 633nm, and 535nm as shown in Figure 3.25. The higher the frequency of the light, the larger the birefringence. All three birefringence remained negative in the measurement temperature range. In the temperature above 200°C, due to the small view field of the lens and limitation of equation 3.15, the birefringence is not reliable when the value is less than 0.005. Since during this temperature range the number of fringes (less than 1 within the filed of view) was almost still, birefringence was estimated as constants. The accurate measurement of birefringence for this temperature range will be introduced in chapter 6.

3.4.4 Polarization of PZN-0.12PT

The polarizations of PZN-0.12PT were calculated from both data set of refractive index and birefringence. From the result of refractive index the polarization after poling is about 0.4C/m^2, which is in agreement with the result of [Lu 2000] and [Kuwata 1982]. Also the polarization is improved 30% after poling. The polarization derived from the birefringence is slightly larger than the one from refractive index. As mentioned in the last section the measured birefringence above 200 °C was approximated as constant; although in fact there is a small positive trend of the birefringence with temperature. Thus the value of $\delta(\Delta n_{31})$ in equation 3.10 for calculation was larger than the real one, and this caused slightly upper bound estimation on polarization. Here $g_{11} - g_{12} = 0.013 m^4 / C^2$ [Kuwata 1982].

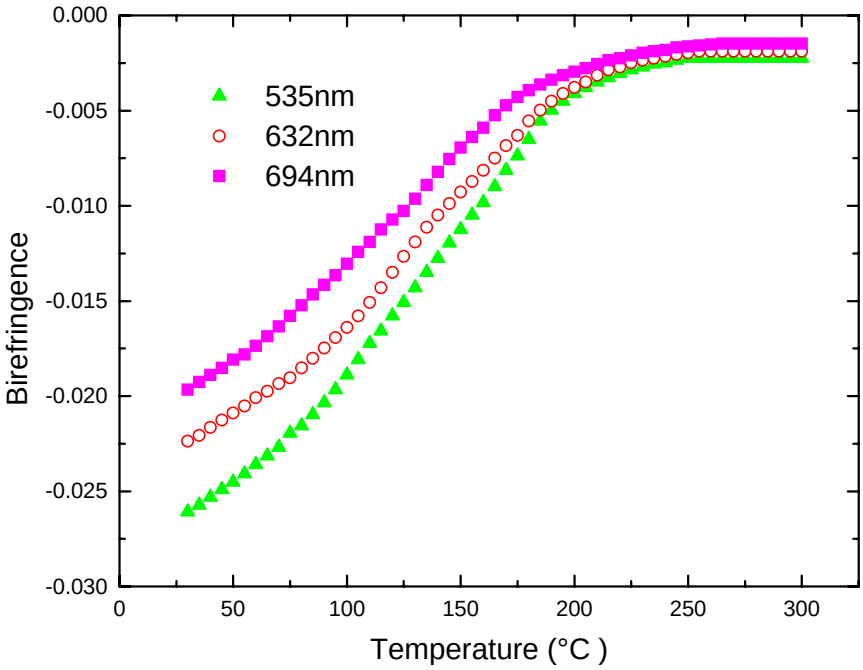

Figure 3.25 Birefringence of PZN-0.12PT as a function of temperature at λ=535, 633, and 694nm

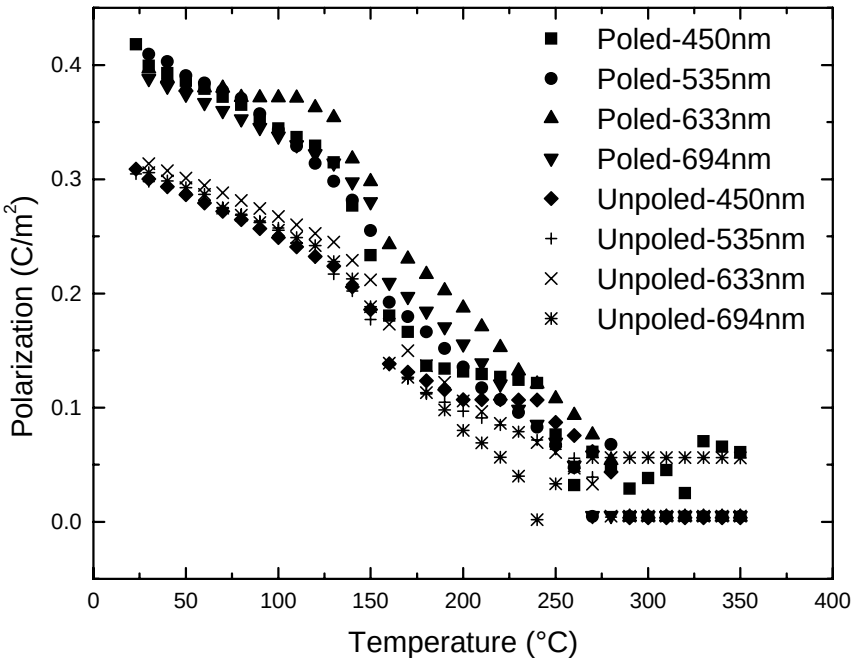

Figure 3.26 Polarization of PZN-0.12PT derived from refractive index as a function of temperature for both poled and unpoled sample

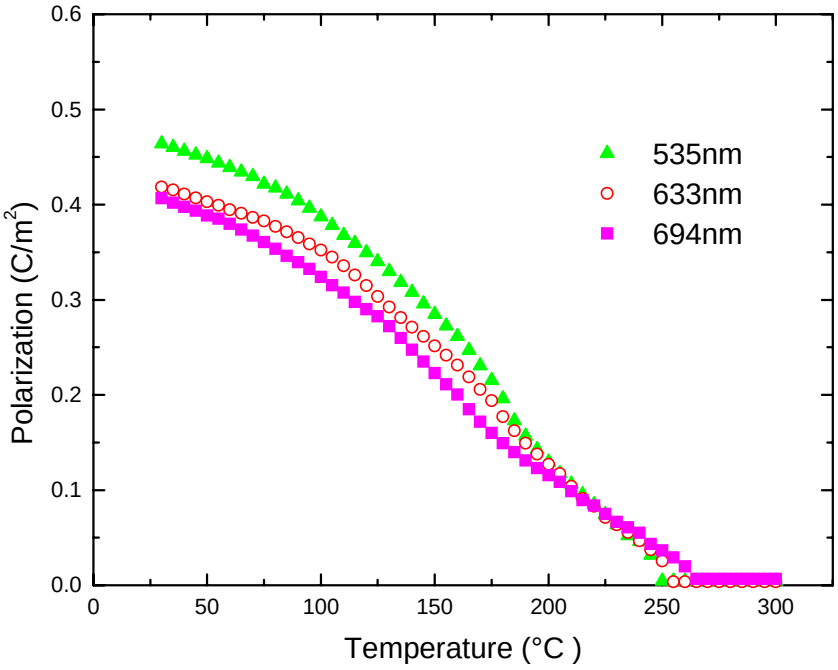

Figure 3.27 Polarization of PZN-0.12PT derived from birefringence as a function of temperature at λ=535, 633, and 694nm

Chapter 4

Thermo-optical properties

4.1 Introduction

The temperature dependence of the refractive index dn/dT of ferroelectrics is of practical importance in many optical and optoelectronic applications such as in focusing, guiding, coupling, modulation of radiation, optical fiber communication system, and high-resolution photographic lenses, which are required to operate under a wide range of temperature conditions [Tsay 1973]. When the crystal is used in laser applications, it will absorb part of the Laser power and be heated, and in turn the refractive index is changed. By changing the ambient temperature the refractive index also can be varied. In some other applications, both the absolute magnitude of dn/dT , as well as its frequency dependence are of interest, such as nonlinear crystal in the high-power nonlinear optical device [Ghosh 1994, 1995].

Usually there are two aspects ascribing to dn/dT coefficient for common dielectric. One comes from thermal expansion; when temperature increases, the material expands, becoming less dense. This mechanism would tend to make dn/dT negative. Another is the dependence of dipole moment on ionic displacements or the so-called electron-phonon interaction. In addition, however, the polarization contribution must be considered in ferroelectrics thus the expression below contains three terms:

$$\frac{dn}{dT} = \frac{dn}{dT}(\alpha) + \frac{dn}{dT}(E_g) + \frac{dn}{dT}(P) \qquad (4.1)$$

The first contribution can be expressed by using thermal expansion coefficient. As to the second contribution, no uniform formula is available until now. Most literatures [Zysset

1992; Tsay 1973, 1977] attribute this contribution to the temperature change of bandgaps. But Zhu et al.[Zhu 1987] pointed out that this was obscure. The optical refractive index is related to the difference between the average energies of the conduction and valence bands, rather than the bandgaps. Surely the bandgaps usually decrease with an increasing temperature, but in the meantime bandwidths increase. Therefore, it is not straightforward to decide whether the difference increases or decreases with the increasing temperature. The last term corresponds to electrooptic effect due to the temperature dependent spontaneous polarization, P_s.

4.2 Experiment results

From the measured optical refractive index and birefringence presented in chapter 3, the thermo-optical coefficients for a given frequency are determined and approximated by the differential:

$$\frac{dn}{dT} = \frac{n(T_2) - n(T_1)}{T_2 - T_1} \tag{4.2}$$

4.2.1 Thermo optical properties of PBN

The thermo-optic coefficients of n_3 and (n_3 -n_1) for PBN obtained from the refractive index n_3 and birefringence are shown in Figure 4.1 and Figure 4.2 respectively. The thermo-optic coefficients of n_3 show strong temperature and frequency dependence below T_d but weak frequency dispersion at temperature above T_d as shown in Figure 4.1.

The calculated thermo-optic coefficients of the birefringence (in Figure 4.2) also show strong temperature dependence but weak frequency dispersion compared to that of refractive index n_3. By comparing the thermo-optic coefficient of n_3 and birefringence of 535nm at discrete temperature (values summarized in Table 4.1), the thermo-optic coefficient of n_1 is derived. As can be seen the thermo-optic coefficients of n_1 are much

less than those of n_3 at low temperature range. It has been observed that n_1 is much less dependent on temperature compared to n_3 for tetragonal ferroelectrics PBN [Guo t al., 1990] and SBN [Bhalla et al., 1987, 1992] with tungsten bronze structure. This confirms that polarizability is highly anisotropic with primary contribution coming from the ionic longitudinal displacement parallel to c-axis. At the high temperature range the slope of the birefringence increases with frequency

The first electronic term in equation 4.1 is usually positive since E_g decreases with temperature and has an order of 10^{-5} for ionic crystal. The second lattice term is negative for thermal expansion and positive for thermal contraction because the electronic polarization density is proportional to the density of the material and has an order of 10^{-5} for ionic crystal [Tsay 1973]. The last polarization term can be the main contribution for ferroelectrics. In the high temperature paraelectric state, there is no significant change of n_3. This should be due to the compensation of positive electronic term and negative lattice term and both of them are around 10^{-5}. While in low temperature ferroelectric state, the lattice term is positive due to the contraction of x_3 which increases with temperature [Bhalla et al., 1987, 1992], thus in the ferroelectric state all three terms are positive. The polarization term can be of the order of 10^{-4} at ferroelectric phase, e.g. at 180°C. In the high temperature paraelectric state, the n_1 decreases with temperature. This is similar as that of SBN of tetragonal tungsten bronze structure. The lattice term of n_1 is negative during all the temperature range unlike the one of n_3. The negative thermo-optic coefficient of paraelectric state implies that the electronic term is not enough to compensate the lattice expansion effect. Comparing thermo-optic coefficients in low temperature ferroelectric state and in high temperature paraelectric state, one can

conclude that there is a positive contribution of polarization term in ferroelectric state with an order of 10^{-5}. Comparing the polarization term of n_3 and n_1 in ferroelectric state, the conclusion obtained again indicates that g_{33} is much lager than g_{13} from equations 3.8 and 3.9.

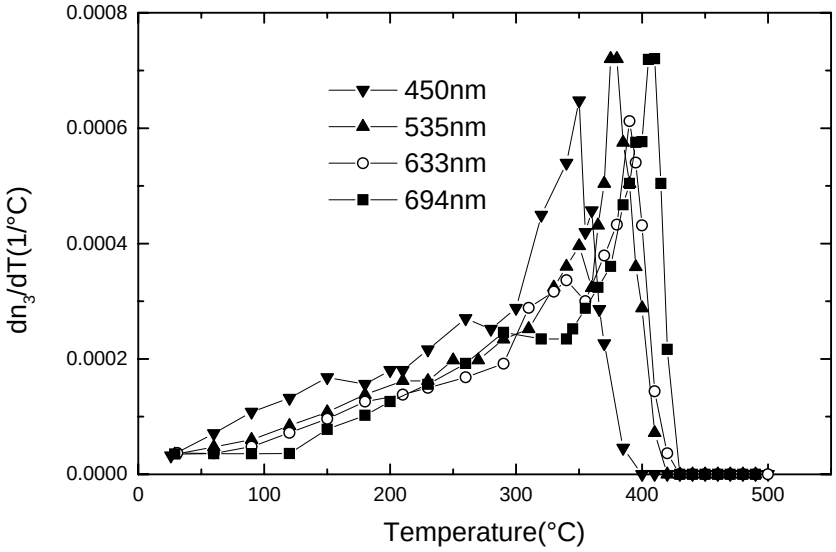

Figure 4.1 Thermo-optic coefficient of n_3 of PBN

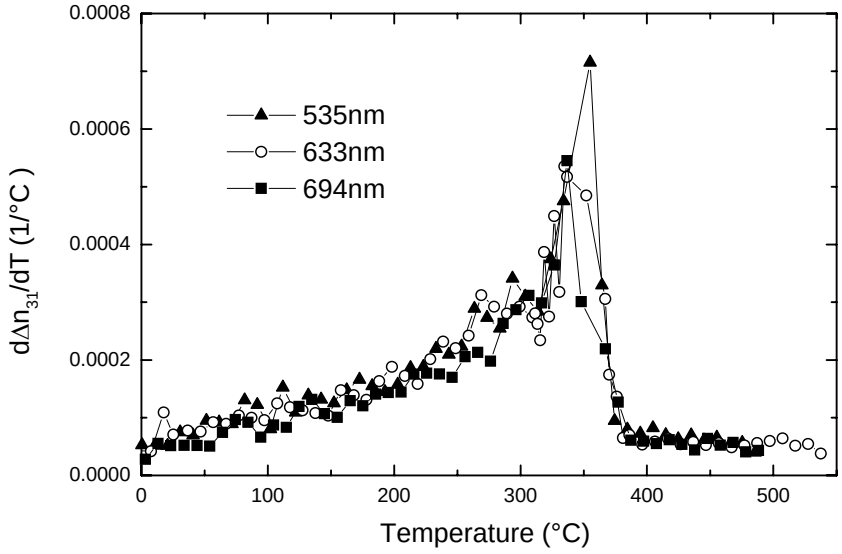

Figure 4.2 Thermo-optic coefficient of birefringence of PBN

Table 4.1 Thermo-optical coefficient of PBN at 535nm

Temperature (°C)	~60	~120	~180	~240	~300	~450-500
dn_3/dT (10^{-4}/°C)	0.6005	0.8402	1.3812	1.979	2.503	0
$d(n_3-n_1)/dT$ (10^{-4} /°C)	0.6978	1.0901	1.5492	2.094	3.098	0.56
dn_1/dT (10^{-4}/°C)	-0.0973	-0.2499	-0.168	-0.115	-0.595	-0.56

Table 4.2 Thermo-optical coefficient of birefringence of PBN at high temperature

Wavelength	$d(n_3-n_1)/dT$ (10^{-4})
535nm	0.56
633nm	0.529
694nm	0.485

4.2.2 Thermo optical properties of PZN-0.12PT

The thermo-optic coefficients of n_3 for PZN-0.12PT before and after poling are shown in Figure 4.3 and 4.4, respectively. The thermo-optic coefficients of (n_3 -n_1) are plotted in Figure 4. The thermo-optic coefficients of n_3 for PZN-0.12PT are similar to PBN also exhibiting temperature and frequency dependence below T_m (around 160°C) but weak frequency dispersion at temperature above T_m (see Table 3.4). It's evident that after poling the thermo-optic coefficients of n_3 in the low temperature range increased. As discussed before, this is also due to the polarization term in equation 4.1. After poling the polarization increased by 30% for PZN-0.12PT crystal and this increased polarization improved the thermo-optic coefficients consequently. Unlike PBN57 with negative thermo-optic coefficients of n_1 in ferroelectric state, the thermo-optic coefficients of n_1 of PZN-0.12PT are positive in ferroelectric state.

The thermo-optic behavior can be analysis in terms of temperature dependent single oscillator parameters, E_0 and E_d. In differential form equation 3.16 becomes [Wemple, 1977]:

$$\frac{dn}{dT} = -\frac{(n^2-1)^2}{2n}\left(\frac{\frac{dE_0}{dT}}{E_d}\right)\left((1-K)+\frac{(1+K)E^2}{E_0^2}\right) \tag{4.3a}$$

where, $K = \dfrac{\dfrac{d\ln E_d}{dT}}{\dfrac{d\ln E_0}{dT}}$ (4.3b)

The quantity K depends on the detailed shape of the imaginary part of the dielectric constant spectrum ε_2 and its temperature dependence. For a linear energy shift with temperature of this entire spectrum without distortion, it can be shown that

$0 \le K \le 1$ and the precise value dependence on details of the spectral shape. For $K > 1$, it is necessary that the ε_2 spectrum change shape as well as shift position with temperature. The value $K = 1$ forms a boundary between situations where the magnitude of dn/dT increases or decreases as the photon energy approaches the interband dege. The latter situation also allows for a change in sign of dn/dT as a function of optical wavelength. The decreasing of the bandgap parameter E_0 implies that the levels of transition to the valence band are reduced while the positive E_d suggests that the strength of those energy levels closest to the band edge are also changing to increased strength and broadening of the optical oscillator transition resonances. The large value of dE_0/dT has also been noted to be associated with a very small coefficient of thermal expansion in materials.

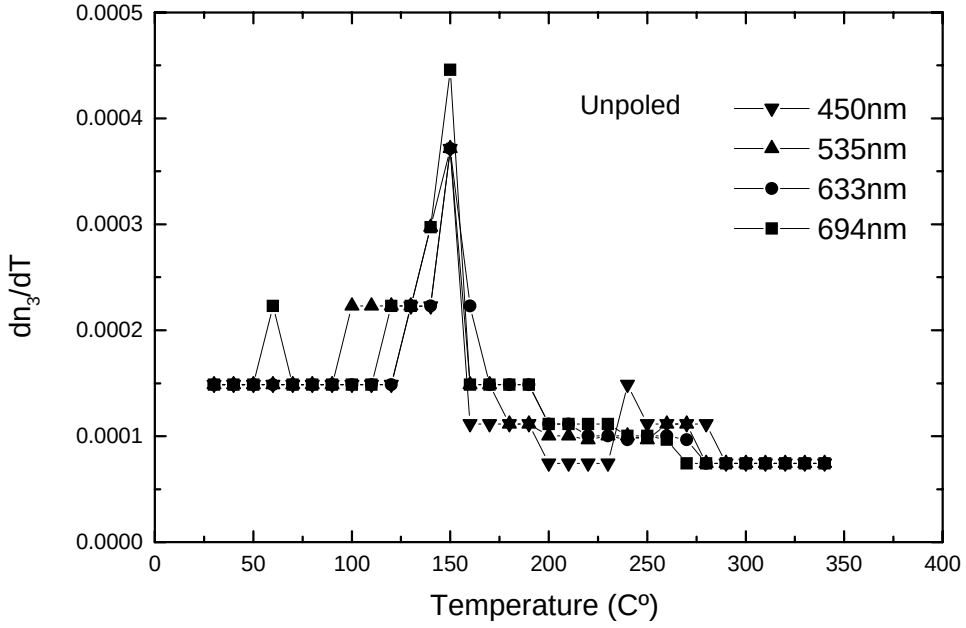

Figure 4.3Thermo-optic coefficient of n_3 of unpoled PZN-0.12PT sample

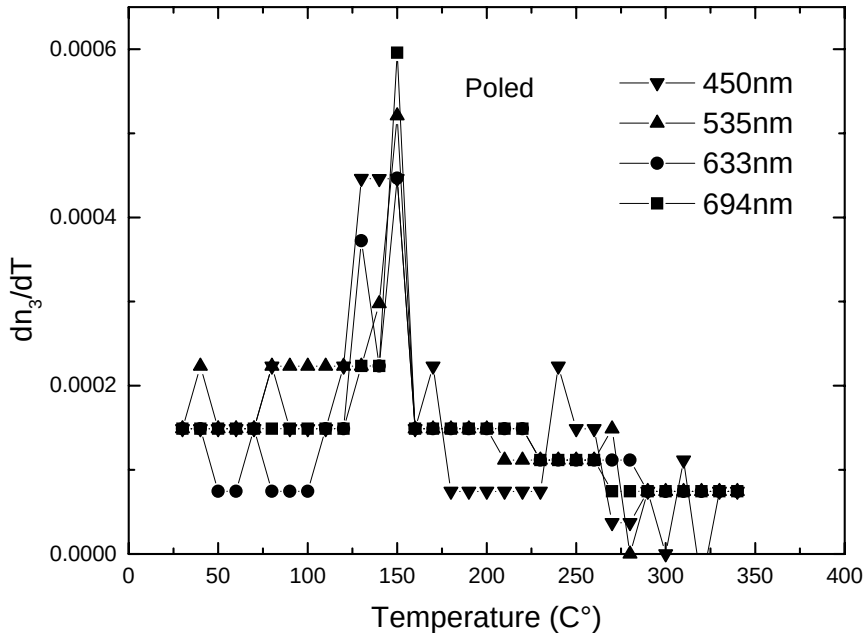

Figure 4.4Thermo-optic coefficient of n_3 of poled PZN-0.12PT sample

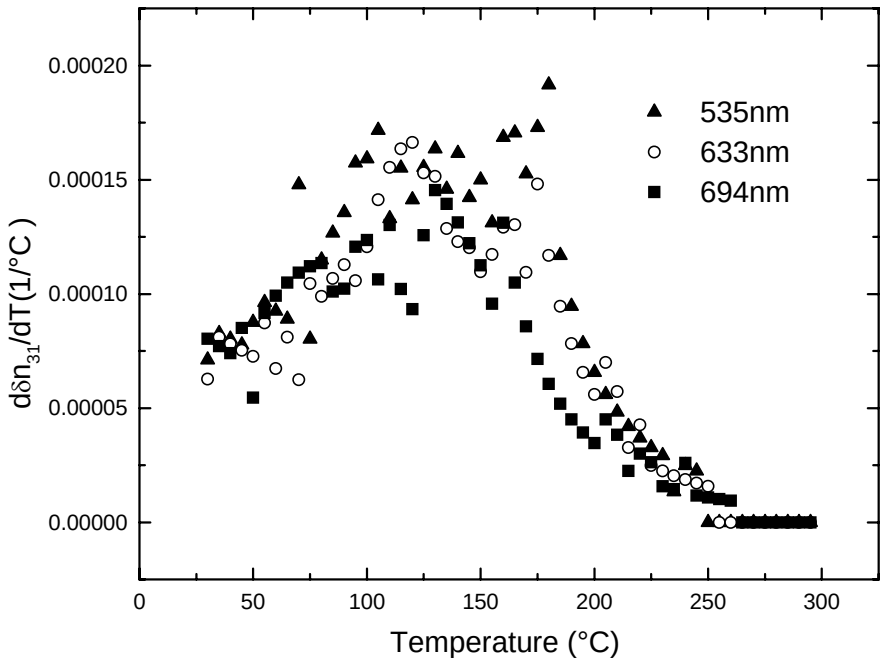

Figure 4.5 Thermo-optic coefficient of birefringence of poled PZN-0.12PT sample

Chapter 5

Transmission spectrum analysis

5.1 Introduction

The optical transmission spectrum study can reveal the information about the electronic band structure, fundamental optical bandgap, ionic lattice absorption, and material impurities of the sample. is of fundamental important. As a relaxor system PZN-PT, it is also interesting to examine how the poling causes the optical bandgap shift, the effects of electron-phonon interaction, as well as the optical anisotropic properties.

5.1.1 Transmission spectrum measurement system

The PC2000-UV-VIS Miniature Fiber Optic Spectrometer (Ocean Optics Inc.) was used to measure the transmission spectrum. The transmission spectrum was collected by the software OOIbase 32. In order to obtain a transmission spectrum, a dark spectrum (D), which is the spectrum after blocking the light source, reference spectrum (R), which is the spectrum without sample, and sample spectrum (S) are measured. Then the transmission spectrum (T) is calculated by:

$$T(\lambda) = \frac{S(\lambda) - D(\lambda)}{R(\lambda) - D(\lambda)} \times 100\% \qquad (5.1)$$

5.1.2 Fourier transform Infrared spectroscopy

The Nicolet-6700FT-IR spectrometer (Thermo Electron Corp.) was used to measure the FTIR spectrum. Fourier Transform Infrared spectroscopy (FTIR) is a measurement technique for collecting infrared spectra. Instead of recording the amount of energy absorbed when the frequency of the infra-red light is varied (monochromator), the IR light is guided through an interferometer. After passing the sample the measured

signal is in form of its interferogram. Performing a mathematical Fourier Transform on this signal results in a spectrum identical to that from conventional (dispersive) infrared spectroscopy.

FTIR spectrometers are cheaper than conventional spectrometers because building of interferometers is easier than the fabrication of a monochromator. In addition, measurement of single spectra is faster for the FTIR technique because the information of all frequencies is collected simultaneously. This allows multiple samples to be collected and averaged together resulting in an improvement in sensitivity. Because of its various advantages, virtually all modern infrared spectrometers are of the FTIR variety.

5.2 Experiment and results

Optical quality PZN-0.12PT single crystal with dimension $4.2 \times 2.65 \times 0.32$ mm was studied both before and after poling. The same poling procedure as applied to the sample used for index measurement was applied to this sample. Spectra were measured both prior and after poling along a axis and c axis with a polarizer at room temperature.

5.2.1 Results of transmission spectrum

5.2.1.1 Transmission spectrum

The measured transmission spectra from 350nm to 1000nm were shown in Figure 5.1. Before poling, transmissions of both spectra along a-axis and along c-axis are around 30%. While after poling, transmissions are improved dramatically to around 60%. On the surface and domain walls of the crystal sample, the optical refractive index is discontinuous to result in reflection loss and less transmission. The unpoled sample has much more domains (walls) and nanoregions with different orientation with respect to the

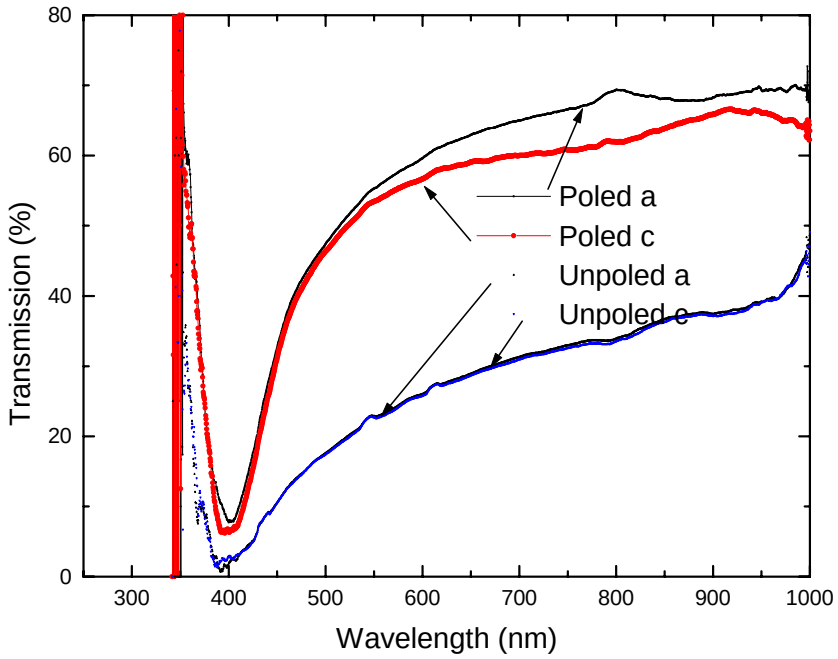

Figure 5.1 Transmission spectra of PZN-0.12PT between 350-1000nm.

optical axis comparing with the poled sample. Thus when the light passes through the unpoled crystal, those domain walls cause large reflection loss or scattering loss. For PZN-0.12PT single crystal, after poling along the <001> direction, the single domain area enlarges and the loss due to domain walls reduced significantly. There is a very slight difference of the transmission along a axis and c axis of the unpoled sample indicating that the unpoled sample is almost isotropic. This is in agreement with the fact that the pseudo-cubic structure of unpoled PZN-0.12PT. While the evident difference of transmission along a axis and c axis for the poled sample is also verifying the anisotropic structure of poled sample.

5.2.1.2 Absorption coefficient

In chapter 1 equation 1.5.17 gives the general case when light passes through a sample. While for a sample of parallel plate form this equation is necessary to be corrected after considering the reflection and multi-reflection in the sample as shown in Figure 5.2. The reflection of the surface between the sample and air is $R = \left(\frac{n-1}{n+1}\right)^2$, n the refractive index of the sample. Light with intensity I_0 indent on the sample, the first order transmission light intensity is $(1-R)^2 I_0 e^{-\alpha d}$, the second order is $R^2(1-R)^2 I_0 e^{-3\alpha d}$, and so on. So the total transmission light intensity is summed as:

$$I = I_0(1-R)^2 e^{-\alpha d}(1 + R^2 e^{-2\alpha d} + R^4 e^{-4\alpha d} + \cdots) = \frac{I_0(1-R)^2 e^{-\alpha d}}{1 - R^2 e^{-2\alpha d}} \quad . (5.2)$$

The transmission is given by:

$$T = \frac{I}{I_0} = \frac{(1-R)^2 e^{-\alpha d}}{1 - R^2 e^{-2\alpha d}} \quad . (5.3)$$

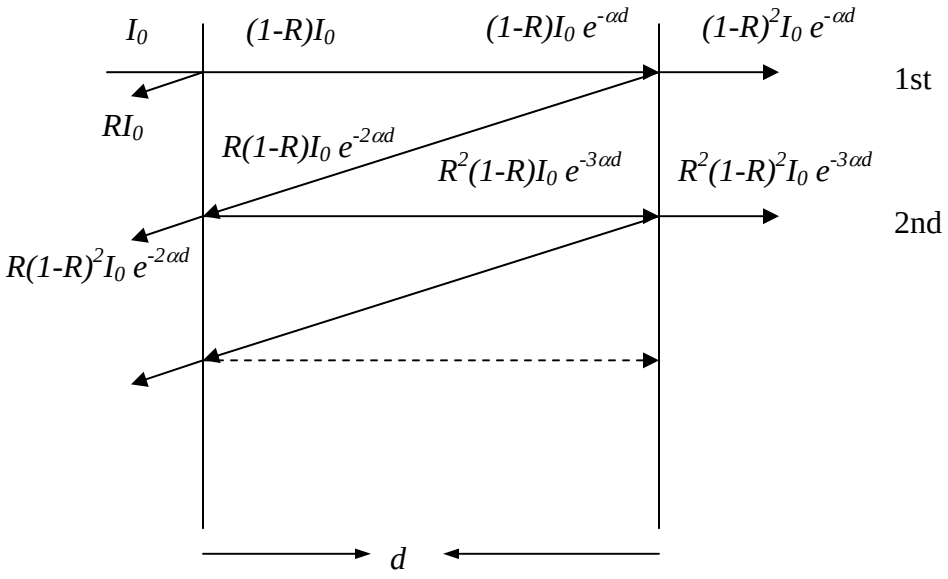

Figure 5.2 The transmission of light passing through sample with thickness of d

The reflection is very weak dependent on the frequency in the visible range though the refractive index is dependent on frequency. For both poled sample and unpoled sample, the difference of reflection of 450nm and 694nm are both less than 2 percent. This ensures that the error can be omitted if taking reflection *R* as a constant in equation 5.3. The absorption coefficients are calculated by equation 5.3 while *R* are both taken as values of 535nm for poled sample and unpoled sample as shown in Figure 5.3. The absorption coefficients α_c are larger than α_a for both poled sample and unpoled sample. This will be discussed late.

5.2.1.3 Optical energy gap

As introduced in section 1.5.5, for indirect allowed transition the $\sqrt{\alpha(\omega)\hbar\omega}$ vs. $\hbar\omega$ curve can consist of some straight lines and the adjacent two straight lines signify the absorption and emission of phonons in certain state phonons as shown in Figure 1.12. There is an obvious inflection point around 2.75 *eV* that separates the curve into two parts with different slope. A linear fitting was applied to the curve near this region to yield two straight lines with different slope as shown in Figure 5.4. The linear fitting data was limited in a narrow region around 0.15 *eV*. The reason that such narrow region is chosen rests on two considerations: firstly as introduced before that many state phonons are involved in the transition, thus the linear fitting cannot be applied to the whole curve otherwise only one state phonon will be yielded; secondly phonon energy are of the order of 10 *meV*, the region of 0.15 *eV* is enough to yield one state phonon.

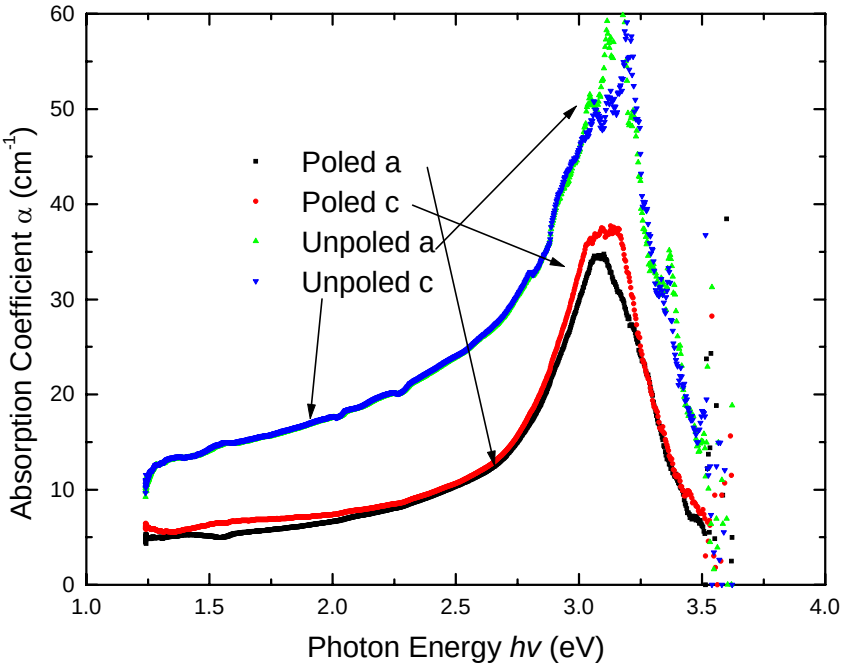

Figure 5.3 Absorption coefficient of PZN-0.12PT in visible range

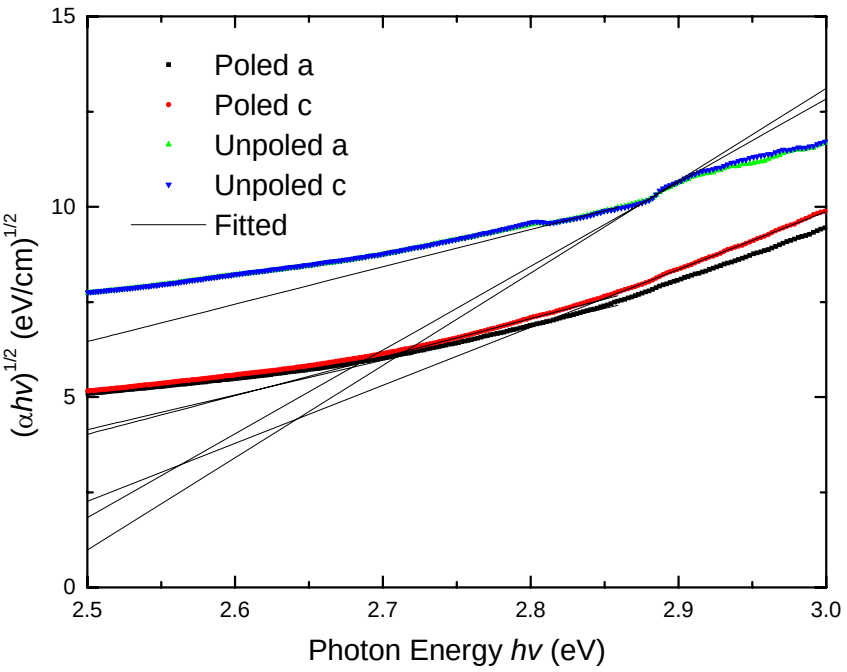

Figure 5.4 Allowed indirect transition accompanied by phonon in PZN-0.12PT

Table 5.1 Optical energy bandgap and phonon energy of PZN-0.12PT

		E_g-E_p (eV)	E_g+E_p (eV)	E_g (eV)	E_p (eV)
c	unpoled	1.84	2.46	2.15	0.30
	poled	2.10	2.35	2.23	0.12
a	unpoled	1.87	2.42	2.14	0.27
	poled	2.04	2.31	2.18	0.13

The values of optical energy gap E_g and phonon energy E_p are included in Table 5.1. Both optical energy along a axis and c axis are improved after poling while phonon energy reduced. The optical energy along c axis is much larger than that along a axis. This can be explained by the concepts introduced in section 1.5.1. After poling, the P_3 is increased and the energy along c axis is proportional to quadratic P_3 while the energy along a axis is just linear with P_3.

The calculated phonon energy, is almost ten times larger than the usually phonon energy, which is too high to be considered as lattice phonon. So the structure observed in Figure 5.4 is not due to the emission and absorption of phonon. PZN-0.12PT has a complex electronic system and the spin-orbit interaction can be strong and result in the splitting of the valence bands. The structure could be due to the transition between this splitting valence bands [El-fadl et al., 1998].

5.2.1.4 Urbach rule

The absorption coefficients near the band gap exponentially varying with light energy and temperature is know as Urbach rule [Dow 1972], which was first observed in many semiconductors and late proved to be a fundamental optical properties of the solid state, taking the form:

$$\alpha = \alpha_0 \exp\left(\sigma \frac{\hbar\omega - E_0}{kT}\right) \tag{5.4}$$

where E_0 is a parameter characterizing the energy gap, σ is a parameter characterizing the broadening of the absorption edge known as the steepness parameter and it is temperature dependent, α_0 is the pre-exponent constant and k is Boltzmann's constant. By fitting the $\ln\alpha$ and $\hbar\omega$ at different temperatures with a straight line as shown in Figure

5.5, all parameters can be derived. Unfortunately the present transmission spectrum is only measured at room temperature thus only steepness parameter σ can be calculated.

Skettrup [Skettrup 1978] explained the exponential behavior of the absorption edge in terms of thermal fluctuations in the band gap energy. As a consequence in this model the steepness parameter σ is related to the temperature dependence of the energy gap E_g in the form of:

$$\frac{dE_g}{dT} = -\frac{3k}{\sigma} \tag{5.5}.$$

where k is Boltzmann's constant. The temperature dependence of the energy gap using this relation was calculated and included in Table 5.2. There is no data in the literature available for the temperature dependent of the optical band gap of PZN-PT. The value of $-\frac{dE_g}{dT}$ for ferroelectric lithium potassium sulphate single crystal (LKS) is 3.68×10^{-2} for c axis and 5.16×10^{-2} for a axis [El-fadl et al., 1998]. These values are close, though these two ferroelectrics have very different structure. More investigation is necessary to verify this result.

The difference of absorption coefficients α_c and α_a for both poled sample and unpoled sample can also be interpreted by the Urbach rule. To compute the relative magnitudes of absorption coefficient for light polarization along the a and c axes it is convenient to separate the oscillator strength in longitudinal mass direction f^l and in transverse mass direction f^t [DiDomenico and Wemple 1968]. Since the absorption edge coefficient has the exponential form by Urbach rule, the absorption coefficient can be written as:

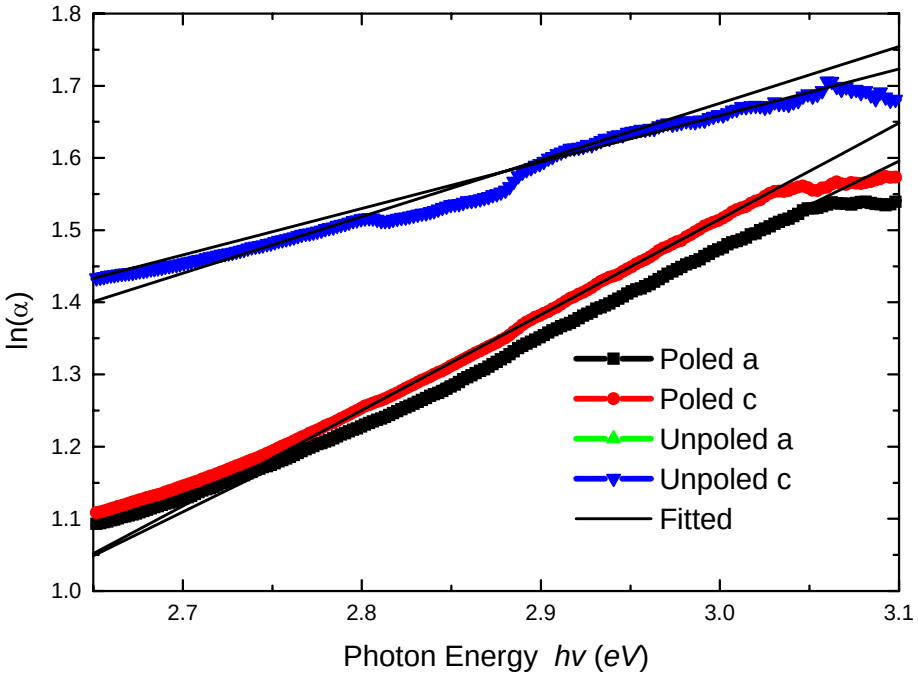

Figure 5.5 Transmission spectrum fitted by Urbach rule

Table 5.2 Parameters of PZN-0.12PT derived using Urbach rule

		$\sigma\,(10^{-2})$	$-\frac{dE_g}{dT}\,(10^{-3} eV/K)$
c	Unpoled	2.02	12.8
	Poled	3.43	7.58
a	Unpoled	1.96	13.2
	Poled	3.15	8.26

$$\alpha_l = \gamma f^{l} \exp[\beta(\hbar\omega - E)] \tag{5.6a}$$

$$\alpha_t = \gamma f^{t} \exp[\beta(\hbar\omega - E)] \tag{5.6b}$$

where γ is a constant of proportionality which includes the joint density of states, and $\beta = \sigma / kT$. Since longitudinal transition is much weaker than transverse, it is reasonable to take $\alpha_l = 0$. The light will not "see" the transition when its direction is parallel to the light polarization, thus when light polarization is parallel to the c axis only two perpendicular directions, both along the a axis, count while light polarization parallel to the a axis two perpendicular direction are along the c axis and another a axis for the tetragonal structure. The anisotropic coefficients are obtained as:

$$\alpha_c = 2\gamma f^{t} \exp[\beta(h\nu - E_a)] \tag{5.7a}$$

$$\alpha_a = \gamma f^{t} (\exp[\beta(h\nu - E_a)] + \exp[\beta(h\nu - E_c)]) \tag{5.7b}$$

where the oscillator strengths are assumed to be insensitive to the lattice polarization. The ratio of the absorption coefficient along two directions is:

$$\alpha_c / \alpha_a = \frac{2}{1 + \exp[\beta(E_a - E_c)]} \tag{5.8}.$$

For both poled and unpoled crystal, E_c is greater than E_a. So the value of equation 5.8 is larger than 1.

5.2.2 Results of FTIR

The measured FTIR spectrums from 6500 cm^{-1} (15.4 μm) to 40000 cm^{-1} (2.5μm) with resolution 2 cm^{-1} are show in Figure 5.6. The absorption is very strong when the wavelength is above 5μm. After poling the transmission was improved to 35% from 15% prior to poling. This is very similar as the transmission of the poled and unpoled sample

in the visible range. The reason is also due to the reflection and scattering loss resulting from domain walls.

There are two strong absorption peaks for wavelength below 5μm as shown in Figure 5.7. One absorption peak near 2.9 μm (3450cm^{-1}) corresponds to the well-known infrared absorption bands of O-H bond stretching mode. Hydrogen can easily enter the crystal during the growth step, forming OH^- radicals. The existence of hydroxyl ions (OH^-) has been reported in many ferroelectrics by IR absorption studies, such as $SrTiO_3$ [Brebner et al., 1981; Houde et al., 1987], $BatiO_3$ [Laulicht and Benguigui 1979; Kapphan and Weber 1981], $LiNbO_3$ [Herrington et al., 1973], SBN [Hunsche et al., 1995], and PBN [Lee et al., 1996]. Protons (H^+) play an essential role in thermal fixing of stored hologram in $LiNbO_3$ and PBN [Liu et al., 1997]. This indicates that it is possible to use PZN-0.12PT for hologram application. Another absorption peak is around 3.4μm (2950cm^{-1}). This corresponds to 365 *meV*, much large than any lattice phonon. This could be due to a stretching mode of O-H bond but at a different site.

5.3 Summary

The transmission spectrum of PZN-0.12PT was measured in wavelength from near UV 350nm to IR 15.4μm for both poled and unpoled samples with different polarization directions. Transmission was improved significantly after poling due to the supression scattering and reflection loss caused by domain walls. Optical band gap was enlarged due to the increased polarization in the poled sample. The temperature dependent optical band gap was determined by Urbach rule. The existence of Hydrogen

in PZN-0.12PT single crystal grown by flux method was hypothesized base on the absorption spectrum obtained by FTIR.

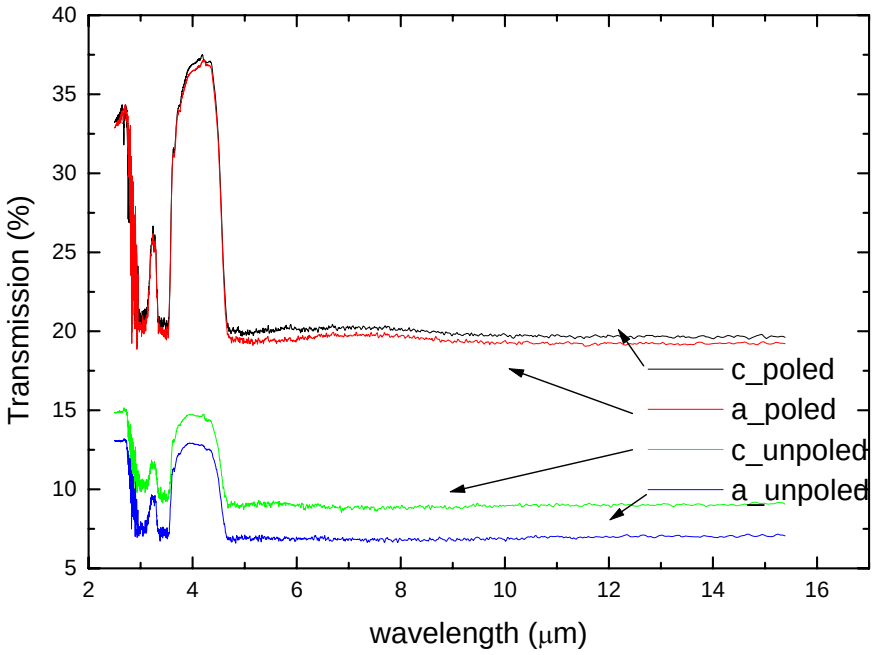

Figure 5.6 FTIR spectrum of PZN-0.12PT

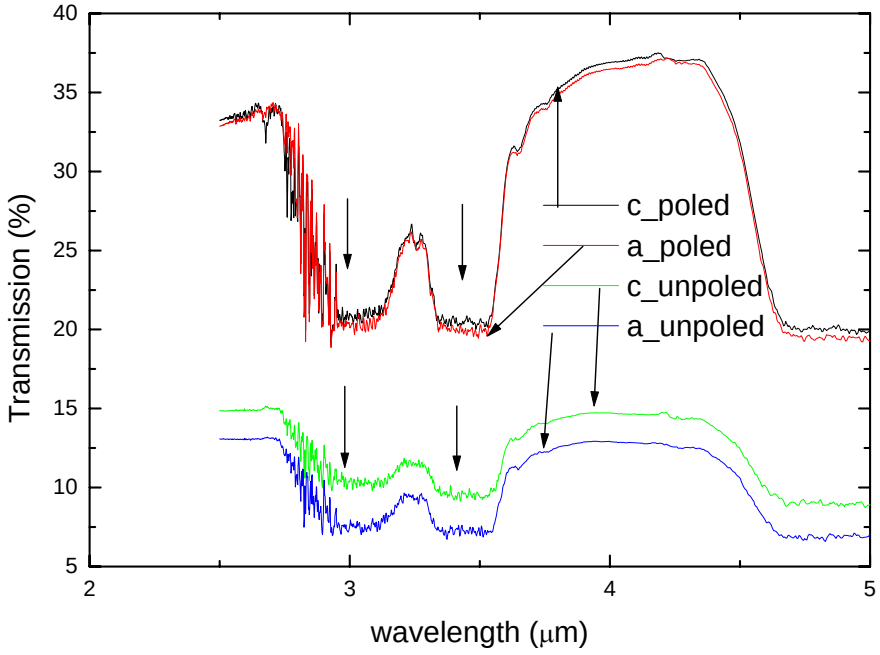

Figure 5.7 Absorption peaks of PZN-0.12PT's FTIR spectrum

Chapter 6

Domain Configuration by Two Dimensional Birefringence Measurement

6.1 Introduction

This chapter deals with the domain configuration as viewed by two dimensional birefringence measurements. First it gives some basic concept of domain and Jones matrix, which is the necessary mathematic tool for two-dimensional birefringence measurement. It is followed by some preliminary test experiments and analysis.

6.1.1 Introduction on ferroelectric domains

Even for a single ferroelectric crystal, usually it does not consist only one domain, since single domain corresponding to higher energy. Lowering the temperature of a single crystal barium titanate with cubic symmetry (m3m) from above 130°C to below Curie point, it has a tetragonal (4mm) symmetry. In this tetragonal state the polarization axis (c axis) is not uniform in the whole crystal, but has six possible directions (three cubic {100} axes. There are only two types of domains, i.e. 90° and 180°, since c axis is originated from an a axis. At room temperature the optical refractive indices along a axis and c axis have a difference $(n_a - n_c) = 0.055$. Due to this birefringence, it is possible to observe the domains in it under transmitting polarized light since the domains are separated by 90° walls,

Figure 6.1 shows a barium titanate single crystal in a ferroelectric state with two domains. The c axis of domain I is c_I, and c_{II} for domain II. Cutting a plate section perpendicular to AB near AC containing only c_I and set it between two-crossed

polarizers, there is no output light while rotating the plate, since the c axis is parallel to the light. This domain is called c-domain for its c axis is perpendicular to the plate. Cutting a plate section perpendicular to ED near EF containing only c_{II} and set it between two-crossed polarizer, there is no output light only at two perpendicular positions while rotating the plate within 180°. This domain is called a-domain for its c axis is parallel to the plate. Cutting a plate section perpendicular to BD near ED and set it between two-crossed polarizer, there is no output light for the domain II part and only at two perpendicular positions for domain I part while rotating the plate within 180°. The polarizations of domain I and domain II are perpendicular to each other, the domain wall is called 90° domain wall. The domain wall must be {011} plane (see Figure 6.2) in order to guarantee that there is no surface charge on the domain wall. A general rule for domain wall orientation is given by Fousek-Janovec criterion [Lines and Glass 1977]. Cutting a plate perpendicular to AC near ABDE and set it between two-crossed polarizer, two perpendicular a-domains are observed, see Figure 6.3, except at only two extinction positions while rotating the plate within 180°. Domain wall can be observed directly by the total reflection when light incidents on domain wall.

There is another important domain wall, 180° domain wall, which is the wall between two opposite polarization domains. From the above discussion, it cannot be distinguished by birefringence since the two c axes are parallel though in opposite direction.

6.1.2 Jones matrix

Generally a polarized light wave with frequency ω, wave number k, propagating along z direction can be expressed as:

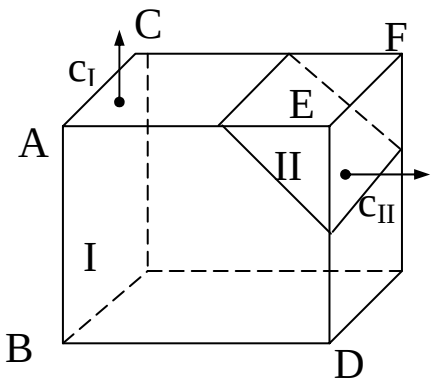

Figure 6.1 $BaTiO_3$ with two domain I and II

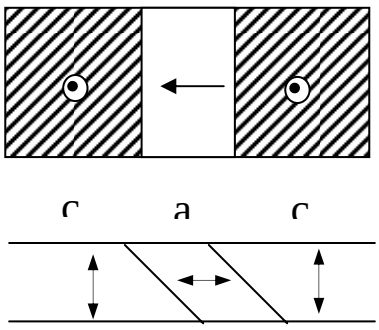

Figure 6.2 90° domain wall between a-domain and c-domain

$$E(z,t) = E_{0x}\cos(\omega t - kz + \phi_x)i + E_{0y}\cos(\omega t - kz + \phi_x)j \tag{6.1}$$

where E_{0x}, E_{0y} the amplitude of x, y component respectively.

Written in complex exponential form and omitting the time dependence by a column notation, which is known as Jones vector [Kliger et al 1990]:

$$E = \begin{vmatrix} E_x \\ E_y \end{vmatrix} = \begin{vmatrix} E_{0x}e^{i\phi_x} \\ E_{0y}e^{i\phi_y} \end{vmatrix} = E_0 \begin{vmatrix} \cos\alpha e^{i\phi_x} \\ \sin\alpha e^{i\phi_y} \end{vmatrix} \tag{6.2}$$

where $E_0 = \sqrt{E_{0x}^2 + E_{0y}^2}$, $\cos\theta = E_{0x}/E_0$, and $\sin\alpha = E_{0y}/E_0$

Only considering the linear interaction between light and the optical materials when the light power or electric field intensity is not high enough. The final output light can be described as:

$$E_{fx} = J_{11}E_x + J_{12}E_y \tag{6.3.a}$$

$$E_{fy} = J_{21}E_x + J_{22}E_y \tag{6.3.b}$$

where J_{ij} are coefficients to be determined from the known properties of the optical material encountered by the light. Using the Jones vector, equation (6.3) becomes:

$$\begin{vmatrix} E_{fx} \\ E_{fy} \end{vmatrix} = \begin{vmatrix} J_{11} & J_{12} \\ J_{21} & J_{22} \end{vmatrix} \begin{vmatrix} E_x \\ E_y \end{vmatrix} \tag{6.4}$$

where the matrix J is the so called Jones matrix.

The electric vector of a light wave that passes through an optical medium with refractive index n and extinction coefficient κ is scaled by a factor of $e^{-i\frac{2\pi}{\lambda_0}d(n-i\kappa)}$, where d is the distance propagated in the medium and λ_0 is the wavelength in vacuum. When a polarized light passes through an optical medium with optical axis parallel to the light electric field, i.e. x and y. Then equation (6.3) becomes:

$$E_{fx} = E_x e^{-i\frac{2\pi}{\lambda_0} d(n_x - i\kappa_x)} = N_x E_x \tag{6.5a}$$

$$E_{fy} = E_y e^{-i\frac{2\pi}{\lambda_0} d(n_y - i\kappa_y)} = N_y E_y \tag{6.5b}$$

So the matrix representing a linear polarizer or retarder with optical axes oriented along the a and y direction can be conclude as:

$$J(0) = \begin{vmatrix} N_x & 0 \\ 0 & N_y \end{vmatrix} \tag{6.6}$$

where (0) denotes no rotation of the optical axes with respect to the coordinate axes. By rotating the coordinate axes it is straightforward to get the matrix $J(\beta)$ for a linear polarizer or retarder with its optical axes rotated by angel β (positive for counterclockwise rotation from the x axis, see figure 6.4) from the coordinate.

$$J(\beta) = R(-\beta) J(0) R(\beta) \tag{6.7}$$

where $R(\beta) = \begin{vmatrix} \cos\beta & \sin\beta \\ -\sin\beta & \cos\beta \end{vmatrix}$ (6.8)

For an ideal horizontal polarizer, the x component of the electric vector passes without attenuation while the y component is attenuated completely. So $N_x = 1, N_y = 0$, thus,

$$J_P(0) = \begin{vmatrix} 1 & 0 \\ 0 & 0 \end{vmatrix} \tag{6.9}$$

The Jones matrix of a polarizer oriented at an angel β from the positive x axis can be calculated directly by equation (6.7), (6.8), and (6.9),

$$J_P(\beta) = \begin{vmatrix} \cos^2\beta & \sin\beta\cos\beta \\ \sin\beta\cos\beta & \sin^2\beta \end{vmatrix} \tag{6.10}$$

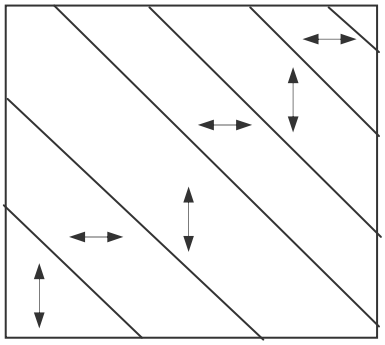

Figure 6.3 90° domain wall between a-domains

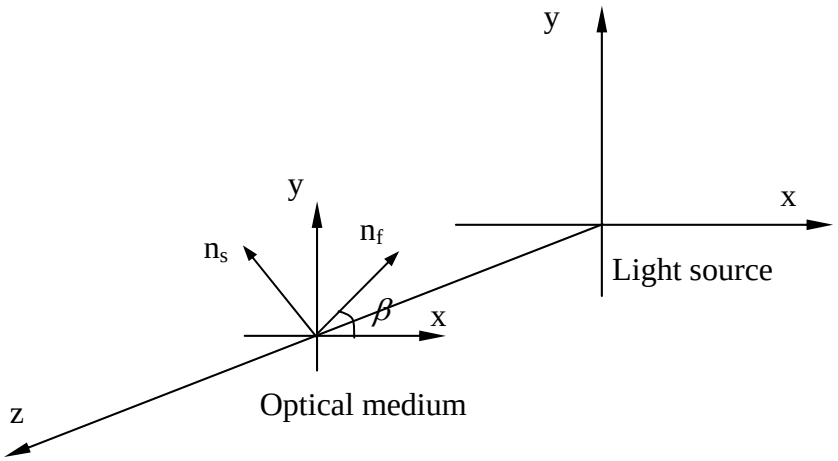

Figure 6.4. Definition of coordinate system

Now considering a linear retarder, which is defined by two parameters. First one is the retardation θ, which is defined by:

$$\theta = \frac{2\pi}{\lambda_0}(n_s - n_f)d \tag{6.11}$$

where n_s and n_f are the optical refractive index of the slow axes and fast axis respectively. Another one is azimuthal angle ϕ of fast axis, the angle between the fast axis and the x axes, which is defined as positive by counterclockwise rotation from the x axes when looking toward to the light source. Assuming the extinction coefficient κ is isotropic, i.e. $\kappa_s = \kappa_f = \kappa$, then Jones matrix with zero fast axis angle retarder is given by:

$$J_R(0,\theta) = \begin{vmatrix} e^{-i\frac{2\pi}{\lambda_0}d(n_f - i\kappa)} & 0 \\ 0 & e^{-i\frac{2\pi}{\lambda_0}d(n_s - i\kappa)} \end{vmatrix} = e^{-i\frac{2\pi}{\lambda_0}d(n_x + n_f) - i\kappa)} e^{-\frac{2\pi}{\lambda_0}d\kappa} \begin{vmatrix} e^{i\frac{\theta}{2}} & 0 \\ 0 & e^{-i\frac{\theta}{2}} \end{vmatrix} \tag{6.12}$$

We are only interested in relative phase and for the intensity study the first exponential factor will vanish with its conjugate term. Given no extinction all the exponential factor can be dropped out and the Jones matrix is

$$J_R(0,\theta) = \begin{vmatrix} e^{i\frac{\theta}{2}} & 0 \\ 0 & e^{-i\frac{\theta}{2}} \end{vmatrix} \tag{6.13}$$

Once again, by using equation (6.7) and (6.8), the Jones matrix of a retarder with fast axis angle ϕ can be derived as,

$$J_R(\phi,\theta) = \begin{vmatrix} \cos^2\phi e^{i\frac{\theta}{2}} + \sin^2\phi e^{-i\frac{\theta}{2}} & i\sin 2\phi \sin(\frac{\theta}{2}) \\ i\sin 2\phi \sin(\frac{\theta}{2}) & \cos^2\phi e^{-i\frac{\theta}{2}} + \sin^2\phi e^{i\frac{\theta}{2}} \end{vmatrix} \tag{6.14}$$

6.1.3. Single Domain:

Ferroelectric crystals are all birefringent materials in their ferroelectric phase. The birefringence of domain is dependent on the spontaneous polarization. When polarized light wave passes through a single ferroelectric domain, it is just the case of a linear retarder. So the Jones matrix is just equation (6.14)

6.1.4. Two 90° domains

What's the Jones matrix for two 90° domains? As shown in Figure 6.5, light propagates perpendicular to plane ABCD. When light encounters in region ABCGF, it propagates only in domain I while only in domain II if encountering in region EHD. Light passes through domain I then domain II when light incidents in region EFGH. (α,θ), (β,γ) are denoting the fast axis angle and retardation of domain I and domain II, respectively.

$$J(\alpha,\theta;\beta,\gamma) = R(-\alpha)J_1(0,\theta)R(\alpha)R(-\beta)J_2(0,\gamma)R(\beta) \tag{6.15}$$

noting $\beta = \frac{\pi}{2} + \alpha$, equation can be simplified as:

$$J(\alpha,\theta;\beta,\gamma) = \begin{vmatrix} -\cos^2\alpha e^{i\frac{\theta-\gamma}{2}} - \sin^2\alpha e^{-i\frac{\theta-\gamma}{2}} & i\sin 2\alpha \sin(\frac{\theta-\gamma}{2}) \\ -i\sin 2\alpha \sin(\frac{\theta-\gamma}{2}) & \cos^2\alpha e^{-i\frac{\theta-\gamma}{2}} + \sin^2\alpha e^{i\frac{\theta-\gamma}{2}} \end{vmatrix} \tag{6.16}$$

This equation is very similar to the one of a single domain, but it is not straightforward to identify the average fast axis angle and total retardation. It's reasonable to take $(\theta-\gamma)$ as the total retardation of these two domains. Firstly, the retardation is θ for the first domain while the second one should be $-\gamma$ since the direction of its fast axis and slow axes exchanged. Secondly, the retardation is θ for one

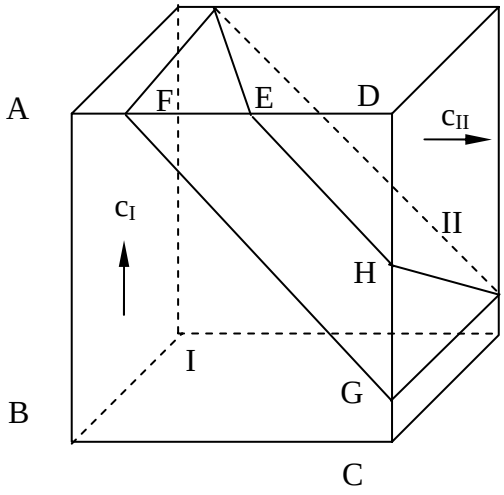

Figure 6.5 Light passing through two 90° domain

domain while all the phase term containing $\theta/2$ in equation (14); while by observing the phase factoring equation (16), they all contain the term of $(\theta-\gamma)/2$.

6.1.5. Three 90° domains

Now considering the Jones matrix of three 90° domains. Assuming that there is a third 90° domain (ρ,σ) after that two 90° domain. $\rho=\beta\pm\pi/2$. For the case of $\rho=\beta-\pi/2$, then $\rho=\alpha$,

$$J(\alpha,\theta;\beta,\gamma;\rho,\sigma)=R(-\alpha)J_1(0,\theta)R(\alpha)R(-\beta)J_2(0,\gamma)R(\beta)R(-\rho)J_3(0,\sigma)R(\rho) \quad (6.17)$$

$$\text{Noting, } R(\alpha)R(-\beta)=R(\beta)R(-\rho)=\begin{vmatrix}0 & -1\\ 1 & 0\end{vmatrix} \quad (6.18)$$

$$\text{So, } R(\alpha)R(-\beta)J_2(0,\gamma)R(\beta)R(-\rho)=-J_2(0,-\gamma) \quad (6.19)$$

$$\text{And, } J_1(0,\theta)J_2(0,-\gamma)J_3(0,\sigma)=J_3(0,\alpha-\gamma+\sigma) \quad (6.20)$$

$$\text{Finally, } J(\alpha,\theta;\beta,\gamma;\rho,\sigma)=-J(\alpha,\theta-\gamma+\sigma) \quad (6.21)$$

For the case of $\rho=\beta+\pi/2$, then $\rho=\alpha+\pi$, the same result as equation (6.21) is obtained. Since the light intensity is the measurement parameter in our experiment, the minus sign can be omitted without affecting the results. So Jones matrix of three 90° domains is

$$J(\alpha,\theta;\beta,\gamma;\rho,\sigma)=J(\alpha,\theta-\gamma+\sigma) \quad (6.22).$$

Unlike the case of two 90° domains, the total retardation and fast axis angle of three 90° domains are easy to determine. The total retardation is $\theta-\gamma+\sigma$, and the fast axis angle is α, the same as the fast axis angle of the first domain. So three 90° domains can be treated as a single domain $(\alpha,\theta-\gamma+\sigma)$. Moreover, the total effect of odd 90°

domains can be treated as a single domain with the fast axis angle of α, the fast axis angle of the first domain, and the retardation θ is

$$\theta = \sum_k (-1)^{k+1} \theta_k \tag{6.23}$$

And then all the even 90° domains can be treated as two 90° domains.

6.2 Experimental Approach

6.2.1 System test

6.2.1.1. Measurement Principle and Setup

Figure 6.6 shows the fundamental setup of the rotating analyzer method for the two-dimensional birefringence measurement. The actual arrangement of its optical system is schematically drawn in Figure 6.7. An incident laser light passes through a polarizer and a quarter-wave plate to generate a circularly polarized light and then propagates through an uniaxial crystal under test. The relative phase shift θ is caused in the uniaxial medium and the principal birefringence axis (i.e., the fast axis) has an angle ϕ measured from the horizontal *y* axis. The Jones matrix representation of the output light passing through an analyzer that is rotated by an angle Φ relative to the *y* axis is given by [Ohmi 1994; Nishida and Yamanaka 2001]

$$\begin{bmatrix} E_x \\ E_y \end{bmatrix} = \begin{bmatrix} \sin^2\Phi & \sin\Phi\cos\Phi \\ \sin\Phi\cos\Phi & \cos^2\Phi \end{bmatrix} J_R(\phi,\theta) \frac{1}{\sqrt{2}} \begin{bmatrix} 1 & i \\ i & 1 \end{bmatrix} \begin{bmatrix} 1 \\ 0 \end{bmatrix} \tag{6.24}$$

$J_R(\phi,\theta)$ is given by equation (6.14).

The optical output intensity *I* is then straightforwardly obtained as

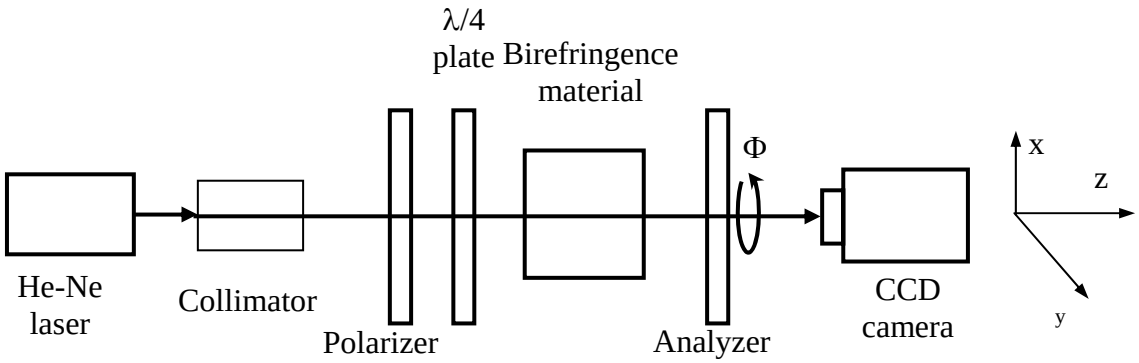

Figure 6.6 Schematic experiment setup

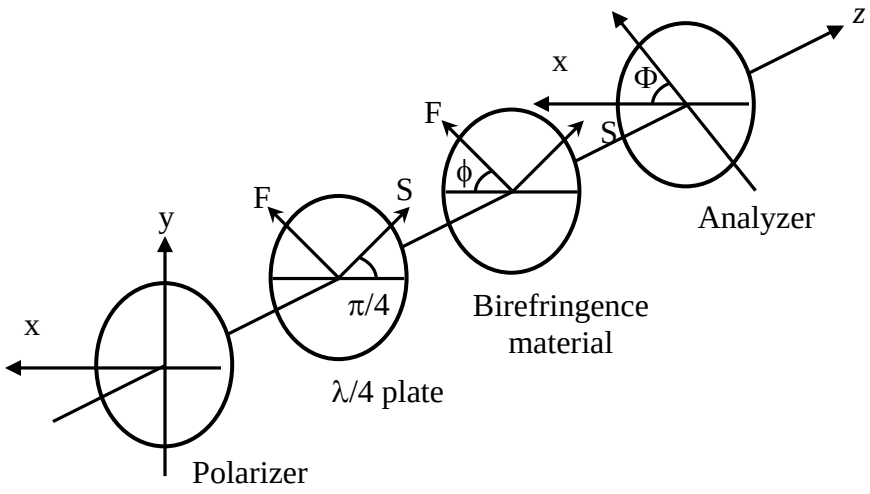

Figure 6.7 Schematic arrangement of optical device

$$I = |E_x|^2 + |E_y|^2 = \frac{I_o}{2}[1 - \sin 2(\Phi - \phi)\sin\theta], \tag{6.25}$$

where I_o is the incident intensity. A CCD camera detects the 2-D intensity data while the analyzer is rotated about the axis of laser beam in steps of a fixed rotation angle. Then calculations are carried out in a computer for each pixel of the captured image data and the 2-D birefringence vector distribution (ϕ, θ) in the sample is obtained simultaneously. However, the rotation of the analyzer causes the additional change of the transmitted intensity I regardless of performance of the optical measurement system characterized by equation (6.25). In other words, the spatial nonuniformity of the analyzer resulting from the production quality or some defects on its surfaces changes its optical transmittance distribution at different rotation angles, which in turn lower the sensitivity of the 2-D measurement depending on the optical characteristics of the analyzer. Therefore, the transmitted intensity I at each pixel of the image data given by equation (6.25) can be modified as

$$I = |E_x|^2 + |E_y|^2 = T(\Phi)\frac{I_o}{2}[1 - \sin 2(\Phi - \phi)\sin\theta] \tag{6.26}$$

Here $T(\Phi)$ accounts for the nonuniformity due to the analyzer rotation. It is a function of Φ and its cancellation is required to improve the measurement sensitivity. To this end, the rotating analyzer method is applied again without installing the uniaxial material to be tested as shown in Figure 6.6.

$$I = T(\Phi)\frac{I_o}{2} \tag{6.27}$$

As shown in Figure 6.6, a He-Ne laser (632.8 nm) is used for an input light source and a beam attenuator controls its intensity. The beam is collimated and passing through

the following polarizer and quarter-wave plate. Here a voltage-controllable nematic liquid crystal retarder is used as the sample whose optical performance (i.e., the retardation θ as a function of voltage) is obtained as shown in Figure 6.8. The transmitted light intensity via the analyzer is recorded by the CCD camera and then sent into the computer system for image processing to obtain the 2-D birefringence vector distribution (ϕ, θ).

The procedure of measurement and image processing is as following. The first step is to measure 19 intensity profile images from – 90° to 90° by 10° increments without the sample in order to obtain $T(\Phi)$ effect given by equation (6.27). After arranging the sample in the optical measurement system, the same measurement as that of the first step is repeated to obtain the 2-D distribution of the retardation θ and the fast axis direction ϕ in the nematic liquid crystal. Then all 36 intensity data are filtered out to reduce the spatial noise and to remove dust or scratches in the intensity image. The nonuniformity effect $T(\Phi)$ due to the rotation of the analyzer is compensated by dividing the intensity data I measured without the sample at the same rotation angle Φ, and then the birefringence vector distribution (ϕ, θ) in the birefringence material can be calculated by equation (6.26).

6.2.1.2 Experimental Results and Discussions

Original 2-D intensity images are taken by the CCD with changing the rotation angle Φ of the analyzer under the experimental setup as shown in Figure 6.6. Each captured image data has a total of 300 × 400 pixels with 8 bits of gray level. A square

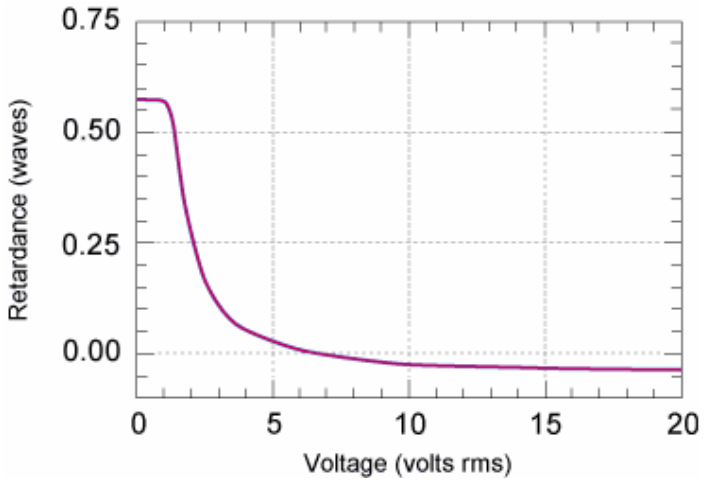

Figure 6.8 Optical performance of the voltage-controllable nematic liquid crystal retarder at 632.8 nm (Source: Meadowlark Optics 1999-2000 catalog).

region with a size of 100 × 100 pixels at the center of image is displayed in Figure 6.9 and used for image processing. As can be seen from Figure 6.9, the mechanical rotation of the analyzer contributes to the nonuniform intensity distribution at different rotation angles. Thus the performance of the rotating analyzer method could be limited by the optical quality of the analyzer and the compensation of this effect might be required. Before moving to image processing to calculate the birefringence vector (ϕ,θ), the defect pattern caused by scratches or dust on the surfaces of the optical components and the spatial noise are removed to some extent by the image filtering as shown in Figure 6.10.

Figure 6.11 and Figure 6.12 show the 2-D distributions of the retardation θ and the fast axis angle ϕ of the principal birefringence axis (i.e., the fast axis) in the voltage-controllable nematic liquid crystal retarder for different voltage. For a convenient visualization of fast axis angle, each neighboring 5×5 pixels is averaged and corresponds to one arrow in the 2-D profile of ϕ. Here note that the long axis of the liquid crystal molecules is defined as the slow axis, which is characterized by the extraordinary index. With no voltage presenting, the molecules lie parallel to the surfaces of the nematic liquid crystal plate and the maximum retardation is obtained. As the voltage applied across the liquid crystal layer increases, the molecules become reoriented such that the slow axis moves to be parallel to the applied electric field. Thus the effective birefringence decreases and it causes a reduction in the retardation θ with the increased applied voltage as shown in Figure 6.10(b) and 6.11(b). From the chart in Figure 6.8, the retardations are around 14° and 7° for voltage 3.23V, 3.99V respectively. The calculated results are in good agreement with these values after considering the

deviation. The deviation is decreased with higher voltage. This is corresponding to the liquid crystal molecules arranging more uniformly. However, the direction of the fast axis θ that is originally aligned parallel to the windows of the liquid crystal plate does not change, independent of the applied voltage as shown in Figure 6.10(a) and 6.11(a). The 2-D distribution of the birefringence vector (ϕ, θ) in the testing liquid crystal is quite uniform, and the signal-to-noise ratio (SNR) decreases when the induced effective retardation comes close to 0° by increasing the applied voltage.

6.2.3 Conclusion

The test experiment verified the effectiveness of the rotation analyzer method for a single domain, and so for odd number of stacked domains. While applying this method to even number of stacked domains, Jones matrix $J_R(\phi, \theta)$ in equation (6.24) should be given by equation (6.16). While, the output intensity is:

$$I = |E_x|^2 + |E_y|^2 = \frac{I_o}{2}\left[1 - \sin 2(\Phi + \phi)\sin\theta\right] \tag{6.28}$$

For this case, the retardation can be calculated the same way as one domain, but the fast axis angle will change sign. For a real measurement, this method alone cannot determine the sign of the fast axis angle in a single measurement configuration. However, the retardation is reliable. Then the total thickness of these two direction 90° domains can be concluded since the total thickness is fixed and measurable. The growth of these two direction 90° domains can be also measured under external bias condition, such as electric field, stress, and change of temperature. To identify the orientation of the domain, it is only necessary to know the change of the fast axis angle but the exact distribution of it. Sudden changing the sign of the fast axis angle will not happen if all the reorientation

behavior of domains goes gradually, which is true for materials at temperature well removed from phase transitions. Thus keeping the same sign of the fast axis angle will give the orientation of the domain.

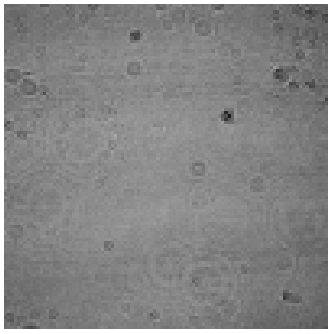

Φ = – 90°

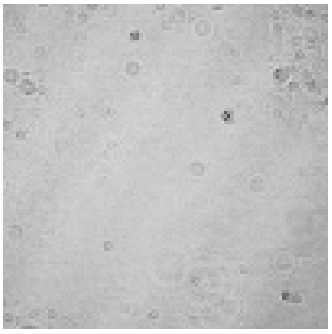

Φ = – 40°

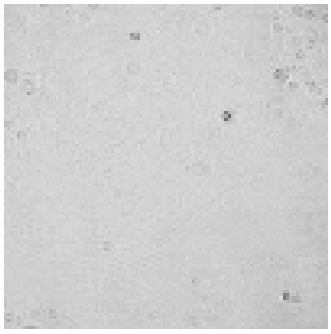

Φ = 10°

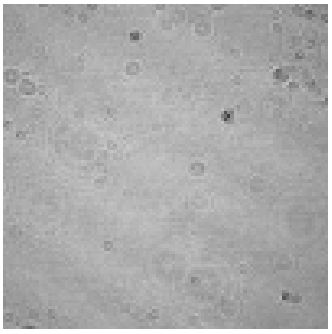

Φ = 60°

Figure 6.9 Original 2-D intensity images captured by CCD with changing the rotation angle of the analyzer

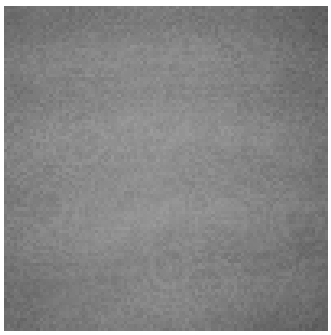

Φ = – 90°

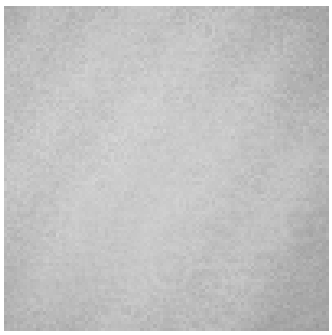

Φ = – 40°

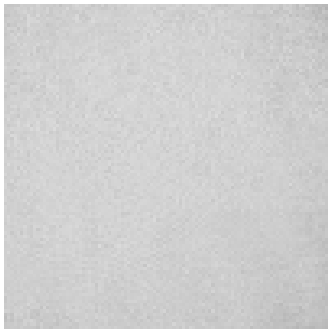

Φ = 10°

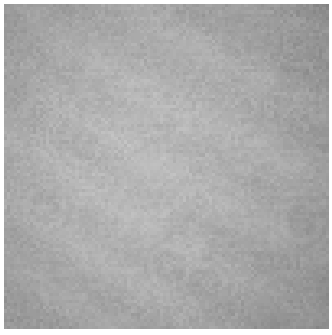

Φ = 60°

Figure 6.10 Filtered 2-D intensity images for the different rotation angle of the analyzer.

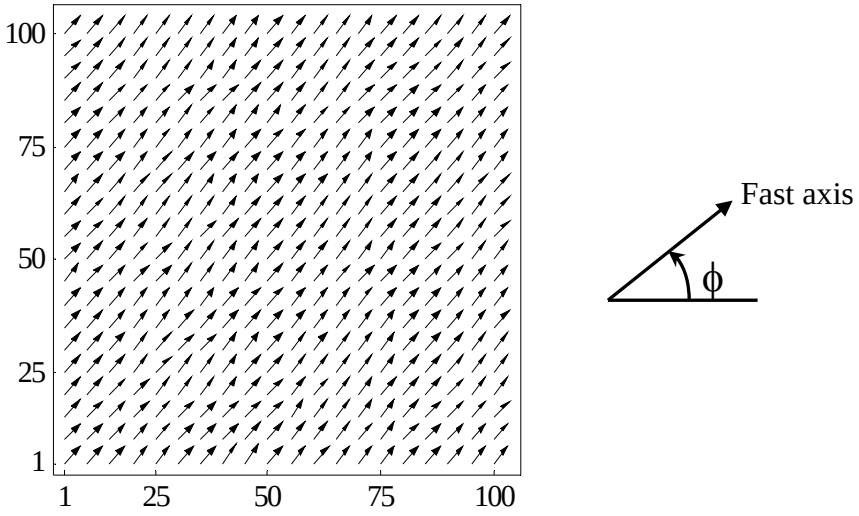

(a) 2-D profile of fast angel ϕ, average: 48.61 deg., standard deviation: 5.06 deg.

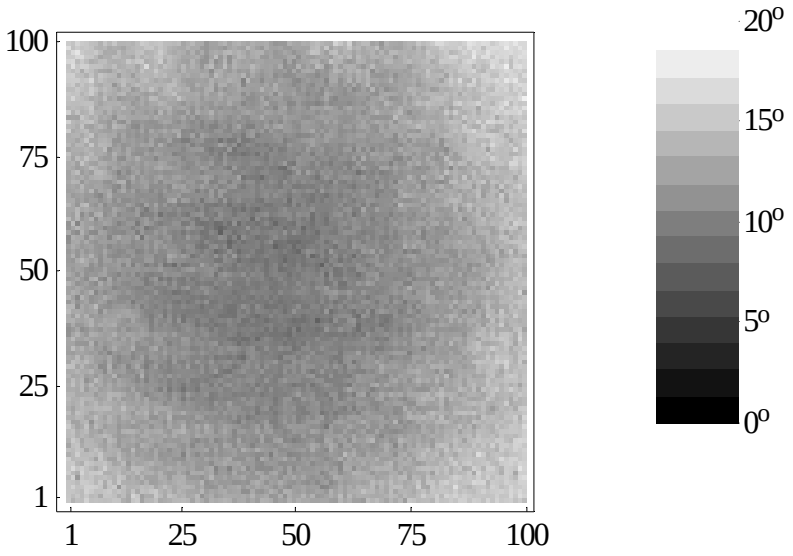

(b) 2-D profile of the retardation θ, average: 12.5 deg., standard deviation: 1.866 deg.

Figure 6.11 2-D profile of birefringence (ϕ, θ) with applied voltage 3.23V

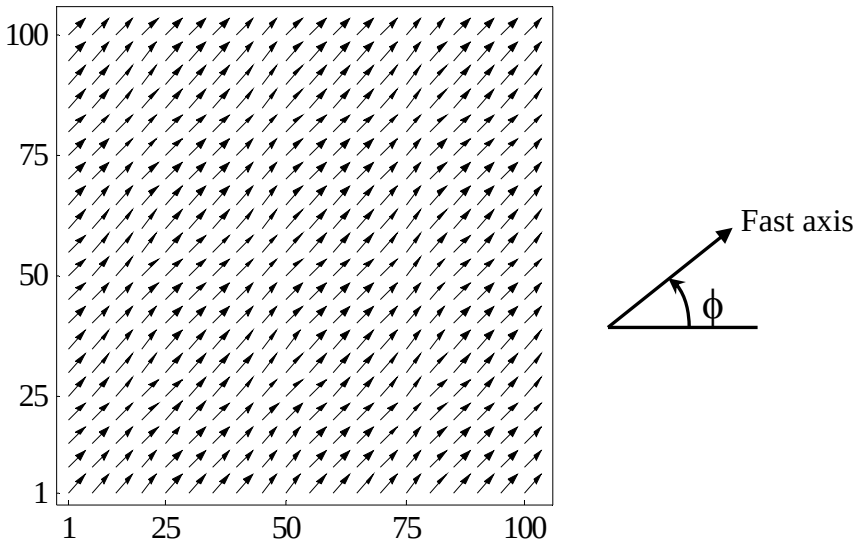

(a) 2-D profile of fast angel ϕ, average: 49.91 deg., standard deviation: 2.54 deg

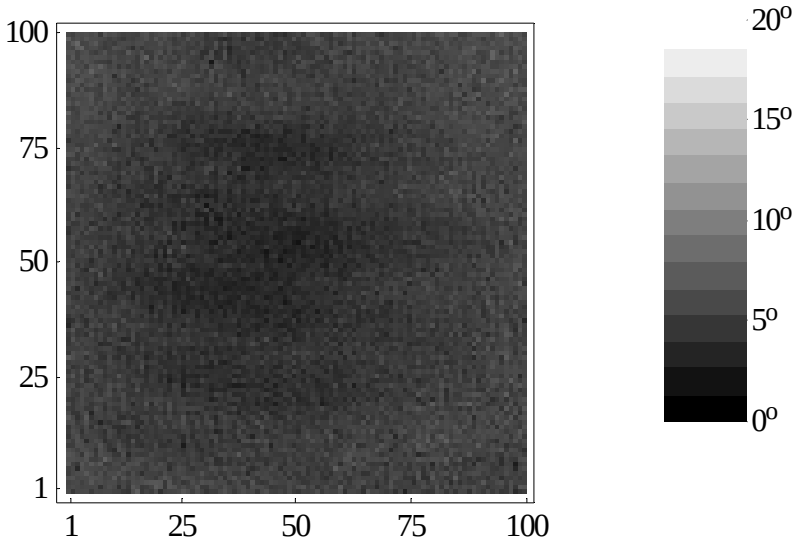

(b) 2-D profile of the retardation θ**,** average: 6.56 deg, standard deviation: 0.92 deg,

Figure 6.11 2-D profile of birefringence (ϕ, θ) with applied voltage 3.99V

Chapter 7

Discussion and Conclusion

7.1 Discussion and conclusion

7.1.1 Local Polarization and Burns Temperature

As a peculiarity of relaxor ferroelectrics, the Burns temperature so far has not been well understood. The Burns temperature was first discovered by Burns and Dacol [Burns and Dacol, 1983a, b] in the ferroelectric systems of PLZT, PMN, and PZN by optical refractive index measuement. Later it was found the existence of the burns temperature in more ferroelectrics system of PTiSn, KSR [Burs and Dacol, 1990a], BSN [Bhalla et. al, 1987], and BSKNN [Bhalla et. al, 1992]. Now it is believed that the Burns temperature, marking the appearance of significant deviation of refractive index or birefringence from quasilinear temperature dependence, is one of the intrinsic characters of the relaxor ferroelectrics with diffuse phase transition. So far the determination of the Burns temperature is by means of the optical method measuring either the refractive index or birefringence, while it can be supported by other method such as neutron scattering spectrum [Gerhring et. al. 2001] and Raman spectrum [Svitelskiy et. al., 2005].

Burns and Dacol connected this deviation with the onset of the formation of polar nanoregions, caused local polarization consequently. The breakdown of translation symmetry resulting from the heterogeneous ions on crystallographic sites leads variation of Curie temperature for nanoregions which undergo transition to a lower symmetry polar state before others. It is notable that the local polarization P_d derived from refractive index or birefringence is not from any detailed microscope model but general symmetry consideration. Δn_3 or $\Delta n_{31} \propto P^2$ come from the fact the high temperature phase can be

treated as centrosymmetric and any polarization (local or macroscopic) can be treated as an expansion at P=0. Thus the first term will be P^2 term. It also should be reminded that the derived local polarization P_d is really the mean square root $\sqrt{\bar{P}_d^2}$. This keeps the answer of the question whether the observed polarization is static or dynamic unknown while the average polarization is zero. In general, one would expect that dynamical inversion of P_d in nano polar region would be modulated by a weak external E_3 field so as to change the fraction of up and down polarizations and thus contribute a significant component to the dielectric polarizability. In the static model the dipolar component which appears at temperature well above is already frozen. Polarizability would now be contributed by expansion and contraction of the polar region and the dielectric maxima would be essentially due to cooperative ordering.

Vakhrushev and Shapior [Vakhrushev and Shapior, 2002] have directly observed a soft ferroelectric mode associated with the Curie-Weiss behavior of the dielectric constant by inelastic neutron scattering measurements of PMN. The frequency of the soft mode exhibits a minimum near the Burns temperature. This confirmed that at the Burns temperature a local phase transition occurs resulting in a crossover of the critical dynamics. Above T_d the dynamics is of displacive type, while below it is governed by a relaxation of the large polar regions.

More recently Toulouse et. al.[Toulouse, et. al., 2005, Svitelskiy, et. al., 2005] proposed that the Burns temperature (in order to avoid confusion the Burns temperature denoted as T_B hereafter) is not the temperature when polar nanoregion appear, but the temperature at which the life time of the dynamic correlations between the off-center Pb ions exceeds the period of the TO phonon, then appearing static on the time scale of the

phonon (or quasidynamic on the absolute time scale) after their investigation on the Raman spectrum of PZN. This crossover from fully dynamic to quasidynamic is marked by a narrowing down of the low frequency features of the Raman spectrum, the disappearance of the long wavelength TO phonon from the inelastic neutron scattering spectrum as well as a faster-than-linear decrease with temperature of the refractive index. It's also the temperature at which the growing lifetime of the dynamic correlations between off-center ions exceeds the inverse frequency of the TO phonon. Above T_B, the local intersite motion of the off-center ions is fast and uncorrelated, dynamically broadening the TO phonon. Below T_B, these correlations, though still dynamic in the absolute (absence of local strain fields), will appear static to the TO phonon whose frequency will then increase. The permanent polar nanoregions appear at so-called 'intermediate temperature' T_d, which is between the Burns temperature T_B and freezing temperature T_f. At T_d local phase transitions begin to take place. Because these are local, they generate local strain field. Thus T_d marks the onset of local phase transition, or the appearance of static or permanent correlations of the off-center ion displacements as well as the off-centering of other previously on-center ions. The temperature range between T_d and T_f is dominated by the rotation of the polar nanoregions and can appropriately be designated as a quasistatic stage. The freezing temperature T_f is marked by a drastic overall drop in scattered intensity and abruptly changes in the Raman spectrum, which strongly suggest an arrest of the low frequency relaxational motion. It is also the temperature at which the frequency dependence disappears in the dielectric constant and an underdamped TO phonon reappears in the neutron scattering spectrum. Below T_f, the

dynamic appears to be dominated by renormalized TA-TO coupling induced by static disorder.

Whether the Burns temperature marks the appearance of the polar nanoregion is critical for the optical measurement of PBN57. If it's true, then both the measurement of refractive index and birefringence should yield the same Burns temperature for each wavelength. However, even if this is true, the difference of the Burns temperature can only ascribe to the measurement error. As mentioned in chapter 3 that the unstable high temperature the refractive index could not yield the true Burns temperature, and generating such error is possible.. If the above model is true, i.e. the Burns temperature marks the crossover between the soft mode and order-disord dynamics. And the Burns temperature for refractive index and birefringence are not necessary the same.

7.1.2 Optical Curie Region

In chapter 3 the optical Curie region is defined as the temperature region between the deviation temperatuire T_D and the Burns temperature T_d. Both the coupling between the light and the nano/micro polar regions and the dipole-dipole interaction between polar regions resulted in the optical Curie region, which decreases with optical frequency. This is shown in the Figure 8.1 with two aspects. The average size of polar regions at low temperature is lager than that at high temperature since in relaxor ferroelectrics the macrodomain transforms to microdomain with increasing temperature, i.e. the average size of polar region decreases with temperature. On the other hand a certain frequency is more sensitive to some polar regions with a corresponding sizes but almost invisible to other polar regions with much different sizes if considering coupling between light waves and polar regions. Thus there is a one-to-one map between any two of the three amounts:

the light frequency, the deviation temperature, and the size of polar regions. The large frequency of light corresponds to small size polar regions while the latter prefer high temperature.

The optical Curie region decreases with frequency. The deviation temperature T_D and the Burns temperature T_d have the tendency that approaches to the T_m with a high enough frequency, and the relaxor ferroelectric behaves maybe more like a normal ferroelectric. The deviation temperature significantly marks the breakup of macroscopic polar-regions approaching relaxor phase transition. It's reasonable to analogize the deviation temperature to freezing temperature T_f since the freezing temperature marks the ending of the diffuse phase transition. If the frequency is low enough that has no coupling with polar regions at all, the deviation temperature maybe approach to freezing temperature T_f. Thus one can speculate that the frequency dependent deviation temperature has an upper bound, i.e. temperature of dielectric maxima, T_m, and a low bound, freezing temperature T_f.

With the accurate determined deviation temperature it is possible to estimate the average size of the polar regions at different temperature.

The isotropic temperature T_i has the same trend with frequency as dielectric maximum temperature T_i. However this is not common phenomenon for relaxor ferroelectric. This only occurs for the relaxor whose birefringence has different sign in the high temperature paraelectric state and low temperature ferroelectric state. The existence of isotropic temperature T_i is of great interest for application, such as optical valve.

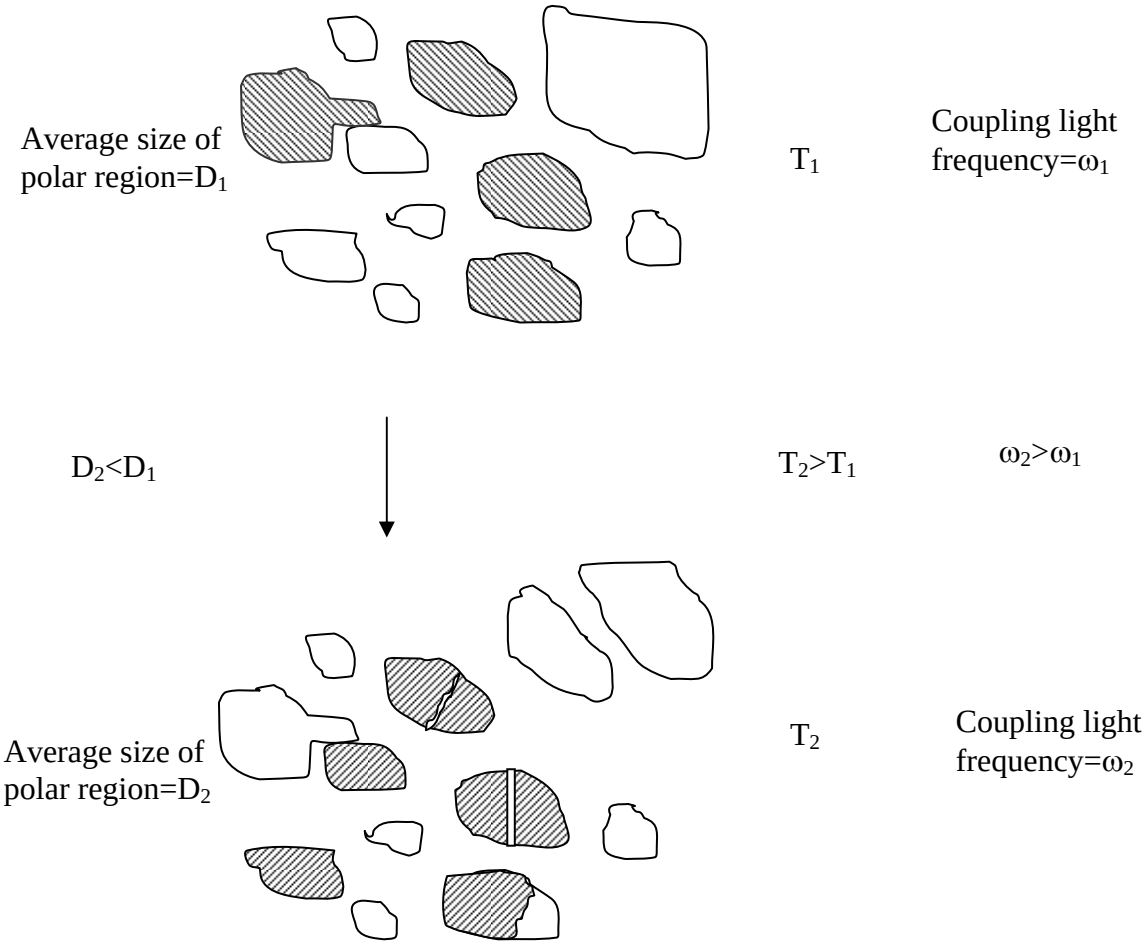

Figure 7.1 Illustration of the coupling between light and polar regions at different temperature

7.1.3 Dipole-Dipole interaction

It was turned out that the interaction between the polar regions in relaxor ferroelectrics system could not be omit. First, the interaction between the polar regions distinguishes the relaxor ferroelectrics from normal dielectrics whose optical refractive index can be describe by the single oscillator model, resulting the existence of optical Curie region. Second, thermo-optic coefficients in the low temperature ferroelectric state have major contribution from polarization term. These two are the most direct proofs for nonneglectable interaction between polar regions. The last one is coming from the results of transmission spectrum of PZN-0.12PT. The derived energy of the phonon is two large to be considered as phonon energy but rather the orbit-spin interaction or the interband transition. The interaction between the polar regions could make the energy band splitting very complicate and make the interband transition possible. Recently more and more theories model based on random field can give some explain for experiment. Taking into account the interaction between polar regions is the essential part of random field.

7.2 Major results and conclusions

1)Temperature dependent birefringence and optical refractive indices of PBN ($Pb_{1-x}Ba_xNb_2O_6$) crystal (1-x=0.57) were measured in several optical wavelengths (λ= 694nm, 633nm, 535nm, and 450nm) to understand the optical frequency dependency of ferroelectric phase transitions in relaxor ferroelectric crystals of tungsten bronze structure. Local polarization is verified to be dynamically activated by thermal process and probed effectively by suitable wavelength of light. An optical isotropic point, as

function of temperature and light frequency, is reported at which the crystal's standing birefringence is fully compensated by polarization.

2) A modified single oscillator model is used to calculate the index of refraction in the ferroelectric phase. The deviation temperature from the single oscillator model is reported to be significant marking the crossover from macroscopic to microscopic polarization. A new parameter, optical Curie temperature region, defined by the temperature difference between the well known Burns temperature and the deviation temperature (from the single oscillator model for index of refraction) is explored for its significance in depolarization behavior of the micro- to nano-polar regions of the ferroelectric relaxor.

3)Temperature dependent optical index of refraction of PZN-0.12PT (1-x)$PbZn_{1/3}Nb_{2/3}O_3$-x$PbTiO_3$, x=0.12, were also studied with emphasis on poling effect. The refractive index n_3 decreases as a result of [001] poling. Temperature dependent effective energy of dispersion oscillator E_0 and dispersion energy E_d were calculated using single oscillator model and found that E_0 and E_d increased by 32% and 60% after [001] poling, respectively. Birefringence of poled PZN-0.12PT also was measured with several frequency and varying temperature. The polarization derived from refractive index and birefringence were consistent with each other. The remnant polarization was increased by approximately 30% as a result of [001] poling.

4) Transmission spectrum of PZN-0.12PT was measured from near UV to IR for both poled sample and unpoled sample. Transmission was improved significantly after poling. By analyzing the transmission spectrum in the visible range, optical band gap and

lattice phonon were determined. The existence of hydrogen in PZN-0.12PT single crystal grown by flux method was postulated based on evidence obtained by FTIR.

5) For accurate and fast birefringence measurement, which is of fundamental important to device design, quality control, and various sensing functions, a two-dimensional birefringence profiling and analysis system was designed and implemented successfully. Jones matrices of two and three 90° domains are derived and conclude that odd number of stacked 90° domains can be treated as a single 90° domain while even number of stacked 90° domains can be treated as two 90° domains. By rotating analyzer method a test experiment using voltage controllable liquid crystal as sample is demonstrated.

-

7.3 S**uggestion for future work**

An extension of the present study can be made into areas related this work but not explore. The following are but a few suggestions for the future work.

1) Apply the whole procedure, including the measurement of optical refractive index and birefringence and data modeling, to other relaxor ferroelectric composition. Check if the freezing temperature T_f is the limitation of the frequency dependent deviation temperature T_D.

2) Continue to verify the optical Curie region with higher frequency, Combine with other measurement methods, such as SEM, to explore to relation of light wavelength with the size of polar regions

3) Temperature dependent transmission would be interesting to explore how the optical bandgap changes with temperature.

4) Temperature dependent IR spectroscopy to explore the TO phonon.

5) Using the 2D index mapping system to study the domain under varying temperature and other conditions.

References:

Abe S., Fujishima T., Tsubone T., Fujimura R., Ono H., Matoba O., Oda K., Shimura T., and Kuroda K., *Opt.Lett*. **Vol.28**, No. 6 ,440(2003)

Abedin K. S., Ito H., *J. Appl. Phys.* **80**, 6561 (1996)

Arabidze A. A. and Chikvaidze B. Ya., *Sov. Phys. Solid State*, **21**(4), 722(1979)

Barad Y., Lu Y.,. Cheng Z. Y, Park S.-E., and Zhang Q. M., *Appl. Phys. Lett*. **77,** 1247 (2000).

Beudon D., Boudjema E. H., Bihan R.L., Jpn. J. Appl. Phys. Supplement, 24 (2), 545 (1985)

Bhalla A. S., Guo R., Cross L. E., Burns Gerald, Dacol F. H., and Ratnakar R. Neurgaonkar, *Phys. Rev. B* **36**, 2030 (1987)

Bhalla A.S., Guo R., and Cross L.E., Burns Gerald, Dacol F. H., and Ratnakar R. Neurgaonkar, *J. Appl. Phys*. **71**, 11 (1992)

Blinc R., Dolinsek J., Gregorovic A., Zalar B., Filipic C., Kutnjak Z., Levstik A., and Pirc R., *Phys. Rev. Lett*. **83**, 424 (1999)

Blinc R., Gregorovič A., Zalar B., Pirc R., and Lushnikov S. G., *Phys. Rev. B* **61**, 253 (2000).

Bobnar V., Kutnjak Z., Pirc R., Blinc R., and Levstik A., *Phys. Rev. Lett*. **84**, 5892 (2000)

Brebner J. L., Jnadl S., Lepine Y., *Phys. Rev*. **B23**, 3816(1981)

Burns G. and Dacol F. H., *Solid State Commun.*, 4**8**, 853 (1983a)

Burns G. and Dacol F. H., *Phys. Rev. B.*, **28**, 2527 (1983b)

Burns G. and Dacol F. H., *Phys. Rev. B.*, **30**, 4012 (1984)

Burns G., *Phase transitions*, **5**, 261 (1985)

Burns G. and Dacol F. H., *Solid State Commun.*, **58**, 567 (1986)

Burns G. and Dacol F. H., *Ferroelectrics*, 104, 25 (1990a)

Burns G., Dacol F. H., Neurgaonkar R. R., Bhalla A. S. and Guo R., *Ferroelectrics,* **108,** 189 (1990b)

Burns G., Dacol F. H., Neurgaonkar R. R., Bhalla A. S. and Guo R., *Appl. Phys. Lett.* **57**(6), 543 (1990c)

Chattopanhuay S., Ayyub P., Palkar V. R., and Multani M., *Phys. Rev. B* **52**, 13177 (1995).

Cheng Z. Y., Cheng, L. Y., and Yao X., *J. Appl. Phys*. **79**, 8615(1996)

Choi S. W., Shrout T. R., Jang S. J., Bhalla A. S., *Ferroelecrics*, **100**, 29 (1989)

Cohen R. E. and Krakuer H., *Ferroelecrics* **111**, 57 (1990)

Cohen R.E., *J. Phys. Chem. Solids*, **61**, 139(1999)

Cross L. E., *Ferroelectrics* **76**, 241 (1987);

Cross L. E., *Ferroelectrics* **151**, 305 (1994).

DiDomenico Jr. M. and Wemple S. H., *Phys. Rev*.**166**, 565(1968)

DiDomenico Jr. M. and Wemple S. H., *J. Appl. Phys.* **40**, 720 (1969a)

DiDomenico Jr. M. and Wemple S. H., *J. Appl. Phys.* **40**, 735 (1969b)

Dierolf V., Sandmann C., Kim S., Gopalan V., and Polgar K., *Appl. Phys*. **93**, 2295 (2003)

Dow J. D., and Redfield D., *Phys. Rev*. **B. 5**, 594(1972)

El-Fadl A. Abu,. Gaffar M. A, Omar M. H., *Physica B* **269**, 403(1998)

Fu Desheng, Suzuki K., Kato K., and Suzuki H., *Appl. Phys. Lett*. **82**, 2130 (2003)

Fu H. X., Cohen R. E., *Nature* **403**, 281(2000)

Garcia A. and Vanderbilt D., *Appl. Phy. Lett*. **72**, 1981(1998)

Gerhring, P. M., Wakimoto S., Ye Z. G., and Shirane G., *Phys. Rev. Lett*. **87**, 277601 (2001)

Ghosez Ph. and Rabe K. M., *Appl. Phys. Lett*. **76**, 2767 (2000).

Ghosh G., *Opt. Lett.* **19**, 1391 (1994)

Ghosh G., *J. Appl. Phys*. **78**, 6752(1995)

Glass A. M., *J. Appl. Phys*. **40**, 4699 (1969).

Glinchuk M. D., Eliseev E. A., Stephanovich V. A., Hilczer B., *Phys. of the Solid State*, **43**, 1247 (2001)

Gopalan V., Mitchell T., Furukawa Y., and Kitamura K., *Appl. Phys. Lett*. **72**, 1981 (1998).

Gruverman A., Auciello O., and Tokumoto H., *Annu. Rev. Mater. Sci*. **28**, 101 (1998).

Guo R., Bhalla A. S., Randall C. A., Chang Z. P., and Cross L. E., *Ferroelectrics,* **93,** 989 (1989)

Guo R., Bhalla A. S., and Cross L. E., *Appl. Optics,* **29,** 904 (1990)

Guo R., Bhalla A. S., Randall C. A., and Cross L. E., *J. Appl. Phys.*, **67(10),** 6405 (1990)

Guo R., Bhalla A. S., Randall C. A., Chang Z. P., and Cross L. E., *J. Appl. Phys*. **67**, 1453 (1990)

Guo R., , Evans Jr. H.T., Bhalla A.S., *ISAF '96. Proceedings of the TenthIEEE International Symposium on Applications of Ferroelectrics,* **1,** 241 (1996)

Haefke H., Luithi R., Mayer K. P., and Guntherodt H. J., *Ferroelectric*, 151, 143 (1994)

Hasiang H. I. and Yen S. F., *J. Am. Ceram. Soc.* **79**, 1053 (1996)

Herrington J. R., Discher B., Rauber A., and Schneider J., *Solid state Commun*. **12**, 351(1973)

Hidaka T., Maruyama T., Saitoh M., Mikoshiba N., Shimizu M., Shiosaki T., Wills L. A., Hiskes R., Dicarolis S. A., and Amano Jun, *Appl. Phys. Lett.* **68**, 2358 (1996)

Hilczer B., Szezesniak L., Mayer K. P., *Ferroelectric*, 97,59 (1989)

Houde D., Lepine Y., Pepin C., Jandl S., and brebner J. L., *Phys. Rev*. **B 35**, 4948(1987)

Hunsche S., Grone A., Greten G., Kapphan S., Pankrth R., and Seglins J., *Phys. Status Solidi* **A 148**,629 (1995)

Isupov V. A., *Ferroelectrics* **90**, 113 (1989)

Isupov V. A., *Phys. Satatus Solidi* B213, 211 (1999)

Isupov V. A., *Phys*. *Solid State* **45**, 1107 (2003)

Ivanov N. R. Volk T. R., Ivleva L. I., Chumakova S. P., and Ginzberg A. V., *Crystallography Reports*, **47**(6), 1023 (2002)

Iwata M., Araki T., Maeda M., Suzuki I., Ohwa H., Yasuda N., Orihara H., and Ishibashi Y., *Jpn. J. Appl. Phys., Part 1* **41**, 7003 (2002)

Izawa Y., and Nakai S., *Applied optics*, **33**,6368 (1994)

Jaffe B., Cook Jr. W. R., and Jaffe H., "Piezoelectric Ceramics", Academic Press, London, (1971)

Kapphan S., and Weber G., f*erroelectrics* **37**, 637 (1981)

Kinase W., Ohnishi N., Yoshikawa M., and Mori K., *Ferroelectrics*, **56**, 165 (1984)

King-Smith R. D. and Vanderbilt D., *Phys. Rev*. **B 49**, 5828(1994)

Kirilov V. V. and Isupov V. A. *Ferroelectrics* **5**, 3 (1973)

Kleemann W. *J. Non-Crystalline Solids*, **307-310**, 66 (2002)

Kliger D. S., Lewis J. W., and Randall C. E., "Polarized light in optica and spectroscopy", Academic Press, Inc., (1990).

Koray E.Akdogan and Safari Ahmad, *Jpn. J. Appl. Phys., Part 1* **41**, 7170 (2002)

Kuwata J., Uchino K., and, Nomura S., *Ferroelectrics*, **22**, 863 (1979)

Kuwata J., Uchino K., Nomura S., *Jpn. J. Appl. Phys*. **21**, 1298(1982)

La-Orauttapong D., Toulouse J., Robentson J. L., Ye Z.-G., *Phys. Rev*. **B** 64, 212101(2001)

La-Orauttapong D., Noheda B., Ye Z.-G., Gehring P. M., Toulouse J., Cox D.E., and Shirane G., *Phys. Rev*. **B**. 65, 144101(2002)

Laulicht L. and Benguigui L., *Solid state Commun*. **32**, 771(1979)

Lee M., Feigelson R. S., Liu A., Hesselink L., Route R. K., *Phys. Rev*. **B, 56**, 7898(1997)

Lim L.C., Rajan K.K, *J.Crystal Growth* **271**, 435(2004)

Lines, M. E., Glass A.M., "Principles and Applications of Ferroelectrics and Related Materials", Oxford University Press, (1977)

Liu A.Y., Bashaw M.C., and Hesselink L., Lee M., Feigelson R.S., *Opt. Lett*. **22**,187(1997)

Lu Y., Cheng Z.-Y., Park S.-E., Liu S.-F., and Zhang Q., *Jpn. J. Appl. Phys*. **39,** 141 (2000).

Lu Y., Cheng Z.-Y., Barad Y., and Zhang Q. M., *J. Appl.Phys*. **89,** 5075 (2001).

Lu C. J., Ren S. B., Shen H. M., Liu J. S., and Wang N. Y., *J. Phys.: Condens. Matter* **8**, 8011 (1996).

Martirena H. T. and Burfoot J. C., *Ferroelectric* **7**, 151 (1974)

Mathan N. de, Husson E., Calvarin G., Gavarri J. R., Hewat A. W., and Morell A., *J. Phys.: Condens. Matter* **3**, 8159 (1991).

McHenry D. A., Giniewicz J., Jang S. J., Bhalla A. S., Shrout T. R., *Ferroelectrics*, **93**, 1137 (1989)

McHenry D. A., Ph. D. Thesis, The Pennsylvania State University , May(1992)

Mulvihill M. L., Cross L. E. and Uchino K., *J. Am. Ceram. Soc*. **78**, 3345 (1995)

Narasimhamurty, T. S. "Photoelastic and Electro-optic properties of crystals", Plenum Press, New York, (1981)

Newnham R. E., "Structure - Property Relations", Springer Verlag, New York, (1975).

Nishida Y. and Yamanaka M., *Review of Sci. Instru*. **72**, 2387 (2001)

Noheda B., Cox D. E., Shirane G., Gonzalo J., Cross L. E., and S. Park, *Appl. Phys. Lett*. **74**, 2059(1999)

Noheda B., Cox D. E., Shirane G., Gonzalo J., Park S., Cross L. E., and Zhong Z., *Phys. Rev. Lett.* **86**, 3891(2001)

Nye J. F., "Physical Properties of Crystals" (Clarendon Press, Oxford, 1990)

Ohmi M., Akatsuka M., Ishikawa K., Naito K., Yonezawa Y., Nishida Y., Yamanka M.,

Paz de Araujo C. A., Cuchiaro J.D., McMillan L. D., Scott M. C., and Scott J. F., *Nature, 374*, 627 (1995)

Phillips J. C., *Phys. Rev. Lett.* **20**, 505 (1968).

Phillips J. C. and Van Vechten J. A., *Phys. Rev. Lett.* **22**, 705 (1969).

Pirc R. and Blinc R., *Phys. Rev. B* **60**, 13470 (1999).

Pirc R. and Blinc R., *Phys. Rev. B* **61**, 14 448 (2000).

Pirc R., Blinc R., and Bobnar V., *Phys. Rev. B* **63**, 054203 (2001)

Rabe K. M. and Cockayne E., *First-priciples calculations for ferroelectric, Fifth Williamsburg Workshop* AIP, 61 (1998)

Randall, C. A. Bhalla A. S., *Jap. J. Appl. Phys*. **29** 327(1990a)

Randall C. A., Bhalla A .S., Shout T. R., and Cross L. E., *J. Mater. Res.* **5**, 829(1990b)

Randall C. A., Guo R., Bhalla A. S., and Cross L. E., *J. Mat. Res.*, **6(8),** 1720 (1991)

Santos Ivair A., Garcia D., Eiras José A., and Arantes Vera L., *J. Appl. Phys*. **93**, 1701 (2003)

Schlag S. and Eicke H. F., *Solid State Commun*. **91**, 883 (1994).

Schlarb U. and Betzer K., *Physics Rev.* **B48**, 15614 (1993)

Scott J. F., Duiker H. M., Beale P. D., Pouligny B., Dimmler K., Parris M., Butler D., and Eaton S., *Physica B & C* **150**, 160 (1988).

Setter N. and Cross L. E. *J. Appl. Phys.* **51**(8), 4356 (1980)

Shrout T. R., Fielding, Jr. J., *Ultrasonics Symposium, 1990. Proceedings., IEEE* 1990 , 4-7 Dec. 2, 711(1990)

Shrout T. R., Halliyal A., *Am. Ceram. Soc. Bulletin*, **Vol. 66**, No.4, 704(1987)

Skettrup G. A. T., *Phys. Rev.* **B.** 18, 2622(1978)

Smolenskii and Isupov V. A., *Dokl. Akad. Nauk SSSR* **9**,653 (1954).

Smolenskii G. A., *J. Phys. Soc. Japan* **28**, Suppl. 26(1970)

Svitelskiy O., La-Orauttapong D., Toulouse J., Chen W., Ye Z.-G, *Phys. Rev*. **B**. 72, 172106(2005)

Tangantsev A. K., *Phys. Rev. Lett*, **72**,1100(1994)

Toulouse J., Jiang F., Svitelskiy O., Chen W., Ye Z.-G, *Phys. Rev*. **B**. 72, 184106(2005)

Tsay Y. F., Bendow B., and Mitra S. S., *Phys. Rev.* **B8**, 2688 (1973)

Tsay Y. F., Lipson H. G., and Ligor P. A., *J. Appl. Phys*. **48**,1953(1977)

Tuttle B., Headley T., Drewien C., Michael J., Voigt J., and Gavino T., *Ferroelectrics* **221**, 209 (1999).

Tybell T., Ahn C. H., and Triscone J.-M., *Appl. Phys. Lett*. **75**, 856 (1999)

Uchino K. and Nomura S., *Ferroelectr. Lett. Sect*. **44**, 55 (1982)

Uchino K., *cer. Bull*. **65**, No. 8, 647 (1986)

Uchino K, "Ferroelectric Devices", Marcel Dekker Inc., New York, (2000)

Varshni Y. P., *Physica* **34**, 149 (1967)

Vakhrushev S. B., and Shapior S. M., *Phys. Rev.* **B 66**, 214101 (2002)

Viehland D., Jang S. J., Cross L. E., and Wuttig M., *J. Appl. Phys*. **68**, 847 (1990a).

Viehland D., Jang S. J., Cross L. E., *J. Appl. Phys*. **68**, 2916 (1990b).

Viehland D., Li J. F., Jang S. J., Cross L. E., *Phys. Rev.* **B 43**, 8316 (1991)

Vugmeister B. E. and Rabitz H., *Phys. Rev.* **B 57**, 7581 (1998)

Wan X., Xu H., He T., Lin. D., and Luo H., *J. Appl. Phys*, **93**, 4766 (2003)

Wan X., Luo H., Wang J., Chan H., and Choy C. *Solid state Commun.,* **129,** 401 (2004)

Wemple S. H. and DiDomenico Jr. M., *Phys. Rev. Lett.* **23**, 1156 (1969)

Wemple S. H. and DiDomenico Jr. M., *Phys. Rev.* **B 3**, 1338 (1971)

Wemple, S. H., "Laser handbook", eds Arecchi F. T. and Schulz-DuBois E. O. 975 (1972)

Wemple S. H., *Phys. Rev.* **B 7**, 3767 (1973)

Wemple S. H., *J. Chem, Phys*. **67**, 2151 (1977)

Weyrich K. H. and Madench R.P., *Ferroelecrics* **111**, 9 (1990)

Whatmore R. W., Osbond P. C., and Shorrocks N. M., *Ferroelectrics*, **76**, 351 (1987)

Wu Z., Cohen R. E., and Singh D. J, "Fundamental physics of ferroelectric" 2003 edited by David P.K. and Singh D. J., (2003)

Xiao Xiaoyue, Xu Yan, Zeng Zhigang, Gui Zhilun, Li Longtu, and Zhang Xiaowen, *J. Mater. Res*. **11**, 2302 (1996)

Xu Y., "Ferroelectric Materials and their Applications" North Holland, Amsterdam, (1991)

Yamashita Y., *Am. Ceram,Soc,Bull,***73**, 74(1994)

Yang T. J., Mohideen U., and Gopalan V., *Phys. Rev. Lett*. **82**, 4106 (1999)

Yang X., Lowell T. Wood, Miller, Jr. John H., and Strikovski M., *J. Appl. Phys*. **92**, 1168 (2002)

Yao X., Chen Z., and Cross L. E., *J. Appl. Phys*, **54**, 3399 (1984)

Zhang S. J. unpublished data

Zhong W., Jiang B., Zhang P., Ma J., Chen H., Yang Z., and Li L., *J. Phys.: Condens. Matter* **5**, 2619 (1993).

Zhong W. L., Wang Y. G., Zhang P. L., *Phys. Rev. B* **50**, 698 (1994).

Zhong W. L., Wang Y. X., Wang C. L., Jiang B., and Bursill L. A., *Ferroelectrics* **252**, 11 (2001).

Zhu S., Chen Y., and Fang J., *Phys. Rev.* **B. 35**, 2980(1987)

Zook J. D. and Casselman, T. N., *Phys. Rev. Lett.* **17**, 960 (1966)

Zysset B., Biaggio I., and Gu**¨**ter P., *J. Opt. Soc. Am. B* **9**, 380 (1992)

VITA

Chunlai Li was born on April 29, 1976 in Xiaogan city, Hubei, China. In high school he excelled in national math competition and was exempted from the entrance exam for college. He majored in physics in Wuhan University from 1992-1996. In 1999 He received his master degree in atomic and molecular physics from Wuhan Institute of Physics and Mathematics, the Chinese Academy of Sciences. He studied in the department of electrical engineering, the Pennsylvania Sate University since 2000 fall.